SYNTHESIS OF FIRST ROW TRANSITION METAL OXIDE NANOMATERIALS
FOR ELECTROCATALYTIC WATER OXIDATION REACTION

A THESIS SUBMITTED TO
THE GRADUATE SCHOOL OF NATURAL AND APPLIED SCIENCES
OF
MIDDLE EAST TECHNICAL UNIVERSITY

BY

ASUDE ÇETİN

IN PARTIAL FULFILLMENT OF THE REQUIREMENTS
FOR
THE DEGREE OF DOCTOR OF PHILOSOPHY
IN
CHEMISTRY

JANUARY 2020

Approval of the thesis:

SYNTHESIS OF FIRST ROW TRANSITION METAL OXIDE NANOMATERIALS FOR ELECTROCATALYTIC WATER OXIDATION REACTION

submitted by **ASUDE ÇETİN** in partial fulfillment of the requirements for the degree of **Doctor of Philosophy** in **Chemistry, Middle East Technical University** by,

Prof. Dr. Halil Kalıpçılar
Dean, Graduate School of **Natural and Applied Sciences**   _____

Prof. Dr. Cihangir Tanyeli
Head of the Department, **Chemistry**   _____

Assoc. Prof. Dr. Emren Nalbant Esentürk
Supervisor, **Chemistry, METU**   _____

Examining Committee Members:

Prof. Dr. Saim Özkar
Chemistry, METU   _____

Assoc. Prof. Dr. Emren Nalbant Esentürk
Chemistry, METU   _____

Prof. Dr. Ahmet M. Önal
Chemistry, METU   _____

Prof. Dr. Birgül Zümreoğlu Karan
Chemistry, Hacettepe University   _____

Assist. Prof. Dr. Ferdi Karadaş
Chemistry, Bilkent University   _____

Date: 15.01.2020

I hereby declare that all information in this document has been obtained and presented in accordance with academic rules and ethical conduct. I also declare that, as required by these rules and conduct, I have fully cited and referenced all material and results that are not original to this work.

Name, Last name : Asude Çetin

Signature :

ABSTRACT

SYNTHESIS OF FIRST ROW TRANSITION METAL OXIDE NANOMATERIALS FOR ELECTROCATALYTIC WATER OXIDATION REACTION

Çetin, Asude
Doctor of Philosophy, Chemistry
Supervisor : Assoc. Prof. Dr. Emren Nalbant Esentürk

January 2020, 141 pages

Environmental concerns associated with the use of fossil fuels have elevated the demand for safe, clean and renewable energy sources. Hydrogen is an outstanding energy carrier because of the high amount of energy stored in its bond, and an excellent alternative to fossil fuels. Therefore, production of hydrogen from readily available and abundant sources such as water through electrochemical water splitting has gained increasing attention in the last couple of decades. However, water oxidation step of overall water splitting process has large energy barrier and thus, requires application of overpotential and use of highly stable and active catalysts for the efficient formation of hydrogen. A great number of nano-sized metal oxide materials have been proven to be very active catalysts for electrochemical water oxidation. In addition to their unique properties, their large surface area and thus, large active sites make such nanomaterials promising candidates as electrocatalysts. This dissertation covers the preparation and characterization of bimetallic oxide nanomaterials composed of various combinations of earth abundant, transition metals as well as their electrochemical activities towards water oxidation reaction.

Firstly, metal oxide nanomaterials in $CuCr_2O_4$, $FeMnO_3$, $NiFe_2O_4$-NiO and $NiCo_2O_4$-NiO structures with various morphologies were synthesized via simple and reproducible methods. Synthesized nanomaterials were then characterized using a combination of analytical techniques including XRD, SEM, EDX, TEM, XPS, ICP-OES and BET. Conductive electrode surfaces were modified with these nanomaterials, and finally their electrochemical behavior in water oxidation reaction were investigated. The overall water oxidation activity of the synthesized materials was observed to be comparable to benchmark RuO_2 or superior to some of the water oxidation catalysts having similar structures.

Keywords: Transition Metal Oxide, Nanomaterials, Water Oxidation, Oxygen Evolution, Electrocatalysis

ÖZ

İLK SIRA GEÇİŞ METAL OKSİT NANOMALZEMELERİN SENTEZİ VE SUYUN ELEKTROKATALİTİK YÜKSELTGENME TEPKİMESİNDE KULLANIMI

Çetin, Asude
Doktora, Kimya
Tez Yöneticisi: Doç. Dr. Emren Nalbant Esentürk

Ocak 2020, 141 sayfa

Fosil yakıtların kullanımından kaynaklanan çevresel endişelerin artması güvenli, temiz ve yenilenebilir enerji kaynaklarına olan talebi önemli ölçüde artırmıştır. Hidrojen, bağında bulundurduğu yüksek enerji sebebiyle önde gelen enerji taşıyıcılarındandır. Aynı zamanda bu özelliğiyle fosil yakıtların kullanımına önemli bir alternatiftir. Bu sebeple, su gibi kolayca erişilebilen ve doğada bol miktarda bulunan kaynaklardan elektrokimyasal ayrıştırma yöntemiyle hidrojen elde edilmesi son yirmi yılda artan ilgi odağı haline gelmiştir. Fakat, suyun yükseltgenmesinin gerçekleştiği anot yarı tepkimesi yüksek enerji bariyeri sebebiyle suyun ayrışmasını yavaşlatmaktadır. Bu da, hidrojenin verimli bir şekilde elde edilebilmesi için aşırıgerilim uygulanmasını ve yüksek kararlılık ve etkinliğe sahip katalizörlerin kullanımını gerekli kılmaktadır. Çok sayıda metal oksit nanomalzeme suyun elektrokimyasal yükseltgenmesinde kullanılmış ve etkinlikleri kanıtlanmıştır. Benzersiz özelliklerinin yanı sıra, sahip oldukları geniş yüzey alanı ve dolayısıyla çok sayıdaki aktif yüzeyleriyle bu nanomalzemeler elektrokatalizör olarak gelecek vaat etmektedirler. Bu tez, doğada bol bulunan geçiş metalleri kullanılarak çeşitli

bileşimlerde bimetalik nanomalzemelerin hazırlanması ve tanımlanmasının yanı sıra suyun yükseltgenme tepkimesindeki elektrokimyasal etkinliklerinin incelenmesini kapsamaktadır. İlk olarak, farklı şekillere sahip $CuCr_2O_4$, $FeMnO_3$, $NiFe_2O_4$-NiO and $NiCo_2O_4$-NiO yapılarında nanomalzemeler kolay ve tekrarlanabilir yöntemlerle sentezlenmiştir. Sentezlenen nanomalzemeler XRD, SEM, EDX, TEM, XPS, ICP-OES ve BET gibi çeşitli analitik tekniklerle tanımlanmıştır. Daha sonra, iletken elektrot yüzeyleri bu nanomalzemelerle kaplanmış ve son olarak suyun yükseltgenme tepkimesinde elektrokimyasal etkinlikleri incelenmiştir. Sentezlenen malzemeler, bu tepkimede referans olarak kullanılan RuO_2 katalizörle kıyaslanabilir etkinlik göstermiştir. Bu malzemelerin benzer yapılardaki diğer katalizörlere kıyasla suyun yükseltgenmesinde daha aktif oldukları görülmüştür.

Anahtar Kelimeler: Geçiş Metal Oksitler, Nanomalzemeler, Suyun Yükseltgenmesi, Oksijen Salınımı, Elektrokataliz

To my beloved family,

ACKNOWLEDGMENTS

to thank Cansu Börüban Bingöl, İlkem Evcimen and Esra Öğün. Those years we were together in the laboratory were truly precious and I enjoyed every single moment of them.

I am greatly thankful to my dear friends Duygu Tan and Derya Özhava, who are like sisters to me, for their unselfish moral support, friendship and for always being there for me whenever I needed.

Last but not least, my most heartfelt appreciation goes to my parents, Aydın Çetin and Rukiye Çetin. I am deeply grateful for their love, caring and constant support in the pursuit of my dreams and more importantly, for always believing in me.

TABLE OF CONTENTS

LIST OF TABLES

LIST OF FIGURES

FIGURES

xviii

LIST OF ABBREVIATIONS

ABBREVIATIONS

TMO   Transition Metal Oxide

ccp   cubic close packing

hcp   hexagonal close packing

CFSE   Crystal Field Stabilization Energy

OSPE   Octahedral Site Preference Energy

XRD   X - Ray Diffraction

FWHM   Full width half maximum

SEM   Scanning Electron Microscopy

EDX   Energy Dispersive X-Ray

TEM   Transmission Electron Microscopy

HAADF   High - Angle Annular Dark Field

STEM   Scanning Tunnelling Electron Microscopy

XPS   X - Ray Photoelectron Spectroscopy

ICP-OES   Inductively Coupled Plasma - Optical Emission Spectroscopy

BET   Brunauer – Emmett – Teller

STM   Scanning Transmission Electron Microscopy

IR   Infrared Spectroscopy

LSV   Linear Sweep Voltammetry

CV   Cyclic Voltammetry

EIS	Electrochemical Impedance Spectroscopy
FTO	Fluorinated Tin Oxide
GC	Glassy Carbon
CPE	Constant Phase Element
RHE	Reversible Hydrogen Electrode
RDE	Rotating Disk Electrode
ECSA	Electrochemically Active Surface Area
RF	Roughness Factor
NTA	Nitrilotriacetic acid
CTAC	Cetyltrimethylammonium chloride
CTAB	Cetyltrimethylammonium bromide
EG	Ethylene glycol
TEG	Triethylene glycol
DMF	Dimethylformamide
PEO	Polyethylene oxide
U-NiCo	Urea-stabilized $NiCo_2O_4/NiO$
C-NiCo	CTAC-stabilized $NiCo_2O_4/NiO$
MWCNT	Multiwalled Carbon Nanotube
PL6	Printex L6
SC65	Super C6

CHAPTER 1

INTRODUCTION

The depletion of fossil fuels and environmental concerns associated with their extensive use have increased the demand for renewable, cheap, clean and safe energy sources significantly. Hydrogen, as an energy carrier is an outstanding alternative to fossil fuels or other risky sources such as nuclear energy. Moreover, hydrogen can be easily obtained from readily available and renewable sources such as water. Therefore, production of hydrogen, which is defined as the "sustainable fuel" of the future, through water splitting has gained well deserved attention and become focus of intensive research in the last couple of decades.

Production of hydrogen through electrochemical water splitting is particularly very attractive. However, water oxidation step occurring at the anode is considered as the bottleneck of overall water splitting. This is mostly because of the large energy barrier caused by the transfer of multiple electrons and protons during the reaction and thus, requires application of overpotential to overcome this energy barrier. Therefore, reducing the applied overpotential and increasing the rate of this reaction is critical in efficient production of hydrogen. Use of suitable catalysts is considered to be very effective in achieving this goal. Hence, designing new catalyst systems which can demonstrate high stability for multiple oxidation cycles and operate at low overpotential has become of utmost importance. Among the potential water oxidation electrocatalysts, metal oxides are one of the prominent choices in this demanding process. Particularly, nano-sized metal oxide particles, rods, wires or plates has drawn attention because of their high surface-to-volume ratio and thus, large surface area.[1–3]

The most active and widely used metal oxide electrocatalysts are the oxides of precious and rare metals (i.e. RuO_2 and IrO_2). For instance, Liu et al. reported that

1

RuO$_2$ nanoparticles exhibited very good activity with an onset potential of 1.34 V (vs RHE) and a low overpotential of 190 mV to achieve current density of 10 mA cm^{-2} (η_{10}).[4] In addition, studies conducted by Sun et al. and Gao et al. exhibited very similar activities for RuO$_2$ nanomaterials. Both reports have shown that the onset potential was 1.48 V (vs RHE) for RuO$_2$ while slight differences in η_{10} was noted (325 mV[5] and 347 mV[2]). Similar to their results, in our study too we have found that RuO$_2$ nanoparticles display good activity and determined the onset potential and η_{10} as 1.45 V (vs RHE) and 326 mV, respectively. Even though, RuO$_2$ and IrO$_2$ demonstrate high activity, their high cost, low availability and poor stability under alkaline conditions limit their practical use.[6–10] Therefore, it is of great importance to prepare metal oxide nanocatalysts with high stability and efficiency using earth abundant and cheap transition metals.

Bimetallic materials in the form of perovskite or spinel have particularly attracted great deal of attention because of their rich chemistry caused by the contributions of both metals, very good stability and activity in alkaline medium.[8,11–14]

Inspired by the Mn$_4$CaO$_5$ clusters in photosystem II, many catalyst systems composing of manganese have been developed. To illustrate, Kim et al. reported the synthesis and electrocatalytic activity of CaMnO$_3$ in perovskite structure for water oxidation in alkaline medium. Rotating disk electrodes (RDEs) modified with nanomaterial exhibited an onset potential of 1.6 V (vs RHE) and Tafel slope of 197 mV dec^{-1}. In addition, they have prepared oxygen-deficient Ca$_2$Mn$_2$O$_5$ perovskite material and studied its activity under the same conditions for comparison. The results reveal that with increased oxygen deficiency both onset potential (1.5 V vs RHE) and Tafel slope (149 mV dec^{-1}) decreased indicating improved water oxidation activity.[15] Peng et al. demonstrated that upon doping with sulfur, CaMnO$_3$ nanotubes display better activity as electrocatalyst for water oxidation with higher stability. The onset potential was found as 1.6 V (vs RHE) while it was ca. 1.7 V (vs RHE) for pristine CaMnO$_3$. The observed enhanced activity was associated with the abundant active sites induced by oxygen vacancies due to sulfur replacement.[16] Another study conducted by Du et al. exhibited the preparation of a series of nonstoichiometric

$CaMnO_{3-\delta}$ nanomaterials $(0 < \delta < 0.5)$ and their water oxidation activities. The results show that $CaMnO_{2.77}$ nanoparticles demonstrated the highest activity among the prepared nanomaterials with an onset potential of 1.4 V (vs RHE) and overpotential of 570 mV to generate current density of 4 mA cm^{-2} (η_4).[17]

Perovskite structures having different metal combinations were also reported as water oxidation electrocatalysts. For instance, Jin et al. studied urchin-like $La_{0.8}Sr_{0.2}MnO_3$ materials and reported that the materials exhibit promising activities with onset potential and η_{10} of 1.57 V (vs RHE) and 985 mV.[18] Studies conducted by Hua et al., on the other hand, showed that $La_{0.8}Sr_{0.2}Mn_{0.9}Fe_{0.1}O_{3-\delta}$ materials have lower η_{10} value (340 mV) compared to the one of reported by Jin et al.[19] Moreover, various studies have reported that doping or coating the metal oxide nanomaterial with a non-metal can enhance its water oxidation activity. To illustrate, Xu et al. compared the electrocatalytic activities of both pristine and carbon-coated $BaMnO_3$ nanorods. The results showed that at the same overpotential value (i.e. 740 mV) observed current density increased significantly from 3 mA cm^{-2} to 14 mA cm^{-2} suggesting the improved conductivity upon coating with carbon.[20]

Another widely used bimetallic oxide materials are the ones having spinel structures. In several studies, it was observed that bimetallic spinel oxides exhibit higher water oxidation activities compared to their monometallic counterparts. For instance, Yuan et al. have synthesized a series of tubular ferrite materials (MFe_2O_4, M: Fe, Co, Ni) and studied their activities by comparing overpotential values required to generate a current density of 10 mA cm^{-2} (η_{10}). Fe_3O_4 nanotubes exhibited the lowest activity with η_{10} value of 432 mV, whereas $NiFe_2O_4$ and $CoFe_2O_4$ nanotubes required overpotentials of 340 and 392 mV to achieve the same current density value, respectively.[21] Li et al. also studied a series of iron based catalysts for water oxidation. They prepared Fe_2O_3 and MFe_2O_4 (M: Mn, Co, Ni, Cu) nanoparticles by electrospinning and investigated their activities.[22] Similar to the work of Yuan et al, in this study too, monometallic Fe_2O_3 nanoparticles exhibited the lowest activity with an onset potential of 1.79 V (vs RHE) and η_5 of 750 mV, while much lower onset potentials and overpotential were obtained for $MnFe_2O_4$ (1.72 V vs RHE, η_5: 640

mV), $CoFe_2O_4$ (1.67 V vs RHE, η_5: 520 mV), $CuFe_2O_4$ (1.71 V vs RHE, η_5: 540 mV) and $NiFe_2O_4$ (1.70 V vs RHE, η_5: 550 mV). In addition, nanofibers of the same structures were also prepared and activities were tested for water oxidation for comparison. Each of the fibers displayed higher catalytic activities with lower onset potentials and overpotentials than their nanoparticle counterparts. Observed activity was attributed to the larger surface area of the nanofibers which allows more contact sites between the catalyst and the substrate.[22]

Among transition-metal based spinel oxides, $NiCo_2O_4$ is also subjected to considerable attention owing to its rich redox chemistry caused by the contributions of both cobalt and nickel ions. In addition, recent studies have shown that $NiCo_2O_4$ exhibits higher electrical conductivity and thus, enhances electrochemical activity than its monometallic counterparts (NiO and Co_3O_4).[23] Barauskiene and Valatka have reported the preparation of $NiCo_2O_4$ nanomaterials on stainless steel by electrodeposition and investigated its activity towards water oxidation reaction. They concluded that the prepared nanomaterial has comparable activity to that of benchmark IrO_2 with an onset potential of 1.6 V (vs RHE) and η_{10} of 530 mV.[24] On the other hand, Zhao et al. reported a slightly higher onset potential of 1.63 V (vs RHE) with lower η_{10} (440 mV) for $NiCo_2O_4$ nanomaterials.[25] $NiCo_2O_4$ nanomaterials were also prepared in wire morphology and tested for electrocatalytic water oxidation. According to the studies by Peng et al. $NiCo_2O_4$ nanowires exhibited good activity with low onset potential of 1.56 V (vs RHE).[26] Nanowires prepared by Yu et al. also demonstrated low overpotential value of η_{10}: 460 mV.[27] On the other hand, Su et al. reported $NiCo_2O_4$ nanowire arrays having superior water oxidation activity. The overpotential required to achieve current density of 10 mA cm^{-2} was determined as 350 mV with use of much smaller catalyst loading (0.2 mg cm^{-2}) compared to the one reported by Yu et al. (1.0 mg cm^{-2}).[28]

Furthermore, recent studies have revealed that co-presence of NiO and $NiCo_2O_4$ or $NiFe_2O_4$ boosts each other's activity significantly because their close interaction promotes better charge transfer. There are several literature reports on the synthesis and electrocatalytic activities for water oxidation reaction of such heterostructures.

4

Mahala and Basu prepared both $NiCo_2O_4$ and $NiO/NiCo_2O_4$ nanosheets and compared their electrocatalytic activities. Biphasic $NiO/NiCo_2O_4$ nanosheets exhibited higher catalytic performance with much lower onset potential (1.59 V vs RHE), overpotential (η_{10}: 360 mV) and Tafel slope (61 mV dec^{-1}) than that of $NiCo_2O_4$ (Onset: 1.66 V vs RHE, η_{10}: 430 mV, Tafel slope: 139 mV dec^{-1}).[29] Liu et al. also performed a similar study by using $NiFe_2O_4$ and $NiO/NiFe_2O_4$ nanorods. The onset potential and η_{10} for $NiFe_2O_4$ nanorods were found as 1.55 V (vs RHE) and 370 mV, respectively. On the other hand, $NiO/NiFe_2O_4$ heterostructure demonstrated enhanced performance with an onset potential of 1.46 V (vs RHE) and η_{10} of 302 mV.[30,31]

In the light of these information, this dissertation aims to synthesize bimetallic oxide catalyst systems composing of earth abundant, first row transition metals in the nano regime and study their electrochemical activities towards water oxidation reaction. Preparation of the nanomaterials were achieved by two facile solution-phase methods, namely sol-gel and hydrothermal synthesis. Obtained nanomaterials were then characterized by several analytical techniques. After characterization, electrode surfaces such as fluorinated tin oxide (FTO) and glassy carbon (GC) were modified with synthesized nanomaterials and their performance in water oxidation reaction were investigated using electrochemical techniques. Prepared transition metal oxide nanomaterials were found to be stable catalysts in electrochemical water oxidation. Furthermore, activities of the catalysts were observed to be comparable to that of water oxidation catalysts with similar structures.

CHAPTER 2

TRANSITION METAL OXIDES

2.1   General Introduction

The binary compounds of oxygen with transition metals constitute one of the most intriguing groups of materials due to their facile synthesis, stability and diverse composition and structure. In addition, ability of transition metals to have multiple oxidation states leads to a great number of compounds with tunable properties such as thermal, electrical, magnetic and optical properties for specific applications. Such diversity of transition metal oxides (TMOs) stems from the partially filled d-orbitals of the metal and the interactions between electrons in these orbitals.[32,33]

TMOs are formed by electron transfer between less electronegative transition metal atoms and more electronegative oxygen atoms. Depending on the number of electrons lost in their d-orbitals, transition metals can form a wide range of oxides from monoxides (e.g NiO), dioxides (e.g RuO_2), to higher and complex oxides (e.g WO_3, $LaMnO_3$, $NiCo_2O_4$). Each of these oxides embodies different bonding and crystal structures. Hence, it is necessary to apprehend the crystal chemistry of TMOs in order to better interpret their behavior in certain applications.

2.2   Classification and Crystal Structures of Transition Metal Oxides

TMOs crystallize in many structures namely, rock salt, wurtzite, rutile, ReO_3, perovskite, spinel and corundum-type. Common feature of these structures is that larger oxide ions are arranged in either cubic or hexagonal close-packed arrays, which leads to formation of octahedral and tetrahedral networks while the smaller transition metal ions occupy the holes created by these oxide networks.

7

2.2.1   Monoxides

All of the first row transition metals, except scandium and chromium, form *monoxides*. Five of the second row transition metals (zirconium, niobium, palladium, silver and cadmium) along with mercury of third row transition metals form monoxides as well. Most of them crystallize in *rock salt* structure in which oxide ions form cubic close packing (ccp) array and the transition metal ions occupy all of the octahedral holes (Figure 2.1). Alternatively, this structure can be described as being composed of corner-sharing octahedral MO_6 units with (6,6)-coordination.[32,33]
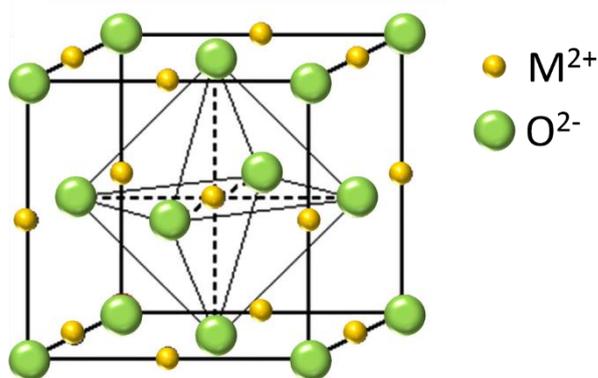
Figure 2.1. Unit cell of rock salt structure (green circles: oxygen atoms, yellow circles: transition metal atoms)

In some cases, nonstoichiometry, atom deficiency or relocation of atoms from their ideal positions can result in deviations in TMOs. Some of these monoxides, such as ZnO, adopt *wurtzite* structure. Wurtzite structure comprise of hexagonal close packing (hcp) arrays of oxide ions with transition metal ions located in half of the tetrahedral cavities (Figure 2.2). Each ion is surrounded by four counter ion leading to (4,4)-coordination.[32,33]
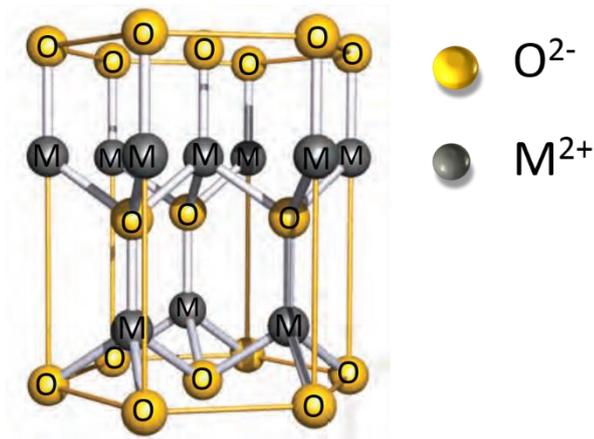
Figure 2.2. Unit cell of wurtzite structure (yellow circles: oxygen atoms, grey circles: transition metal atoms) (modified from [34])

2.2.2   Dioxides

Dioxides are formed by titanium, vanadium, chromium and manganese of first row transition metals. In addition, almost all of the second and third row transition metals, except cadmium form dioxides. These TMOs assume either *rutile* or *fluorite* crystal structures. The rutile structure is made up of hcp arrays of oxide ions (Figure 2.3). Ideally, in this structure, half of the octahedral holes are occupied by the transition metal ions while the tetrahedral holes are empty. Each transition metal ion is surrounded by six oxygen and each oxygen is surrounded by three metal ion, resulting in (6,3)-coordination.[32,33]
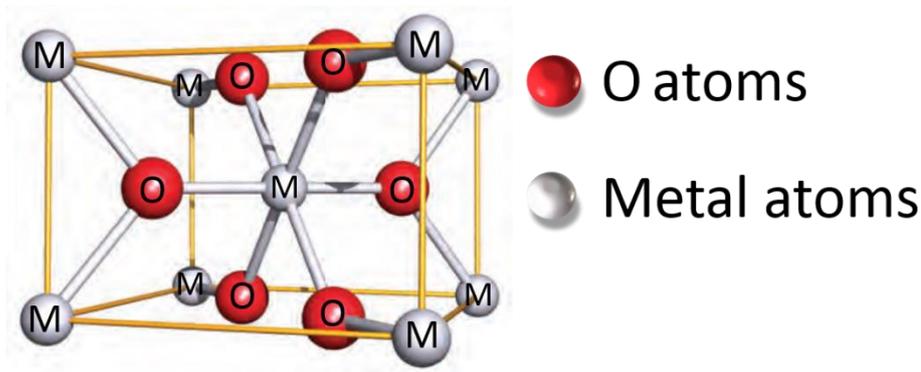
Figure 2.3. Unit cell of rutile structure (red circles: oxygen atoms, pale grey circles: transition metal atoms) (modified from[34])

Figure 2.4 shows the fluorite structure. As opposed to other structures, transition metal ions arrange in ccp arrays while oxide ions occupy all of the tetrahedral holes forming a lattice with (8,4)-coordination.
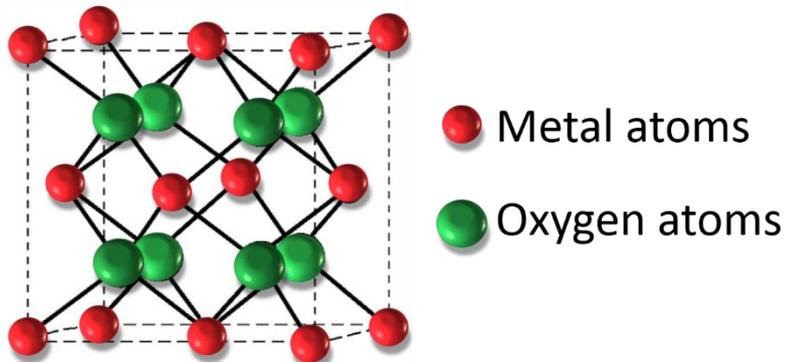
Figure 2.4. Unit cell of fluorite structure (green circles: oxygen atoms, red circles: transition metal atoms)

2.2.3   Sesquioxides – corundum type

Most of the first row transition metals in their +3 oxidation state, except zinc, crystallize in *corundum-type structure* (M_2O_3). In this structure, the transition metal ions (M^{3+}) are located in two-third of the octahedral cavities which are formed by hcp arrangement of oxide ions (Figure 2.5) giving rise to a (6,4)-coordination.[32]
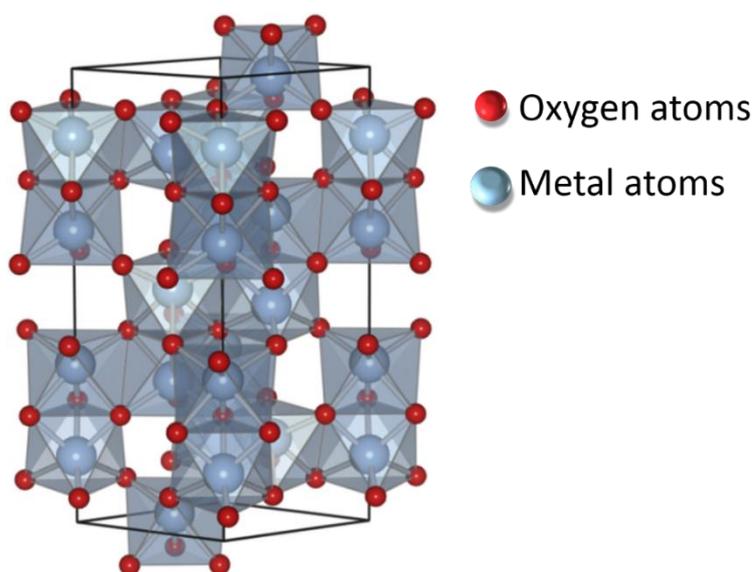
Figure 2.5. Corundum structure of TMOs (M_2O_3) (red circles: oxygen atoms, blue circle: transition metal atoms occupying the octahedral cavity formed by O^{2-} ions) (modified from[32])

2.2.4   Trioxides

Transition metals forming *trioxides* are rare due to the requirement of +6 oxidation state. Molybdenum, rhenium and tungsten are the only transition metals that show MO_3 stoichiometry. These oxides adopt rhenium trioxide structure which consist of cubic unit cell with Re ions at the corners and oxide ions at the edge-centers (Figure 2.6). Alternatively, the structure can be viewed as being made up of corner-sharing

ReO_6 octahedra. Molybdenum trioxide (MoO_3) has a layer structure which is composed of chains formed by corner sharing MoO_6 octahedral units. These two chains are attached to each other by sharing adjacent edges of the octahedra resulting in a double layer. In WO_3, slightly distorted WO_6 units are connected by corner sharing.[32]
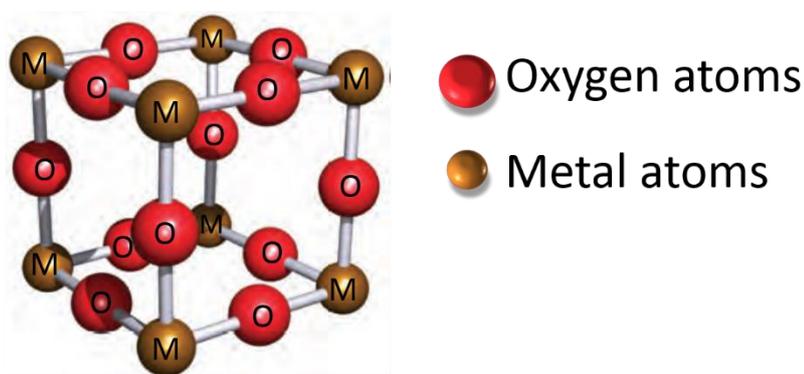
Figure 2.6. Unit cell of ReO_3 structure (red circles: oxygen atoms, gold circles: transition metal atoms) (modified from[34])

2.2.5 Spinels

TMO *spinels* generally have the AB_2O_4 composition, where A and B are metal ions. The spinel structure is formed by ccp array of oxide ions in which A cations fill one-eighth of the tetrahedral voids and the B cations fill half of the octahedral voids (Figure 2.7). In order to maintain charge neutrality, cation A and B can have oxidation states of either +2 and +3 ($A^{2+}B_2^{3+}O_4^{2-}$) or +4 and +2 ($A^{4+}B_2^{2+}O_4^{2-}$), respectively[8].
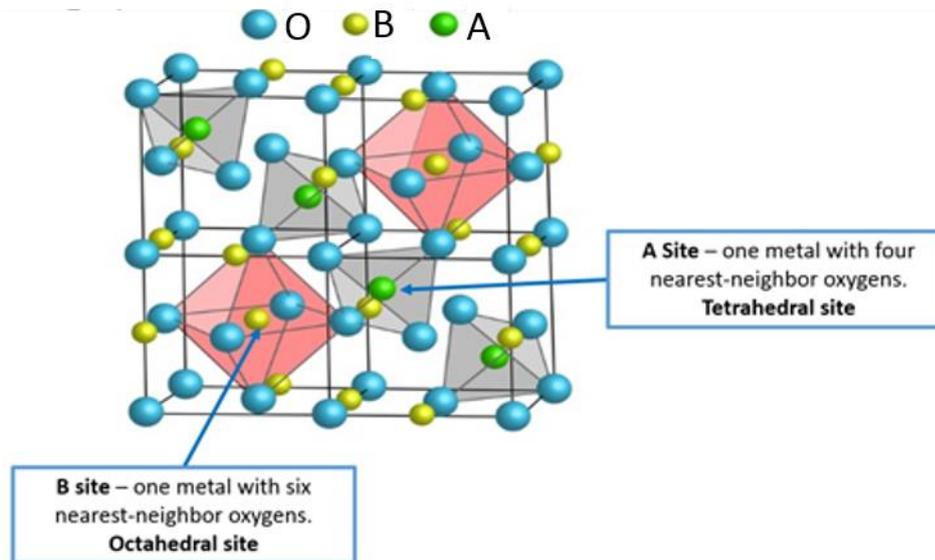
Figure 2.7. Unit cell of spinel structure (green circles: A cations, yellow circles: B cations and blue circles: oxygen atoms)

Depending on the cation distribution in tetrahedral and octahedral holes, spinels can be categorized into three types, namely normal, inverse and complex spinels. Zhao et al suggested the following representation of spinels, $A_{1-\lambda}B_\lambda[A_\lambda B_{2-\lambda}]O_4$, in order to identify them easily. In this notation, $[A_\lambda B_{2-\lambda}]$ represent the metal ions occupying octahedral holes while the ions before square brackets, $A_{1-\lambda}B_\lambda$, represent the ones located in tetrahedral holes. When $\lambda = 0$, the structure is defined as *normal spinel* $(A[B_2]O_4)$ with A^{2+} and B^{3+} ions located in tetrahedral and octahedral holes, respectively. $\lambda = 1$ leads to *inverse spinel* structure which can be denoted as $B[AB]O_4$. In inverse spinel, A^{2+} ions occupy the octahedral sites while B^{3+} ions are equally distributed in octahedral and tetrahedral sites. In the case of $0 < \lambda < 1$, the structure is complex spinel. Complex spinels have mixed metal ion distribution in octahedral and tetrahedral sites. In this regard, they are considered as being intermediate between normal and inverse spinels.[8]

Distribution of metal ions in spinel structures is governed by several factors namely, radius of the metal, electrostatic interactions between ions and the crystal field

stabilization energy (CFSE) difference between octahedral and tetrahedral fields of the metal ions. This energy difference, also named as octahedral site preference energy (OSPE), has a significant effect on the structure adopted by the TMOs. For instance, Mn_3O_4 has a normal spinel structure since Mn^{3+} ion can acquire higher CFSE occupying octahedral interstices. Hence, Mn^{2+} ions occupy tetrahedral interstices giving rise to $Mn^{2+}[Mn_2^{3+}]O_4$ configuration. On the other hand, Fe^{2+} ions rather than Fe^{3+} ions in Fe_3O_4 strongly prefer to fill octahedral holes because of their greater CFSE in octahedral field. Thus, Fe_3O_4 is inverse spinel with $Fe^{3+}[Fe^{2+}Fe^{3+}]O_4$ configuration.[8,32,33]

2.2.6 Perovskite

Perovskite structure, generally denoted as ABO_3, is based on ReO_3 structure. Corner sharing octahedral BO_6 units are arranged in cubic network, and A cations occupy the 12-coordinate hole created by these octahedra (Figure 2.8). The structure can also be described as A cation located in the center of a cube formed by the B cations, whereas oxide ions reside in the edge centers of the cube.
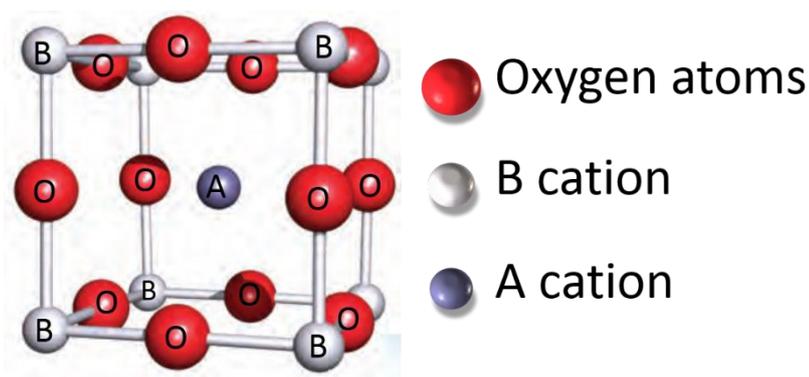
Figure 2.8. Unit cell of perovskite (ABO_3) structure (red circles: oxygen atoms, purple circle: A cation and pale grey circles: B cations) (modified from[34])

In perovskite structure, A and B cations can bear different charge distributions in order to achieve charge neutrality; $A^{1+}B^{5+}O_3$ (e.g. $NaWO_3$), $A^{2+}B^{4+}O_3$ (e.g. $CaTiO_3$) and $A^{3+}B^{3+}O_3$ (e.g. $LaCoO_3$). Generally, A ions are alkali, alkaline earth or lanthanide ions while B are transition metals ions.[32,33,35]

2.3   Preparation of Transition Metal Oxide Nanomaterials

Materials in the nano regime have attracted considerable attention owing to their unique properties and viability in numerous applications. The exciting properties of the nanomaterials, which can be altered to suit certain applications, have motivated researchers to explore new synthetic approaches to prepare such materials. Consequently, many different methods have been employed and made it possible to obtain nanomaterials with a wide range of unique morphologies, crystal structures and compositions.

Transition metal oxide nanomaterials can be prepared by two basic approaches, namely *top-down* (physical methods) and *bottom-up* (physical and chemical methods). Top-down method includes the miniaturization of the large scale material by lithography or other related techniques. However, high cost, irregular and rough features obtained on atomic scale and irreproducibility restrict the use of this method in the preparation of nanomaterials.[36] On the other hand, bottom-up approach consist of assembling atoms or molecules to generate large scale materials. Bottom-up approach also has the advantage of control over crystallite size and/or shape by use of atoms, molecules or individual nanoparticles as building blocks.[36] Moreover, this technique includes a wide variety of methods ranging from solid-phase synthesis (e.g. flux growth, thermal decomposition, pulsed laser ablation/deposition) to solution-phase (e.g. coprecipitation, polyol, microemulsion, sol-gel, hydrothermal/solvothermal) and vapor-phase synthesis (e.g. chemical vapor deposition, spray pyrolysis, magnetron sputtering).[8]
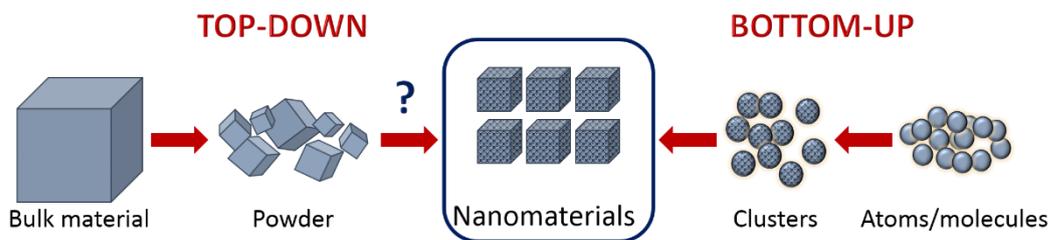
Figure 2.9. Top-down and bottom-up approaches used to obtain naomaterials

Among all these methods, solution-phase synthesis has several advantages over solid- or gas-phase methods. It provides control over the reaction pathways which enables synthesis of nanomaterials with distinct crystal structures. In addition, nanoparticles having uniform size distribution, homogeneous compositions and morphologies can be obtained by utilizing solution-phase synthesis.[36] The most common synthetic routes used in the solution-phase preparation of TMO nanomaterials are sol-gel and hydrothermal/solvothermal methods and the details of these techniques are explained in the following sections.

2.3.1 Sol-Gel Method

Sol-gel process is one of the most facile methods for the synthesis of metal oxide materials, most commonly as nanoparticles. It can be defined as inorganic polymerization of precursors to yield inorganic solids (Figure 2.10).[8,36,37] A typical sol-gel synthesis consists of the following steps:

i) *Formation of sol* by dissolution of the precursors together with a suitable reagent in a solvent. Mostly, metal salts or metal alkoxides are used as precursors. Citric acid, propionic acid and ethylene glycol are generally added as chelating agents. After dissolution, precursors are hydrolyzed to yield hydroxides/monomers followed by a condensation step to form oligomers.

16

ii)   *Formation of gel* by further condensation of the monomers/oligomers. In this step, due to hydrogen bonding between the solvent and the gel, the oxide material consists of porous structure.

iii)   *Aging:* In this step, condensation of the gel continues and it solidifies. In order to increase the rate of aging process, it can be done by heating the obtained gel.

iv)   *Drying:* Drying process can be done either by supercritical drying, which results in the formation of aerogel with high porosity in the structure or by thermal evaporation leading to xerogel formation with smaller pore size compared to that of aerogel.

v)   *Dehydration:* In this step, -OH groups present on the surface and organic moieties are removed by thermal treatment at elevated temperatures.

- Metal precursors
- Complexing agent (e.g. citric acid)
- Water
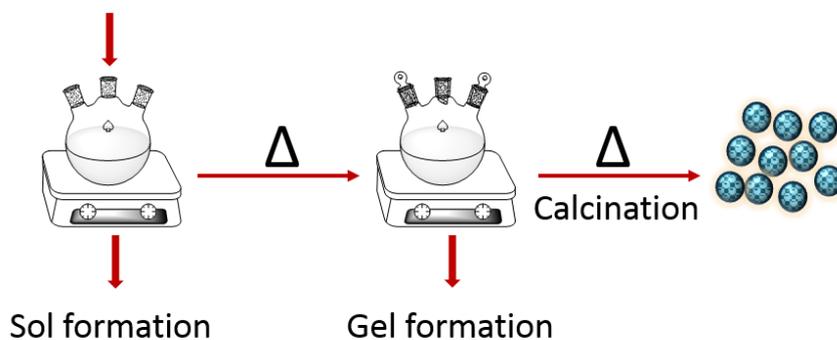
Figure 2.10. Schematic representation of sol-gel synthesis of nanomaterials

2.3.2 Hydrothermal / Solvothermal Method

Hydrothermal method is defined as high-pressure solution-phase synthesis in which the solvent is water. As an alternative to water, other solvents such as ethanol, 2-propanol or ethylene glycol can also be used, and this method is referred to as *solvothermal* synthesis.[8] In this method, autoclaves which can tolerate high temperature and pressure are used as reaction vessels.

This method is one of the most commonly used techniques for the synthesis of TMO nanomaterials having a wide variety of morphologies. The working principle is that upon heating the mixture in the autoclave, regions having two different temperatures are created. The precursors are dissolved in the hotter region which resides in the lower part of the vessel. Then, this solution ascends to the upper part while the cooler part of the solution settles down. As the temperature of the upper part is reduced, the solution becomes supersaturated and crystal formation occurs.[37]

Nanomaterials with controlled size and composition can be obtained easily by modifying the reaction temperature and/or solvent used. In addition, with the utilization of different type of surfactants such as cetyltrimethyammonium bromide (CTAB), cetyl alcohol, urea or nitrilotriacetic acid (NTA) well-dispersed nanomaterials having various morphologies can be prepared.[8]
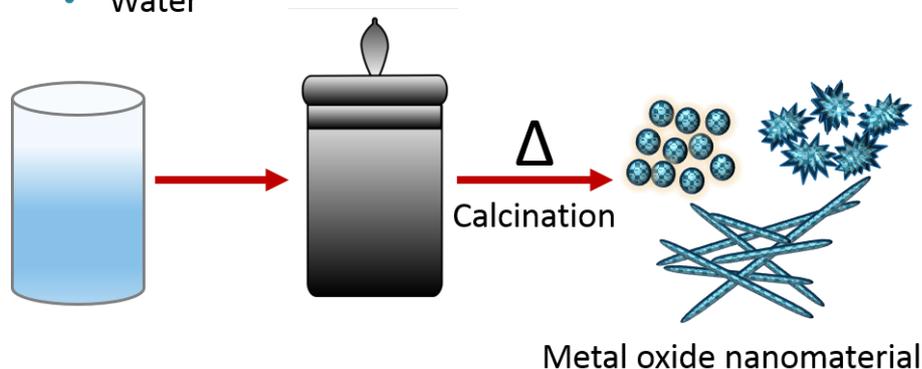
Figure 2.11. Schematic representation of hydrothermal synthesis of nanomaterials

2.4 Characterization of Transition Metal Oxide Nanomaterials

Characterization of TMO nanomaterials is as essential as preparing them with desired properties in nanoparticle research area. In order to gain valuable insights on their behavior in certain applications, one must analyze the composition, structure and morphology of the nanomaterials. Several analytical techniques can be utilized for characterization of nanomaterials.

The most common technique used is electron microscopy. *Scanning electron microscopy* (SEM) provides information about surface topography of nanoparticles by analyzing either secondary or back-scattered electrons. However, SEM does not give data on atomic scale since its resolution is ca. 5 nm. Therefore, *transmission electron microscopy* (TEM) is used in order obtain detailed information about size, shape and composition of nanoparticles and their distribution. In addition, with utilization of *high resolution TEM* (HR-TEM), diffraction patterns and lattice spacing of the nanoparticles can be obtained. *Energy dispersive x-ray spectroscopy* (EDX) can also be studied in conjunction with both SEM and TEM, which provides primitive elemental analysis of the sample.

X-Ray diffraction (XRD) is another valuable technique applied to characterize nanoparticles. Analysis of crystal structure and chemical composition of nanomaterials as well as phase of the bulk structure are possible by XRD. Moreover, the characteristic set of lattice spacings obtained from x-ray pattern can be useful for identifying the material. Determination of crystallite size of the nanomaterials is also possible with utilization of Debye-Scherrer equation (2.1).[38]

$$\tau = \frac{K\lambda}{\beta\cos\theta} \qquad (2.1)$$

where τ is the average crystallite size, K is a dimensionless shape factor (0.9), λ is the X-ray wavelength (nm), β is the line broadening (radian) at full width half maximum (FWHM) and θ is the Bragg angle.

X-Ray photoelectron spectroscopy (XPS) is utilized to investigate surface properties of the nanoparticles. Photoelectrons emitted from the surface have characteristic energy levels, which reveal the chemical and electronic state of the elements present in the material as well as their concentration and distribution across the surface. Therefore, XPS is a very useful tool for both qualitative and quantitative evaluation of surface structure of nanoparticles.

Adsorption-desorption techniques are frequently employed to acquire information about surface area, pore volume and pore size of the nanomaterials. Additionally, porosity of the materials (i.e. microporous, mesoporous or macroporous) can be determined from the obtained adsorption-desorption isotherms.

Moreover, elemental analysis techniques such as inductively coupled optical emission spectroscopy (ICP-OES), infrared spectroscopy (IR), Raman spectroscopy and scanning tunneling microscopy (STM) are other techniques that are used commonly in the characterization of nanomaterials.

CHAPTER 3

WATER SPLITTING

Concerns regarding the energy crisis that may arise in the future have led researches focus on finding and developing new energy sources. When the effect of greenhouse gases released due to extensive use of fossil fuels is taken into consideration, alternative energy sources which are environmentally sustainable and have the potential of widespread use have gained increasing attention.[39–43] In this context, renewable energy sources are particularly promising. However, in order to be used on a global scale, there are a number of problems that need to be considered.[44] Foremost is the lack of reliable methods of storing the energy generated from these sources including solar and wind. In order to overcome this problem, research has focused on storing the energy in the chemical bonds of a suitable fuel.[45]

Hydrogen, as an energy carrier, has become focus of increasing attention owing to the high energy stored in its bonds. Moreover, it serves the possibility to be obtained from readily available, abundant and renewable energy sources such as water. Water splitting in which electrons and protons are extracted is a well-known process for hydrogen generation (summarized by the following reactions).[46]

Oxidation half-reaction: $\quad 2H_2O \;\rightarrow\; O_2 + 4H^+ + 4e^-$ $\qquad$ (3.1)

Reduction half-reaction: $\quad 2H^+ + 2e^- \rightarrow H_2$ $\qquad\qquad$ (3.2)

Overall water splitting: $\quad 2H_2O \rightarrow O_2 + 2H_2$ $\qquad\qquad$ (3.3)
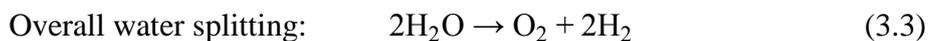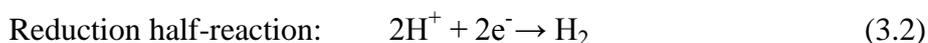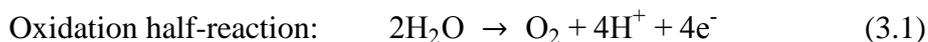
Water splitting, especially *water oxidation*, is both thermodynamically and kinetically a demanding process (non-spontaneous, $\Delta G° = 475$ kJ/mol) and needs high energy to occur. To overcome this difficulty, use of suitable catalysts is required. In nature, oxygen evolution center located in photosystem II in plants is

known to be highly efficient and extensively studied catalyst in water oxidation reaction. In this center, oxidation process occurs in the Mn_4CaO_5 clusters. Inspired by this structure in nature, research has focused on synthesis of stable and highly active catalysts. Thus, developing novel catalysts containing transition metals with higher performance for water oxidation has become very active research area.[47]

Water oxidation can be studied by three methods, namely chemical, photoelectrochemical and electrochemical oxidation. The details of these techniques are explained in the following sections.

3.1   Chemical Water Oxidation

Chemical water oxidation involves the use of sacrificial reagents. In this method, transition metals are oxidized (activated) by sacrificial reagents. Then, activated metals oxidize water to produce oxygen. Hypochlorite (ClO^-), peroxomonosulfate (HSO_5^-), sodium periodate ($NaIO_4$), cerium ammonium nitrate ($NH_4Ce(NO_3)_4$, CAN), $[Ru(bpy)_3]^{3+}$ (bpy: 2,2'-bipyridine) are commonly used examples of sacrificial reagents in water oxidation. Although chemical oxidation provides information on catalyst performance in a simple and rapid way, there are some limiting factors. Sacrificial reagents are consumed irreversibly during the reaction; therefore, it brings out the possibility that oxygen produced may contain one oxygen atom from this reagent. In addition, sacrificial reagents cause the catalyst to decompose, resulting in depletion of catalyst activity and/or transformation of the catalyst to another material.[48,49] Since sacrificial reagents are used in larger amount compared to the catalyst, they affect the catalyst stability and thus, cause misinterpretation of the experimental results.

3.2   Photoelectrochemical Water Oxidation

In this method, catalysts are activated via light which later oxidize water. Metal-semiconductor composites (i.e Pt/TiO$_2$) can be used as catalysts in which

semiconductor component is the photocatalyst while metal one is the co-catalyst.[48] When exposed to light with energy higher than its band gap ($h\nu > E_{gap}$), an electron is ejected from the valence band (V.B.) of the photocatalyst and migrates to the conduction band (C.B.) forming an electron-hole pair. Then, water adsorbed on the positively charged holes is oxidized while protons are reduced by the electrons transferred to the co-catalyst. In addition to metal-semiconductor composites, three component system which includes a photosensitizer (i.e. $[Ru(bpy)_3]^{3+}$), a molecular catalyst and a sacrificial electron acceptor (i.e. $S_2O_8^{2-}$, $[Co(NH_3)_5Cl]^{2+}$, $[Co(bpy)_3]^{3+}$, $[Co(phen)_3]^{3+}$ (phen:phenanthroline)) can be used in photochemical water oxidation. Once the photosensitizer is excited with light, electron transfer occurs to sacrificial electron acceptor. Oxidized photosensitizer then activates the catalyst and thus, catalytic cycle is initiated. However, due to the reactive singlet oxygen produced during the process, stability of the photosensitizer is affected.[46]
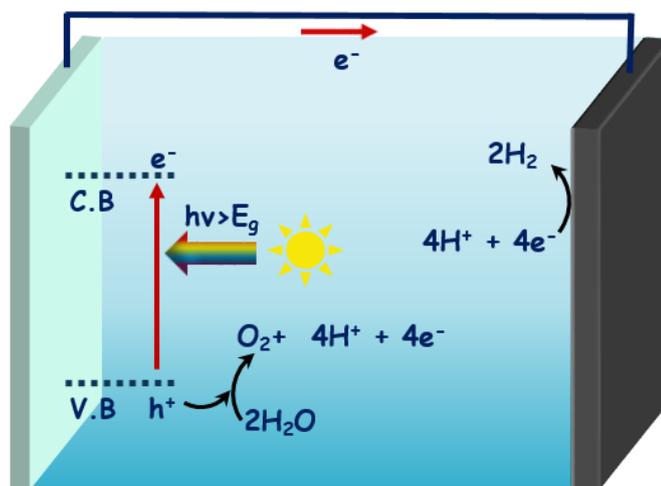
Figure 3.1. Schematic representation of photoelectrochemical water oxidation

3.3 Electrochemical Water Oxidation

In addition to chemical and photochemical methods, water oxidation can be studied via electrochemical oxidation. In this method, catalysts are used as anode materials. Catalysts are oxidized with the applied potential. Then, the activated catalyst causes water molecules to oxidize. The most significant advantage of electrochemical oxidation is that the system being studied shows resemblance to conditions of solar fuel generation cell.[49] This provides a practical way to analyze the activities of systems which will be used in photochemical and/or electrophotochemical water oxidation. Therefore, stable catalysts which are proven to be efficient through electrochemical oxidation are considered as important prototypes for the ones to be developed for solar fuel generation cells.
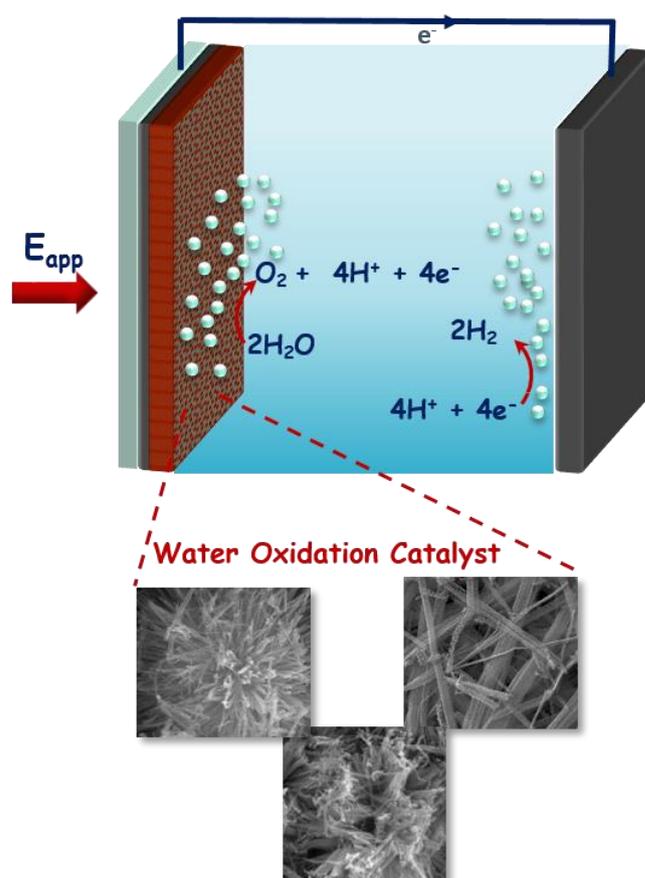
Figure 3.2. Schematic representation of electrochemical water oxidation

Water splitting is a non-spontanenous process and needs high energy because, 4 O-H bonds are cleaved for the formation of O-O bond. Therefore, water oxidation requires not only use of stable catalysts but also application of overpotential. The amount of overpotential applied is crucial for the net energy obtained from the reaction. Hence, developing catalyst which requires minimum amount of overpotential in water oxidation has become focus of this research area.

3.4   Evaluation of Water Oxidation Activity of an Electrocatalyst

The important parameters in the evaluation of water oxidation activity of a catalyst include onset potential, overpotential, Tafel slope, capacitance and stability. Several electrochemical techniques can be employed in order to determine these parameters such as linear sweep voltammetry (LSV), cyclic voltammetry (CV), electrochemical impedance spectroscopy (EIS), chronoamperometry, chronopotentiometry and/or controlled potential coulometry.

i)   *Polarization curves:* Polarization curves can be obtained by recording linear sweep voltammograms of an electrode modified with catalyst. These curves provide three important data about catalysts' activity. First one is the *onset potential*. Onset potential indicates the start of water oxidation and usually refers to the potential at a current density of 10 μA cm^{-2}.[8] It can also be determined by drawing two tangent lines; one at non-faradaic region and the other at faradaic region where increase in current density is observed. The intersection point of these two tangent lines results in onset potential (Figure 3.3).[50]
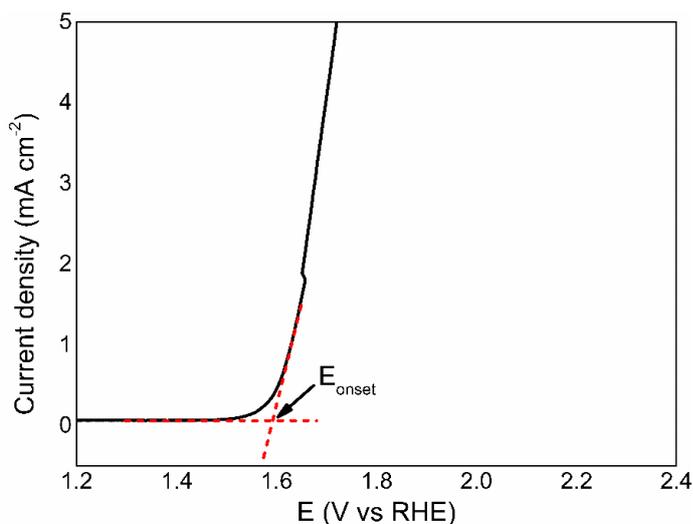
Figure 3.3. Determination of onset potential from a polarization curve

Secondly, overpotential values can also be determined from polarization curves. Ideally, the applied potential for a reaction to occur should be equal to the equilibrium potential of that reaction. However, higher potential than that of equilibrium potential is applied to surpass the kinetic barrier of the reaction.[6] This difference between the applied potential and equilibrium potential is defined as overpotential and it can be expressed by the following equation (3.4) where E is the applied potential and E_{eq} is the potential under equilibrium conditions.

$$\eta = E - E_{eq} \qquad (3.4)$$

In addition to onset potential and overpotential, Tafel slope can also be determined. In order to find Tafel slope, linear portion of polarization curves are fitted to Tafel equation (3.5) where η is the overpotential a, j and b are intercept to find exchange current density and Tafel slope, respectively).

$$\eta = a + b \cdot \log(j) \qquad (3.5)$$

The value of Tafel slope presents valuable insights about the mechanism and rate determining step of the overall reaction.[6,8]

Lower onset potential and overpotential are indications of an efficient electrocatalyst while lower Tafel slope implies faster water oxidation kinetics.

ii) *Capacitance:* Catalysts on electrode surface can act as capacitor by forming a double-layer between electrolyte and catalyst film and accumulating charge. Double-layer capacitance (C_{dl}) is directly proportional to the active surface area of the modified electrode, which gives information about the number of atoms that can act as a catalyst. The value of C_{dl} can be determined by measuring CV in a non-faradaic potential window and at various scan rates (v). The measured current is assumed to be due to double-layer charging current (i_{dl}) having the following relation (equation (3.6)).[8]

$$C_{dl} = \frac{i_{dl}}{v} \qquad (3.6)$$

The plot of i_{dl} versus v results in a straight line whose slope yield C_{dl} values of the catalysts. Electrochemically active surface area (ECSA) and roughness factor (RF) of the catalysts, which are also important parameters in the assessment of catalyst activity can be determined by equation (3.7) and (3.8), respectively.

$$ECSA = \frac{C_{dl}}{C_s} \qquad (3.7)$$

where C_s is the specific capacitance of the material.

$$RF = \frac{ECSA}{GSA} \qquad (3.8)$$

where GSA is the geometric surface area of the electrode.

Higher C_{dl}, ECSA and RF values signify the presence of large number of active sites, and thus improved catalytic performance.

iii) *Stability:* Stability of an electrocatalyst can be assessed by applying a constant potential to electrode for a long period of time. The variation in current density with time can be monitored during the long-term electrolysis. Another way is recording polarization curves before and after electrolysis in order to compare the onset potential, overpotential or

current densities. A small or no change in these parameters implies high stability of the electrocatalyst.

3.5 Motivation of the Dissertation

Together with the recent advances in technology, demand for cheap, renewable and environmentally benign energy sources in order to satisfy the energy need of the world has elevated greatly. Therefore, research on finding abundant sources that can be used in energy production has become of utmost importance. Among all, role of hydrogen, which is obtained through water splitting, in energy production has earned great deal of attention. However, water oxidation, which is one of the half reactions of water splitting, is an electrochemically difficult and energetically demanding process. Hence, this reaction limits the overall water splitting. As a result, designing and preparing catalyst systems that increase the rate of water oxidation reaction has become an active research area.

There are two main challenges that must be addressed in catalytic water oxidation reaction and for the efficient and economical production of hydrogen. Firstly, the catalyst used for this reaction should operate at low overpotentials. Secondly, it should be prepared from earth abundant and cheap elements. Therefore, researchers have focused on designing and preparing new catalyst systems to overcome these challenges. Nonetheless, the most promising results were achieved with catalysts consisting of rare and precious metals, namely Ru and Ir. Therefore, research on relatively cheaper and effective catalysts from earth abundant metals has increased greatly.

Metal oxide catalysts have been prepared as films or as nanomaterials with various morphologies such as spherical, rod, wire and plate and used as water oxidation electrocatalysts. Among these diverse structures, nano-sized ones are of great interest since they have the potential to be very active catalysts caused by their large surface area. Recently, bimetallic oxides with spinel or perovskite structures have

28

particularly drawn attention. Transition metals in such structures can have multiple oxidation states and different coordination environments. This brings the possibility to be prepared in various combinations of metals with enhanced stability and activity in catalysis applications.

The purpose of this dissertation is to develop new catalyst systems consisting of earth abundant, first row transition metal oxide nanomaterials as well as to investigate their electrocatalytic activities towards water oxidation reaction. Specifically, the following studies were performed in this dissertation;

i) Synthesis of bimetallic oxide nanomaterials with earth abundant first row transition metals which are known to be stable and catalytically active in $CuCr_2O_4$, $FeMnO_3$, $NiFe_2O_4$-NiO and $NiCo_2O_4$-NiO structures with various morphologies such as spherical, wire and plate by facile and reproducible methods namely, sol-gel and hydrothermal routes.

ii) Characterization of the synthesized nanomaterials by a combination of analytical techniques including XRD, SEM, TEM, EDX, XPS, ICP-OES and BET.

iii) Preparation of electrodes by modifying conductive surfaces such as FTO and GC with synthesized nanomaterials.

iv) Investigation of the catalytic performance of nanomaterials in electrochemical water oxidation reaction.

CHAPTER 4

EXPERIMENTAL

4.1   Materials

All reagents were used as received without further purification. Copper(II) acetate hydrate ($Cu(OAc)_2.H_2O$), chromium(III) acetylacetonate ($Cr(acac)_3$), manganese(II) chloride tetrahydrate ($MnCl_2.4H_2O$), iron(II) chloride tetrahydrate ($FeCl_2.4H_2O$), iron(II) nitrate hexahydrate ($Fe(NO_3)_2.6H_2O$), cobalt(II) nitrate hexahydrate ($Co(NO_3)_2.6H_2O$), nickel(II) nitrate hexahydrate ($Ni(NO_3)_2.6H_2O$), citric acid, nitrilotriacetic acid (NTA), urea, cetyltrimethylammonium chloride (CTAC), 2-propanol, dimethyl formamide (DMF), acetylacetone, polyethylene oxide (PEO), Triton™ X, and Nafion® perfluorinated resin solution (5% wt in lower aliphatic alcohols and water) were purchased from Sigma Aldrich. Deionized water with resistivity greater than 18 MΩ (PURELAB Option-Q, ELGA) was used in the preparation of solutions throughout this study.

4.2   Synthesis of the Transition Metal Oxide Nanomaterials

4.2.1   Synthesis of $CuCr_2O_4$ nanoparticles

Synthesis of $CuCr_2O_4$ nanoparticles were carried out by using a previously reported sol-gel method with some modifications.[51] Briefly, 0.005 moles of $Cu(Ac)_2.H_2O$ and 0.01 moles of $Cr(acac)_3$ were dissolved in 50 mL deionized water and stirred vigorously until complete dissolution. Then, 0.03 moles of citric acid was added onto the solution and stirred until a homogeneous mixture was obtained. The solution was maintained at room temperature for 30 min and then heated at 95 °C for 2 h. Obtained gel was dried in oven at 160 °C for 2 h. After drying, the citrate precursors were

calcined to eliminate the organic materials.[52] After calcination at 600 °C for 3h, $CuCr_2O_4$ nanoparticles were obtained as black powder.

4.2.2   Synthesis of FeMnO₃ nanowires

Synthesis of $FeMnO_3$ nanowires was carried out using a previously reported solvothermal method with some modifications.[5] Briefly, $FeCl_2.4H_2O$ (3.0 mmol), $MnCl_2.4H_2O$ (6.0 mmol) and NTA (4.7 mmol) were added to 30.0 mL 2-propanol and 10.0 mL deionized water mixture. After complete dissolution, the reaction mixture was transferred to a 100 mL Teflon line autoclave, which was heated to 180 °C and kept at this temperature for 6 h. The product was collected by centrifugation, and washed with deionized water and ethanol for several times. After calcination at 650 °C for 1 h, $FeMnO_3$ nanowires were obtained as brown powder.

4.2.3   Synthesis of NiFe₂O₄-NiO nanoparticles

$NiFe_2O_4$-NiO nanoparticles were synthesized by a simple hydrothermal route based on a procedure reported previously.[53] In brief, 2.0 mmoles of $Fe(NO_3)_2.6H_2O$, 4.0 mmoles of $Ni(NO_3)_2.6H_2O$ and 12.0 mmoles of urea were dissolved in 40.0 mL of deionized water and stirred until a homogenous solution is obtained. Then, the solution was transferred a 100 mL Teflon lined autoclave and kept at 180 °C for 6 h. After the solution cooled down to room temperature, the product was separated by centrifugation and washed with deionized water and ethanol for several times. Finally, the product was dried at 90 °C followed by calcination step at 550 °C for 2 h.

4.2.4 Synthesis of NiCo$_2$O$_4$-NiO microspheres

Hierarchical NiCo$_2$O$_4$-NiO biphasic microspheres were synthesized with two different morphologies by using different structure directing agents, namely urea and CTAC.

4.2.4.1 Synthesis of urea-stabilized NiCo$_2$O$_4$-NiO microspheres

Synthesis of urea-stabilized NiCo$_2$O$_4$-NiO (U-NiCo) nanomaterials was achieved by a simple hydrothermal method reported in the literature with some modifications.[53] Briefly, Co(NO$_3$)$_2$.6H$_2$O (2.0 mmol), Ni(NO$_3$)$_2$.6H$_2$O (4.0 mmol) and urea (12 mmol) were dissolved in 40 mL deionized water. The obtained solution was transferred to a 100 mL Teflon-lined autoclave and kept at 180 °C for 6 h. The precipitate was separated from the mixture by centrifugation, and washed with deionized water and ethanol for several times. After drying at 90 °C, the resulting powder was calcined at 550 °C for 2 h.

4.2.4.2 Synthesis of CTAC-stabilized NiCo$_2$O$_4$-NiO microspheres

CTAC-stabilized NiCo$_2$O$_4$-NiO (C-NiCo) nanomaterials were prepared according to the hydrothermal process described above with some modifications.[5] In brief, Co(NO$_3$)$_2$.6H$_2$O (3.0 mmol), Ni(NO$_3$)$_2$.6H$_2$O (6.0 mmol) and CTAC (4.7 mmol) were dissolved in a mixture of 2-propanol (30.0 mL) and deionized water (10.0 mL). Then, the reaction mixture was heated to 180 °C for 6 h in a 100 mL Teflon lined autoclave. The precipitate was collected by centrifugation, followed by washing with deionized water and ethanol for several times. After drying at 90 °C, the resulting powder was calcined at 550 °C for 2 h.

4.3   Materials Characterization

SEM images, EDX measurements along with elemental composition analysis were acquired by FEI Nova Nano SEM 430. TEM was carried out on JEM 2100F-RTEM and FEI Tecnai G2 F30 electron microscope operating at 300 kV. Rigaku Ultima IV X-ray diffractometer with Cu Kα radiation (λ = 1.54 Å) was utilized to examine the phase of the nanomaterials in the 2θ range from 10º to 80º. XPS analyses were carried out on PHI-5000 VersaProbe [Physical Electronics (PHI) Chanhassen, Minneapolis, MN], equipped with Al Kα at 1486.92 eV source. All data were calibrated to the hydrocarbon contamination peak at C1s of 282.4 eV. Autosorb-6 (Quantachrome Coporation) instrument was used for nitrogen adsorption-desorption experiments and BET analysis. $CuCr_2O_4$ nanoparticles were dehydrated at 200 °C for 3 h, while $FeMnO_3$ nanowires, $NiCo_2O_4$-NiO microspheres and $NiFe_2O_4$-NiO nanoparticles were dehydrated at 350 °C for 3 h before analysis. Elemental composition and mass percent of each element in the structure of nanomaterials were investigated by ICP-OES with Perkin Elmer Optima 4300DV.

4.4   Electrochemical Characterization

4.4.1   Electrode preparation

In this study, GCEs (0.07 cm^2) were used in the investigation of electrochemical behaviors of $CuCr_2O_4$ nanoparticles, $NiCo_2O_4$-NiO microspheres and $NiFe_2O_4$-NiO nanoparticles, while for $FeMnO_3$ nanowires, FTO coated glass electrodes (0.5 cm^2) were modified and used as working electrodes.

A modified method previously reported by Kuo et al was used in the preparation of GCEs.[54] Briefly, 11.2 mg of catalyst was dispersed in 2.0 mL of DMF by sonication. After 30 min., 19 µL Nafion® solution was added and sonicated for 2 h resulting in a homogeneous ink. 5.0 µL of the ink was dropped onto GCE and dried in an oven at 90 °C overnight. Mass loading of ca. 0.4 mg cm^{-2} was obtained.

Preparation of FTO electrodes were carried out according to a previously reported method.[55] Before catalyst loading, FTO coated glass was cleaned by sonication in dilute H_2SO_4 solution for 30 min and treated at 400 °C for 30 min. Then, 100 mg of catalyst and 30 mg of PEO were dispersed in 100 µL of Triton™ X, 100 µL of acetylacetone and 1.0 mL of deionized water mixture under vigorous stirring for 24 h. 5.5 µL of the ink was transferred onto FTO glass to obtain a catalyst loading of ca. 0.92 mg cm^{-2}.
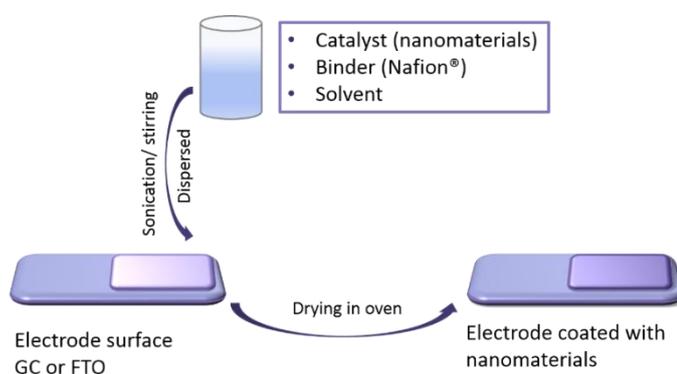
Figure 4.1. Schematic representation of modified electrode preparation

4.4.2   Electrochemical measurements

Electrochemical studies were conducted by using a Gamry 1010B potentiostat-galvanostat and a standard three-electrode system (Figure 4.2). In this system, Pt wire and Ag/AgCl (in 3.0 M KCl) were used as counter electrode (CE) and reference electrode (RE), respectively. GCEs coated with $CuCr_2O_4$ nanoparticles, $NiCo_2O_4$-NiO microspheres and $NiFe_2O_4$-NiO nanoparticles and FTO modified with $FeMnO_3$ nanowires were used as working electrodes (WE).
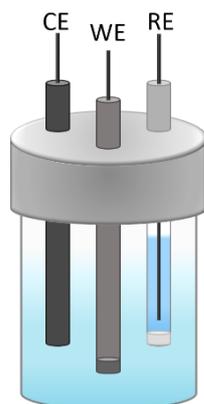
Figure 4.2. Schematic representation of a standard three-electrode system used for the electrochemical studies of electrodes modified with nanomaterials

Electrochemical behavior of the modified electrodes was investigated in 0.1 M KOH solution at room temperature. Polarization curves were recorded at a scan rate of 5 mV s^{-1}. All potentials, measured in this work were corrected for iR drop, and reported against reversible hydrogen electrode (RHE). The conversion of the obtained potential (vs Ag/AgCl) was carried out according to Nernst equation (4.1) and overpotential, η was calculated using equation (4.2).

$$E_{RHE} = E_{Ag/AgCl} + 0.059 \text{ pH} + E°_{Ag/AgCl} \qquad (4.1)$$

$$\eta = E_{RHE} - 1.23 \text{ V} \qquad (4.2)$$

The water oxidation kinetics of the nanomaterials were elucidated by fitting the linear part of polarization curves to Tafel equation (equation (3.5)) where η is the overpotential, a, j and b are intercept to find exchange current density (j_0), current density and Tafel slope, respectively.

The stability of the modified electrodes was investigated via constant potential electrolysis at certain overpotentials which correspond to current densities of 5 mA cm^{-2} in 0.1 M KOH. Electrochemical impedance spectroscopy (EIS) analyses were carried out at various potentials in the frequency range of 0.1 Hz – 100 kHz and with an amplitude of 10 mV.

36

Electrochemically active surface area (ECSA) of the catalysts were estimated by determining the electrochemical double-layer capacitance (C_{dl}). The values of C_{dl} were determined by recording cyclic voltammograms (CVs) at non-Faradaic potential window (1.177-1.277 V vs RHE) and at various scan rates (5-10-15-20-25 mV s^{-1}). The plot of double-layer charging current (at 1.27 V vs RHE) versus scan rate resulted in a straight line whose slope yield C_{dl} values of the catalysts. The ECSA values were then determined by using equation (3.7). C_s is the specific capacitance of the sample where $C_s = 0.06$ mF cm^{-2} for smooth metal oxide surfaces.[56,57]

Surface roughness factor (RF) was calculated by dividing ECSA of the catalyst to the geometric surface area (GSA) of the electrode (equation (3.8)).

Mass activity (A g^{-1}) values were determined according to equation (4.3) by using the catalyst loading, m (mg cm^{-2}) and current density, j (mA cm^{-2}) at a certain overpotential.

$$\text{Mass activity} = \frac{j}{m} \qquad\qquad (4.3)$$

Specific activity (mA cm$^{-2}_{ECSA}$) was calculated by using equation (4.4) where i is the observed current at a certain potential.[29]

$$\text{Specific activity} = \frac{i}{ECSA} \qquad\qquad (4.4)$$

Water oxidation activity of FTO modified with FeMnO$_3$ nanowires were tested by measuring the volume of O$_2$ gas evolved during electrolysis at a constant current of 5 mA for 1 h using a Hoffmann electrolysis apparatus (Figure 4.3). Faradaic yield, which is described as the ratio of the amount of O$_2$ gas generated experimentally to the theoretical amount, was calculated. Theoretical amount of O$_2$ was determined by using the following relations:

i.   By using Faraday's relation (equation (4.5)) amount of charges (Q) passing through the system was calculated, where i is the current (A) and t is time (s).

$$Q = i.t \qquad\qquad (4.5)$$

ii.   Mole of O_2 ($n(O_2)$)was calculated by equation (4.6) where n_{e^-} is the mole of electrons passing the system for O_2 generation (4 moles) and F is the Faraday's constant (96485 C mol^{-1}).

$$n(O_2)=\frac{Q}{n_{e^-}\times F} \qquad\qquad (4.6)$$

iii.   Theoretical volume of O_2 ($V(O_2)$) was calculated using ideal gas law (equation 4.7) where P is atmospheric pressure which is 0.9 atm in Ankara, T is temperature (K) and R is the ideal gas constant (0.082 L atm mol^{-1} K^{-1}).

$$P\,V(O_2)= n(O_2)RT \qquad\qquad (4.7)$$
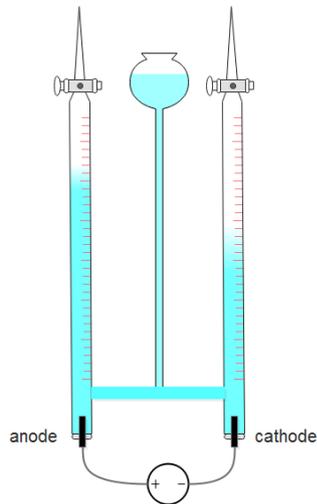
Figure 4.3. Schematic representation of a Hoffmann electrolysis apparatus

CHAPTER 5

RESULTS AND DISCUSSION

5.1   Characterization of Transition Metal Oxide Nanomaterials

5.1.1   Characterization of $CuCr_2O_4$ Nanoparticles

$CuCr_2O_4$ nanoparticles were synthesized by modified sol-gel method. The formation of nanoparticles took place in aqueous medium where citric acid function as chelating agent (Figure 5.1). TEM images of the as-synthesized $CuCr_2O_4$ nanoparticles are displayed in Figure 5.2a-c. The images show that $CuCr_2O_4$ particles have quasi-spherical morphology with average size of 28 nm ± 6 nm. The particle size distribution histogram is given in Figure 5.2d. The spacing between lattice fringes is measured as 3.5 Å, which is in agreement with the d-spacing of (220) plane of $CuCr_2O_4$.[58] EDX analysis performed in conjunction with SEM verifies the presence of Cu and Cr in the nanoparticles (Figure 5.3).
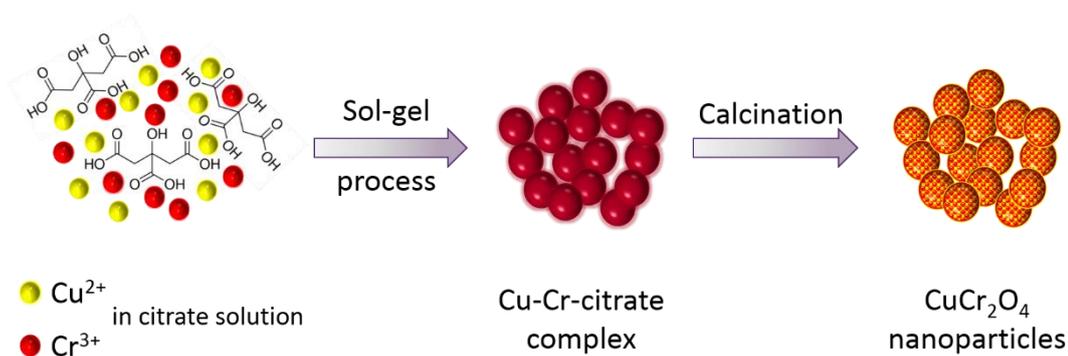
Figure 5.1. Illustration for the formation of $CuCr_2O_4$ nanoparticles
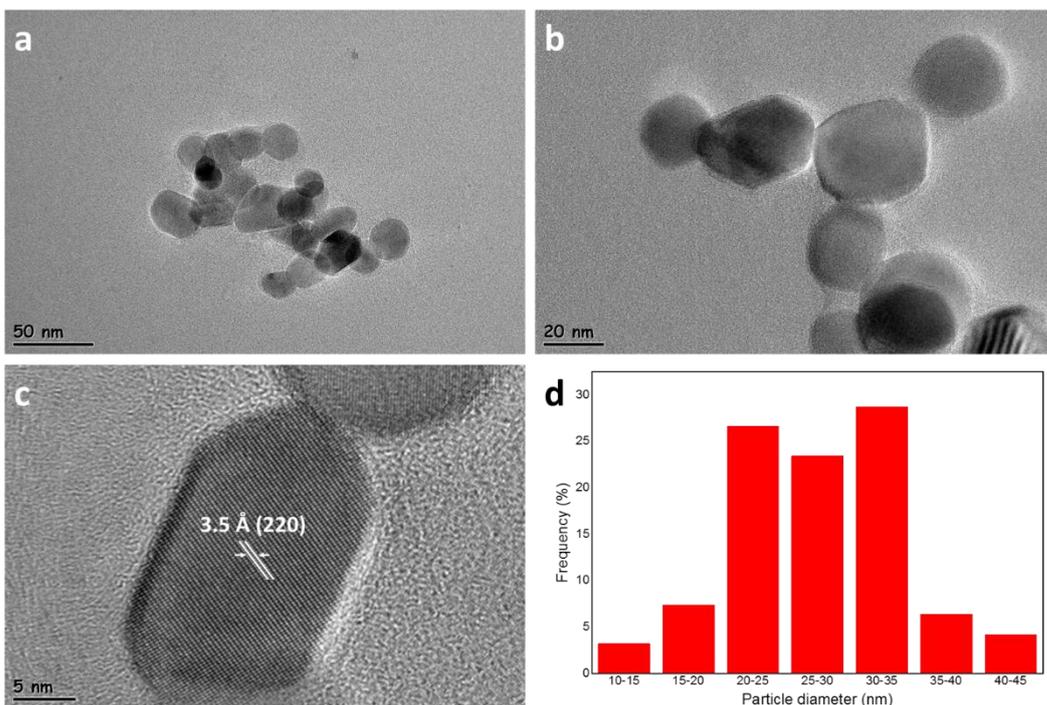
Figure 5.2. (a-c) TEM images and (d) particle size distribution graph of $CuCr_2O_4$ nanoparticles

Element	Wt %	At %
CrK	51.95	56.92
CuK	48.05	43.08
Total	100.00	100.00
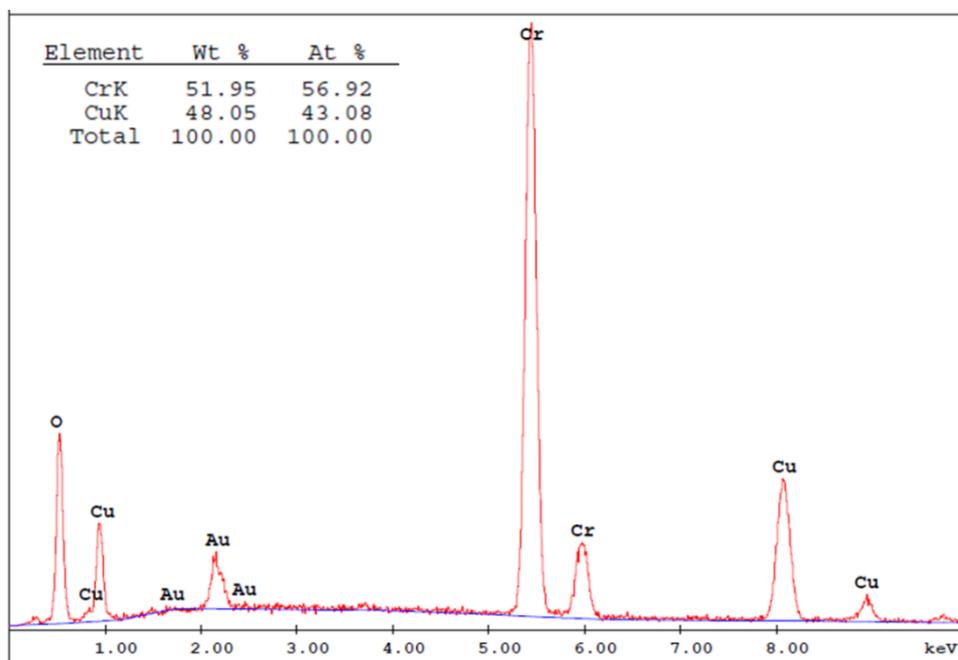
Figure 5.3. EDX spectrum of $CuCr_2O_4$ nanoparticles

The XRD pattern of $CuCr_2O_4$ nanoparticles is shown in Figure 5.4. The peaks with 2θ values of 31.23°, 35.36°, 37.83°, 56.37° and 64.94° correspond to the (112), (211), (202), (321) and (411) planes of cubic $CuCr_2O_4$, respectively (JCPDS 34-0424). Lack of secondary phase diffractions due to the impurities of oxides of Cu and Cr indicates that obtained nanoparticles are purely spinel $CuCr_2O_4$. The sizes of the crystallites are estimated with XRD peak analysis as ca. 35 nm. The analysis was done for the diffraction peak at 35.36° ((211) plane) by using Debye-Scherrer equation (equation 2.1).[38] This value is consistent with the results obtained by TEM analysis.
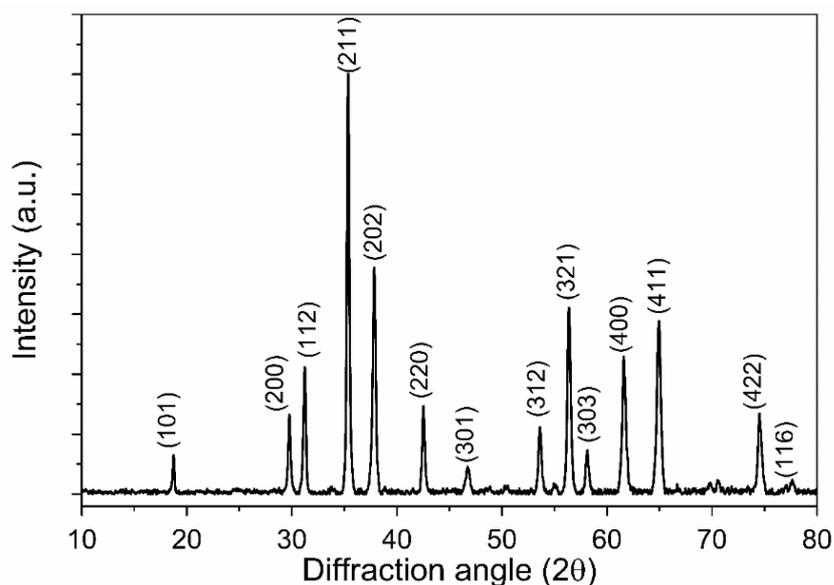
Figure 5.4. XRD pattern of $CuCr_2O_4$ nanoparticles (JCPDS 34-0424)

The O 1s, Cu 2p, Cr 2p along with survey XPS spectra of $CuCr_2O_4$ nanoparticles are demonstrated in Figure 5.5 and 5.6. The survey spectrum suggests the presence of only Cu, Cr and O. No species contaminating the synthesized nanoparticles are observed, except low amount of carbon (C1s at 282.3 eV) used for calibration (Figure 5.5). Cu 2p core level spectrum shows two characteristic peaks corresponding to Cu $2p_{3/2}$ at binding energies of 932.0 eV and 929.4 eV (Figure

5.6a). The strong satellite features, which are on the high-binding energy side, indicate the presence of copper in oxidation state of +2. The low-energy Cu $2p_{3/2}$ peak at 929.4 eV is attributed to Cu^{2+} in octahedral voids while the high-energy Cu $2p_{3/2}$ at 932.0 eV is assigned as Cu^{2+} in tetrahedral voids. The observed Cu $2p_{3/2}$ peaks verify the presence of $CuCr_2O_4$ spinel structure.[58–60] Figure 5.6b shows Cr 2p core level spectrum. The two peaks corresponding to $2p_{1/2}$ and $2p_{3/2}$ are observed at 583.2 eV and 573.3 eV, respectively. Further resolution of these peaks reveal two Gaussian bands which are ascribed to Cr^{3+} (582.9 eV and 573.0 eV) and Cr^{6+} (584.4 eV and 574.1 eV). [61,62] Presence of Cr^{6+} in $CuCr_2O_4$ structure is unexpected. The possible reason for observing this ion may be due to the oxidation of Cr^{3+} species on the nanoparticles' surface.[61] The O 1s spectrum given in Figure 5.6c demonstrates a peak around 527.3 eV, which is further resolved to three Gaussian bands. The one observed at 527.2 eV (I) is attributed to metal-oxygen bonds, while the ones at 528.1 eV (II) and 529.1 eV (III) are assigned to defect sites with low oxygen coordination and surface adsorbed oxygen species (O_2^{2-}, OH^-) on the materials' surface, respectively.[23,29,63,64]
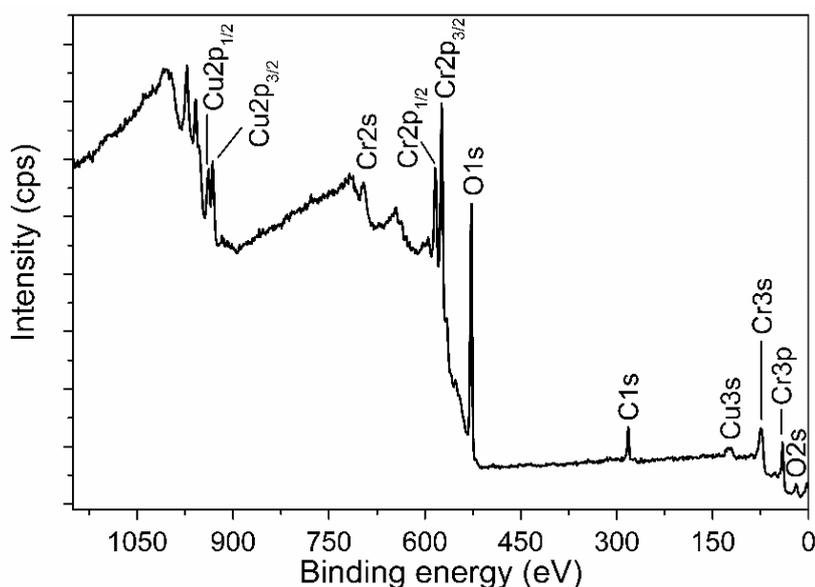
Figure 5.5. XPS survey spectrum of $CuCr_2O_4$ nanoparticles
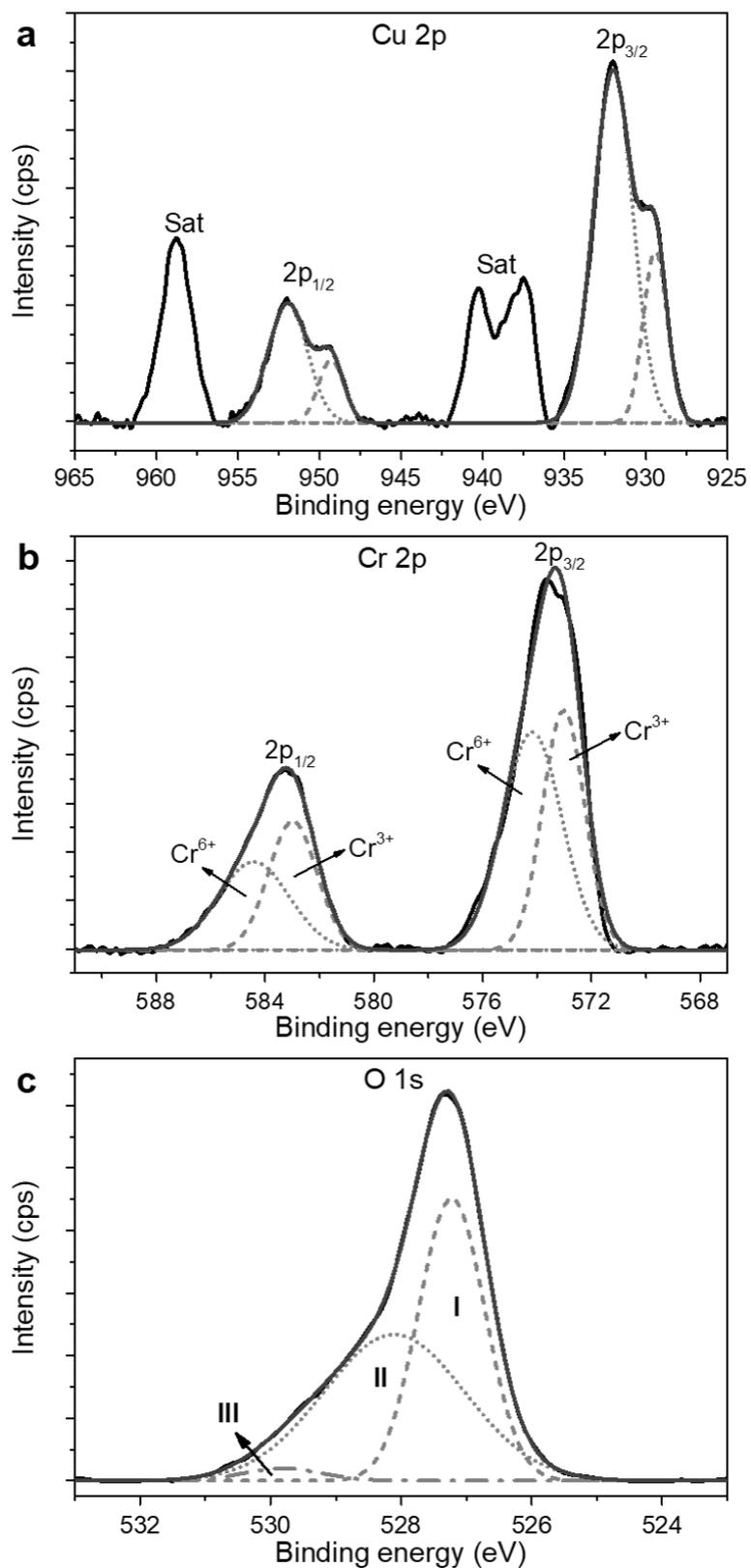
Figure 5.6. XPS (a) Cu 2p, (b) Cr 2p and (c) O 1s spectra of $CuCr_2O_4$ nanoparticles

Elemental composition and mass percent of each element present in the nanomaterials were investigated by ICP-OES. The amount of Cu and Cr in $CuCr_2O_4$ nanoparticles as wt% were determined as 24.6 ± 0.5 and 38.8 ± 0.3, while theoretically they were calculated as 27.4 % and 44.9 %, respectively. The most likely reason for the observed difference in the amount of Cu and Cr is the solubility problem of the sample encountered during analysis. Even though a percent error of 10.3 % and 13.6 % were obtained for Cu and Cr, respectively, relative molar ratio of the elements are consistent with the expected 1:2 (Cu:Cr) ratio.

N_2 adsorption-desorption analysis was performed in order to examine BET surface area and pore size of the synthesized nanoparticles. $CuCr_2O_4$ nanoparticles exhibit BET surface area of 10.63 m^2 g^{-1}. The observed isotherm (Figure A.1) indicate the mesoporous nature of $CuCr_2O_4$ nanoparticles. Moreover, large surface area and porosity are also important parameters in catalysis since they promote the interaction between catalyst and reactants/reaction intermediates, and thus enhance catalyst activity.

5.1.2 Characterization of FeMnO₃ nanowires

The synthesis of $FeMnO_3$ nanowires was performed with a simple modified hydrothermal method. Formation of the nanowires took place in isopropyl alcohol and deionized water mixture where NTA function as structure directing agent. As illustrated in Figure 5.7, after dissolution of metal salts, the transition metal ions react with NTA to form FeMn-NTA complex during hydrothermal reaction. Then, through calcination $FeMnO_3$ nanowires are synthesized.
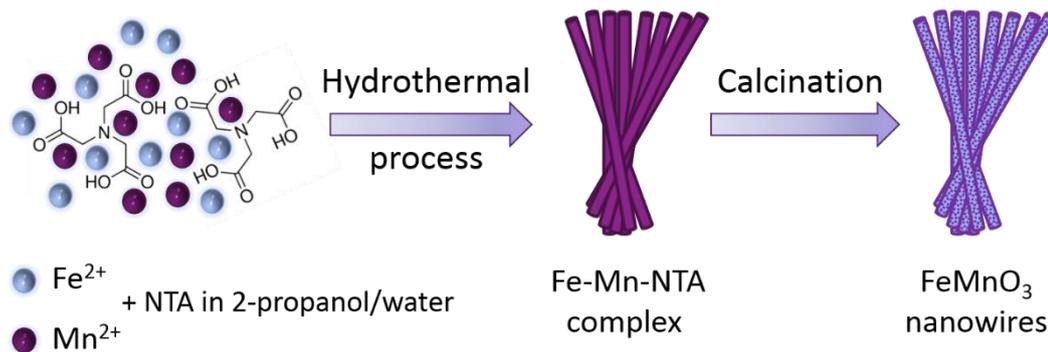
Figure 5.7. Illustration for the formation of $FeMnO_3$ nanowires

Figure 5.8 shows SEM and TEM images of $FeMnO_3$ nanowires. The images reveal that about 70 nm size nanoparticles assemble to form the wires. The images also demonstrate that the nanowires have several micrometers of length and approximately 200 nm of thickness. EDX analysis verifies the presence of Fe and Mn in the synthesized nanowires (Figure 5.9). The composition of the $FeMnO_3$ nanowires was studied by the elemental mapping of Fe, Mn and O elements on the nanowires (Figure 5.8g). The mapping reveal that the elements forming the nanowires are uniformly distributed across the whole material.
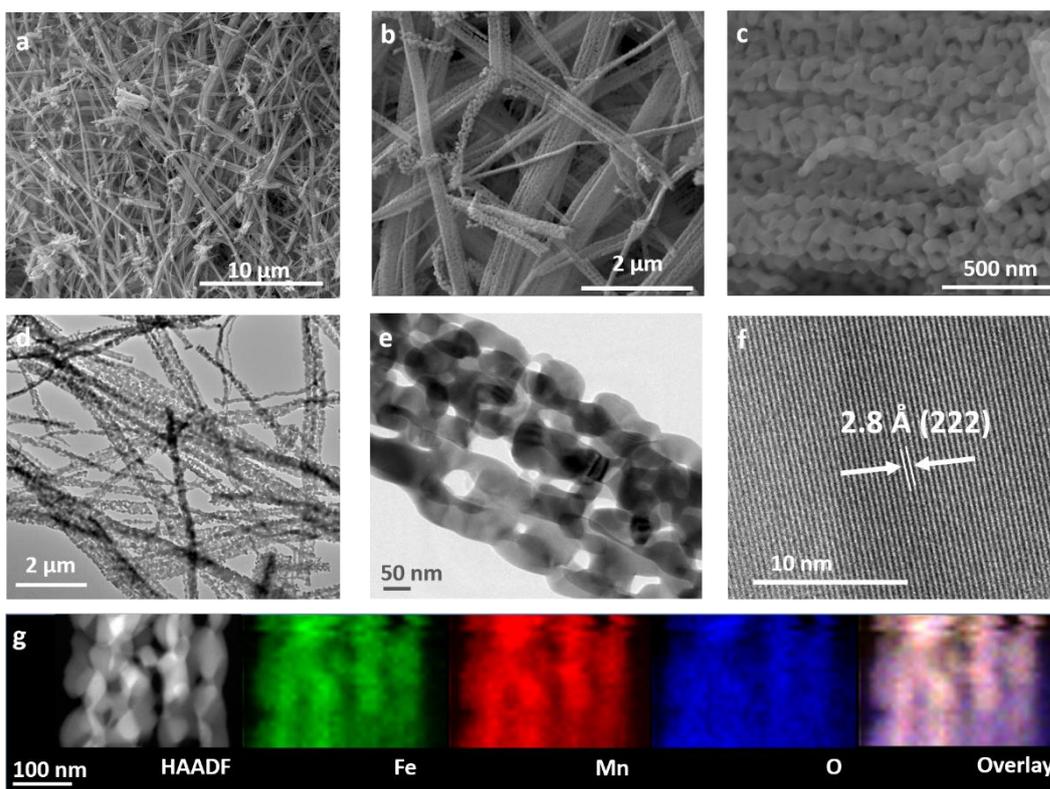
Figure 5.8. (a-c) SEM images and (d-f) TEM images at different magnifications, (g) HAADF-STEM image and element mapping (Fe (green), Mn (red) and O (blue)) of FeMnO$_3$ nanowires
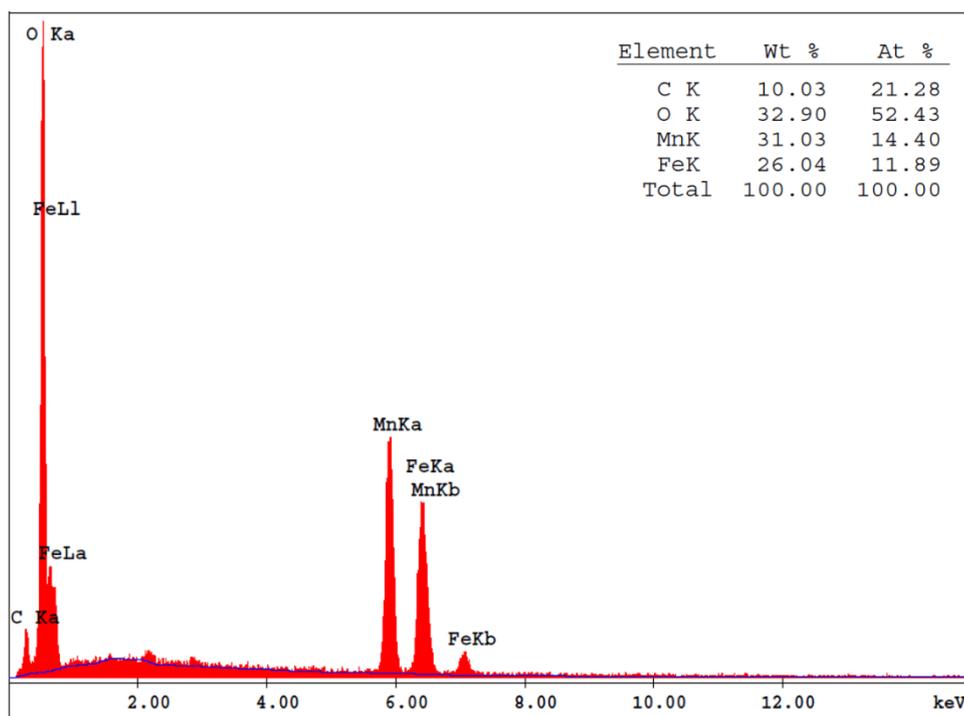
Figure 5.9. EDX spectrum of FeMnO$_3$ nanowires

The XRD pattern of nanowires is shown in Figure 5.10. The peaks with 2θ values of 23.16°, 32.96°, 35.65°, 38.24°, 40.65°, 42.98°, 45.18°, 47.23°, 49.34°, 53.28°, 55.16°, 57.06°, 58.82°, 60.58°, 62.37°, 64.06°, 65.76°, 67.42°, 69.08°, 70.72°, 72.33°, 74.00° and 75.54° were indexed to the (211), (222), (320), (400), (411), (420), (332), (422), (134), (125), (440), (433), (600), (611), (026), (145), (622), (136), (444), (543), (046), (721) and (642) planes of FeMnO$_3$ bixbyite structure (PDF number 01-076-0076), respectively. No diffraction peaks other than those of FeMnO$_3$ were observed in the XRD pattern. XRD peak analysis was performed for the diffraction peak at 32.96° (222), using the Debye-Scherrer equation to estimate crystallite size.[38] The analysis revealed that sizes of the crystallites are ca. 46.8 nm for FeMnO$_3$ nanowires. The crystallite sizes are slightly smaller than particle sizes measured by TEM analysis.
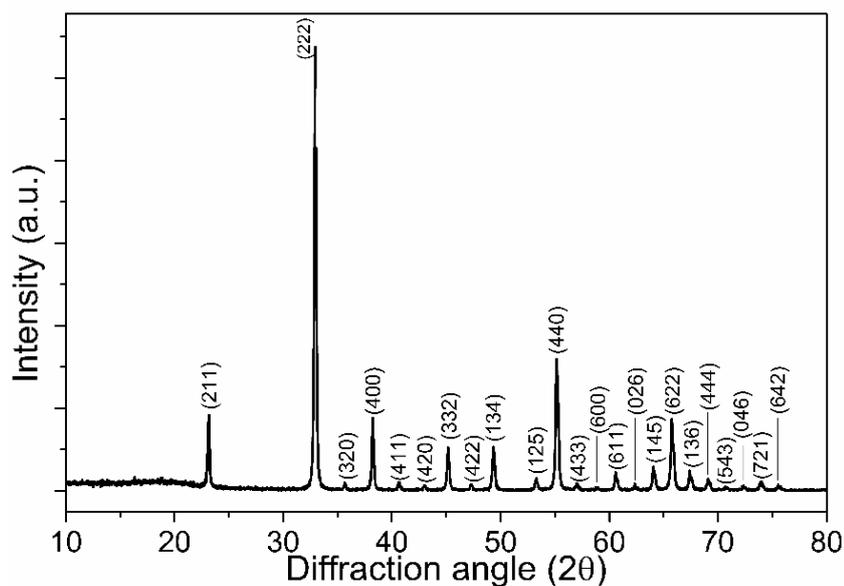
Figure 5.10. XRD pattern of FeMnO₃ nanowires (PDF number 01-076-0076)

The XPS spectra of FeMnO₃ nanowires are demonstrated in Figures 5.11 and 5.12. The survey spectrum of nanowires suggests the presence of only Mn, Fe and O elements (Figure 5.11). Only contamination observed in the sample was low quantity of carbon (C1s at 282.4 eV) which is used for calibration. Fe 2p core-level spectrum demonstrates two peaks at binding energies of 708.4 eV and 722.1 eV corresponding to Fe $2p_{3/2}$ and Fe $2p_{1/2}$ peaks, respectively (Figure 5.12a). The Gaussian fit unveiled two bands under Fe 2p peaks, which are ascribed to Fe^{2+} (708.0 eV and 721.9 eV) and Fe^{3+} (709.7 eV and 724.3 eV). The observed peaks and their positions agree well with the ones reported previously.[61,65–67] Mn 2p core-level spectrum is demonstrated in Figure 5.12b. The spectrum shows two major peaks at 638.9 eV and 650.8 eV, which are assigned as Mn $2p_{3/2}$ and Mn $2p_{1/2}$, respectively. Mn 2p peaks were resolved further and fitted bands of Mn^{3+} (638.8 eV and 650.5 eV) and Mn^{4+} (640.0 eV and 651.6 eV).[61,65,68] The O 1s spectrum exhibits a peak at 527.3 eV (Figure 5.12c). The curve-fitting process revealed two Gaussian (I and II) bands. The one at 527.2 eV (I) corresponds to metal-oxygen bonding in the sample while the one at

48

528.4 eV (II) is assigned to surface adsorbed oxygen species (i.e. O_2^{2-}, OH^-) suggesting the presence of low oxygen coordination sites in the nanowires.[65,66,68–70]
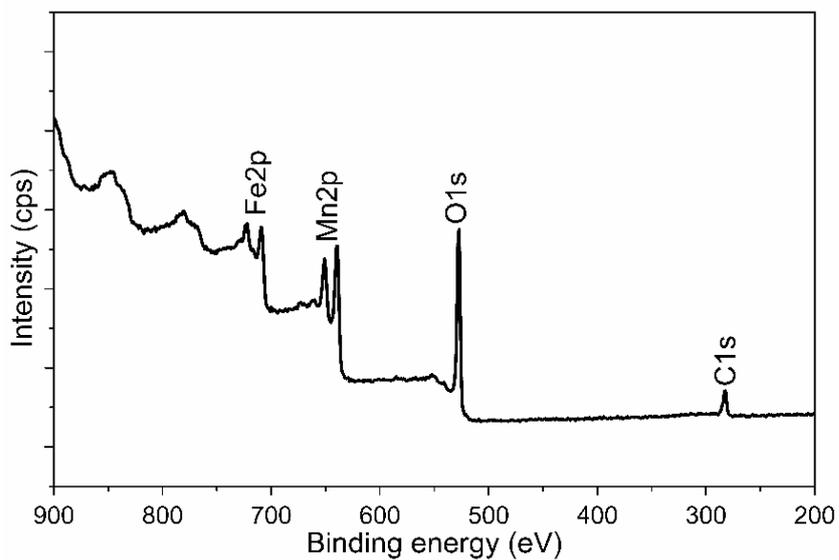
Figure 5.11. XPS survey spectrum of FeMnO$_3$ nanowires
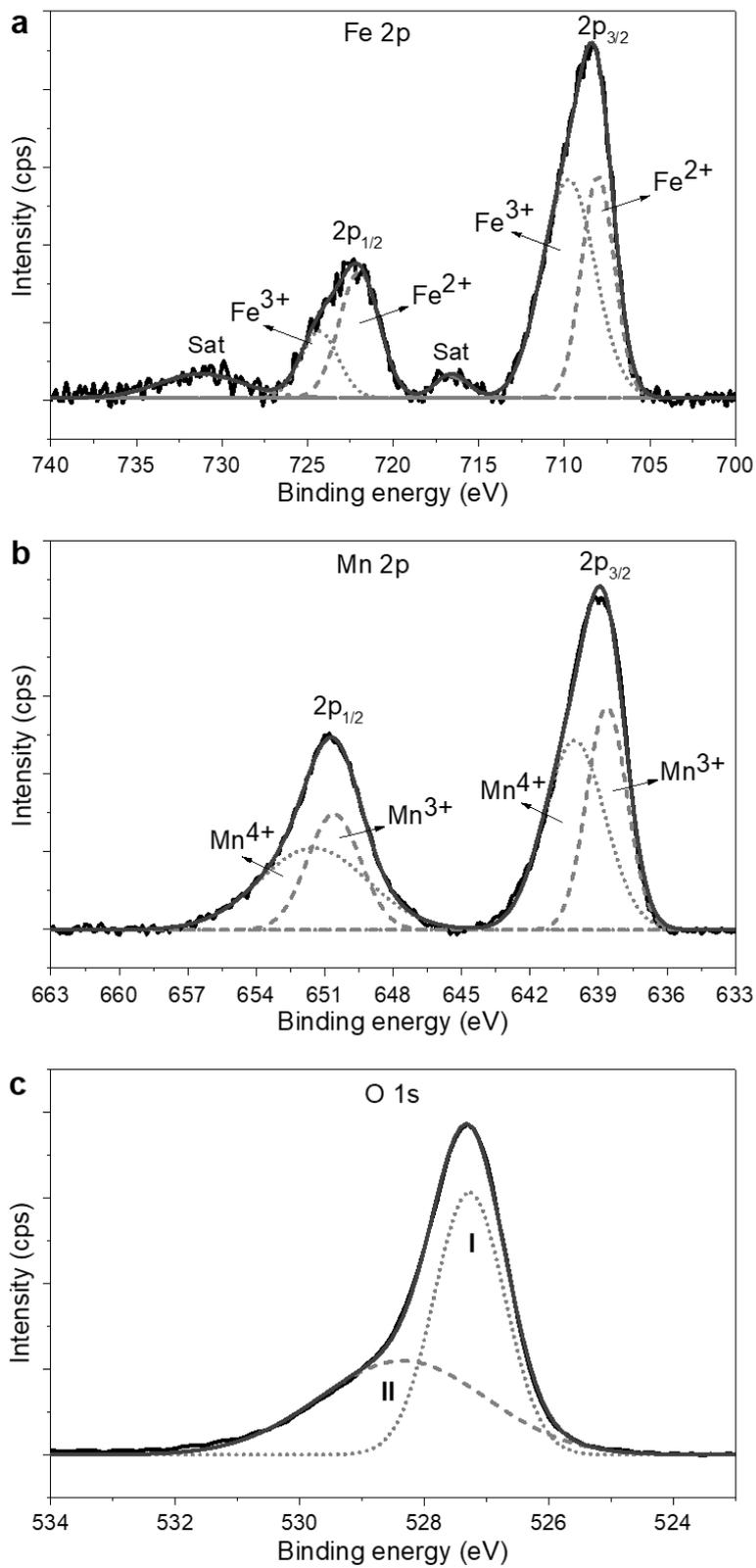
Figure 5.12. XPS (a) Fe 2p, (b) Mn 2p and (c) O 1s spectra of FeMnO$_3$ nanowires

Elemental composition and mass percent of each element in the nanowires were investigated by ICP-OES, and the amount of Mn and Fe found to be 36.6 wt% and 29.2 wt%, respectively. However, theoretical values for Mn wt% and Fe wt% were determined to be 34.6 % and 35.2 %, respectively. Similar to the ones of $CuCr_2O_4$ nanoparticles, for this material too ICP-OES analysis resulted in a 17.0 % error, which can also be due to solubility problem of the synthesized material. The BET surface area was measured as 14.21 m^2 g^{-1} for $FeMnO_3$ nanowires. $FeMnO_3$ nanowires were observed to have higher surface area than the one of $CuCr_2O_4$ nanoparticles. Large surface area is very important for not only catalysis but also for many other potential applications. Therefore, larger surface area of $FeMnO_3$ nanowires suggest them to be more advantageous for the desired applications compared to $CuCr_2O_4$.

5.1.3 Characterization of NiFe₂O₄-NiO Nanoparticles

$NiFe_2O_4$-NiO nanoparticles were synthesized via simple hydrothermal method where urea was used as surfactant. The urea molecules could react with Ni^{2+} and Fe^{2+} ions and form Ni-Fe-urea precursor complex, which was later calcined in air to obtain $NiFe_2O_4$-NiO nanoparticles (Figure 5.13).
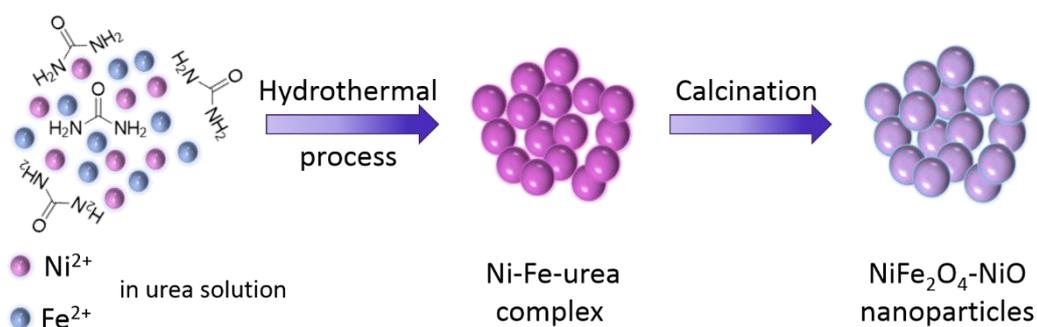
Figure 5.13. Illustration for the formation of NiFe₂O₄-NiO nanoparticles

SEM and TEM images of the materials are given in Figure 5.14. The microscopy images show that $NiFe_2O_4$-NiO nanomaterial is composed of spherical-like particles with average size of 35 nm. EDX spectrum of the particles confirms the presence of Ni and Fe in the materials' structure (Figure 5.15). The detailed analysis on the composition of the nanoparticles with elemental mapping shows that Ni, Fe and O elements are homogeneously distributed across the whole structure (Figure 5.14g).
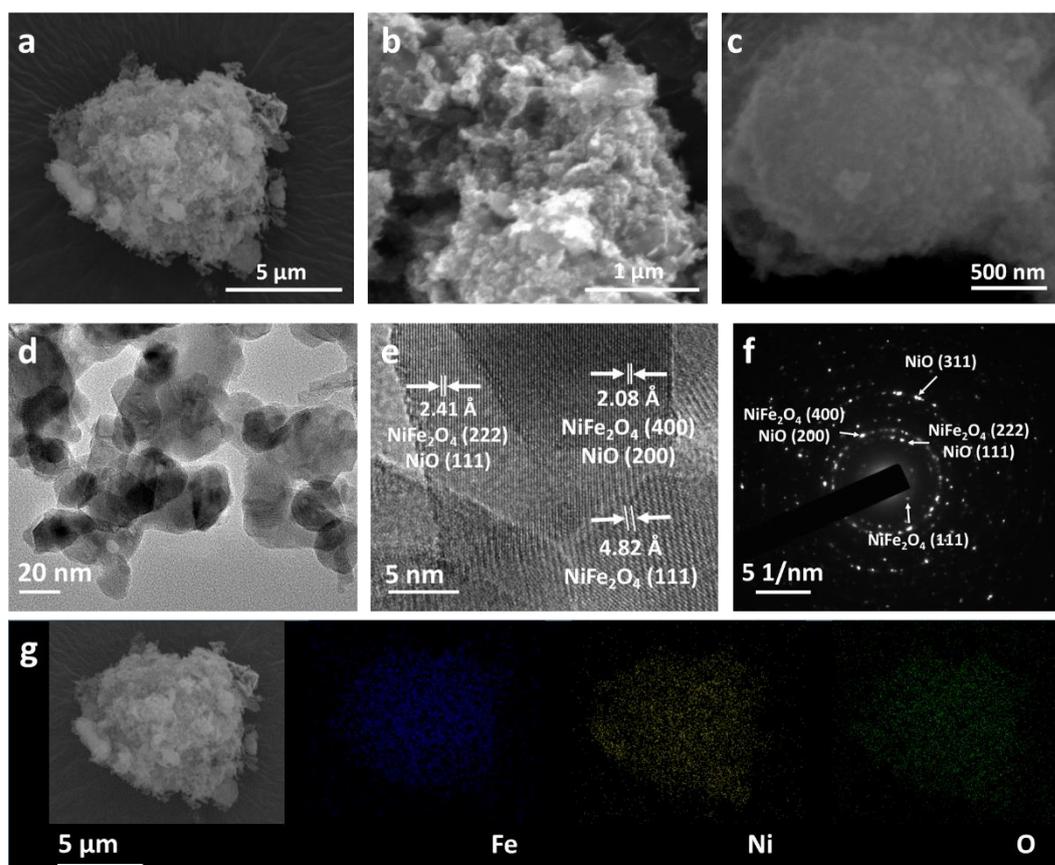
Figure 5.14. (a-c) SEM and (d-e) TEM images at different magnifications, (f) SAED pattern and (g) element mapping (Fe (blue), (Ni (yellow), O (green) of $NiFe_2O_4$-NiO nanoparticles

Element	Wt %	At %
C K	66.94	76.41
O K	25.41	21.77
FeK	2.74	0.67
NiK	4.91	1.15
Total	100.00	100.00
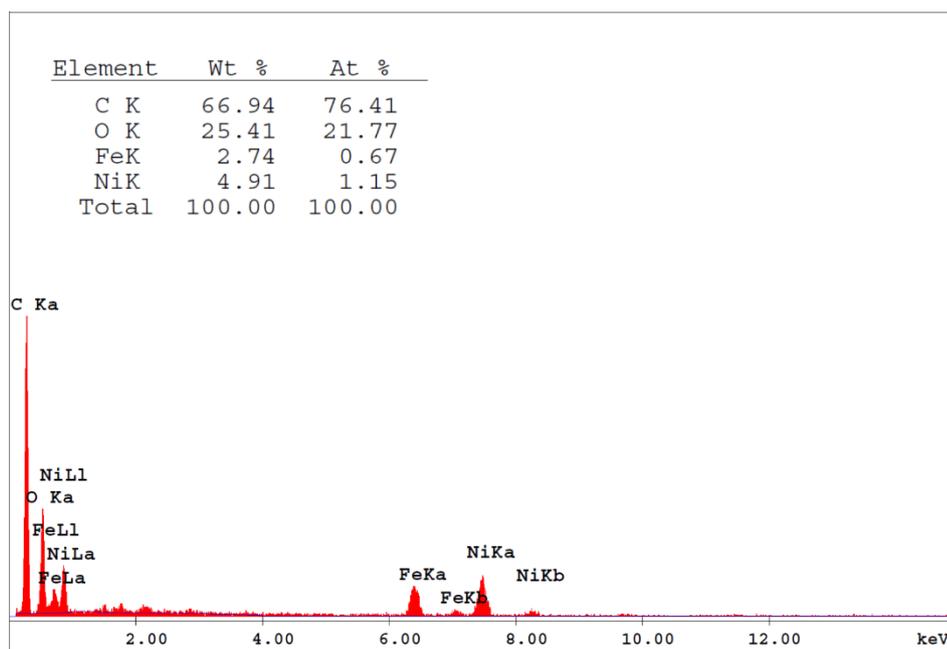
Figure 5.15. EDX spectrum of $NiFe_2O_4$-NiO nanoparticles

Figure 5.16 shows the XRD pattern of $NiFe_2O_4$-NiO nanoparticles. The peaks located at 2θ values of 18.4°, 30.4°, 35.7°, 37.3°, 43.4°, 54.0°, 57.5°, 63.1°, 71.6° and 74.7° are attributed to (111), (220), (311), (222), (400), (422), (511), (440), (620) and (533) planes of $NiFe_2O_4$ (PDF 00-003-0875), respectively. In addition, peaks corresponding to (111), (200), (220) and (311) planes of cubic NiO (PDF 01-071-1179) are observed at 2θ values of 37.3°, 43.4°, 63.1° and 75.5°, indicating the co-formation of NiO and $NiFe_2O_4$. (222), (400) and (440) diffraction peaks of $NiFe_2O_4$ coincide with (111), (200) and (220) peaks of NiO, respectively. The reason for this observation is mainly because the unit cell parameters of $NiFe_2O_4$ and NiO are very similar.[71–74] The crystallite size was calculated as ca. 15.1 nm based on the diffraction peak at 43.4°. The crystallite size is slightly smaller than particle size measured by TEM analysis.

53
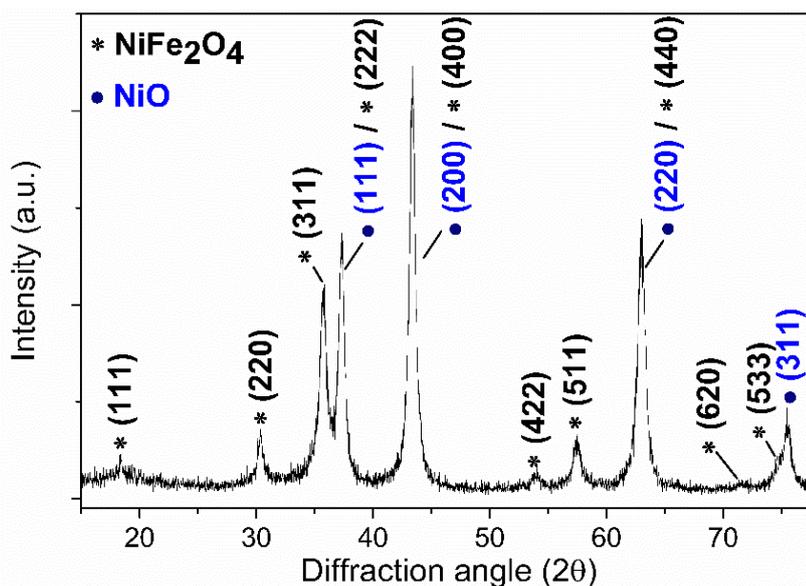
Figure 5.16. XRD pattern of NiFe$_2$O$_4$-NiO nanoparticles

XPS survey spectrum along with Ni 2p, Fe 2p and O 1s spectra of NiFe$_2$O$_4$-NiO nanomaterials are given in Figures 5.17 and 5.18. Survey spectrum affirms the presence of only Ni, Fe and O in the nanomaterial (Figure 5.17) in addition to C, which was used for calibration. Ni 2p core level spectrum is shown in Figure 5.18a. Two characteristic peaks at 855.6 eV and 873.4 eV corresponding to Ni 2p$_{3/2}$ and Ni 2p$_{1/2}$ were observed together with two shakeup satellite peaks, which suggest the presence of Ni^{2+} in the materials.[71,75] Deconvolution of these peaks resulted in two Gaussians indicative of co-existence of Ni^{2+} (855.4 eV and 873.2 eV) and Ni^{3+} (857.3 eV and 875.1 eV) ions in NiFe$_2$O$_4$-NiO.[30,76] Fe 2p core level spectrum displays two spin-orbit doublets, 2p$_{3/2}$ and 2p$_{1/2}$, at 711.6 eV and 724.6 eV, respectively (Figure 5.18b). Absence of satellite peaks confirms that Fe$_3$O$_4$ or Fe$_2$O$_3$ is not formed and NiFe$_2$O$_4$-NiO structure comprise of Fe^{3+} ions.[30,77–79] Fitting of O 1s core level spectrum revealed three oxygen contributions which are attributed to metal-oxygen bond (529.9 eV, peak I), oxygen deficient sites and oxygen species (O$_2^{2-}$, OH$^-$) adsorbed onto the nanomaterials' surface(531.1 eV, peak II and 534.2 eV, peak III) (Figure 5.18c).[80]
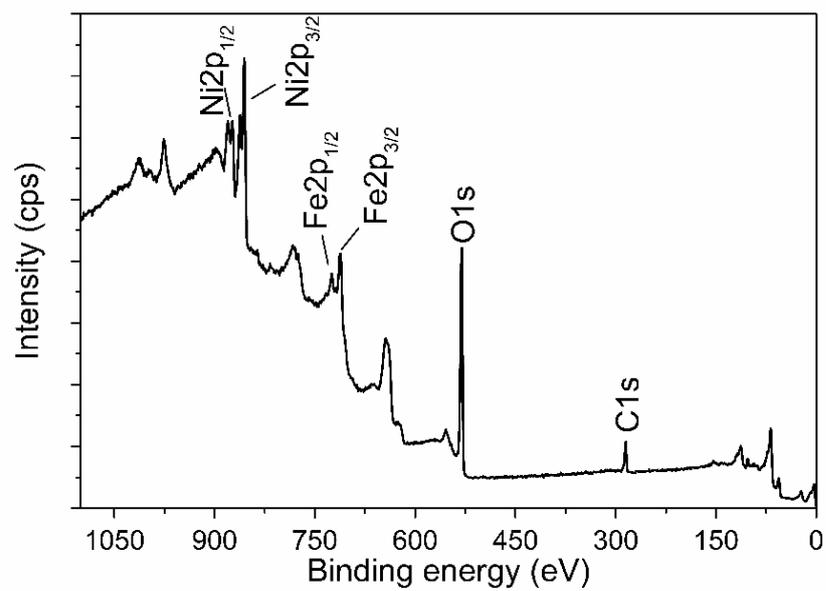
Figure 5.17. XPS survey spectrum of NiFe$_2$O$_4$-NiO nanoparticles
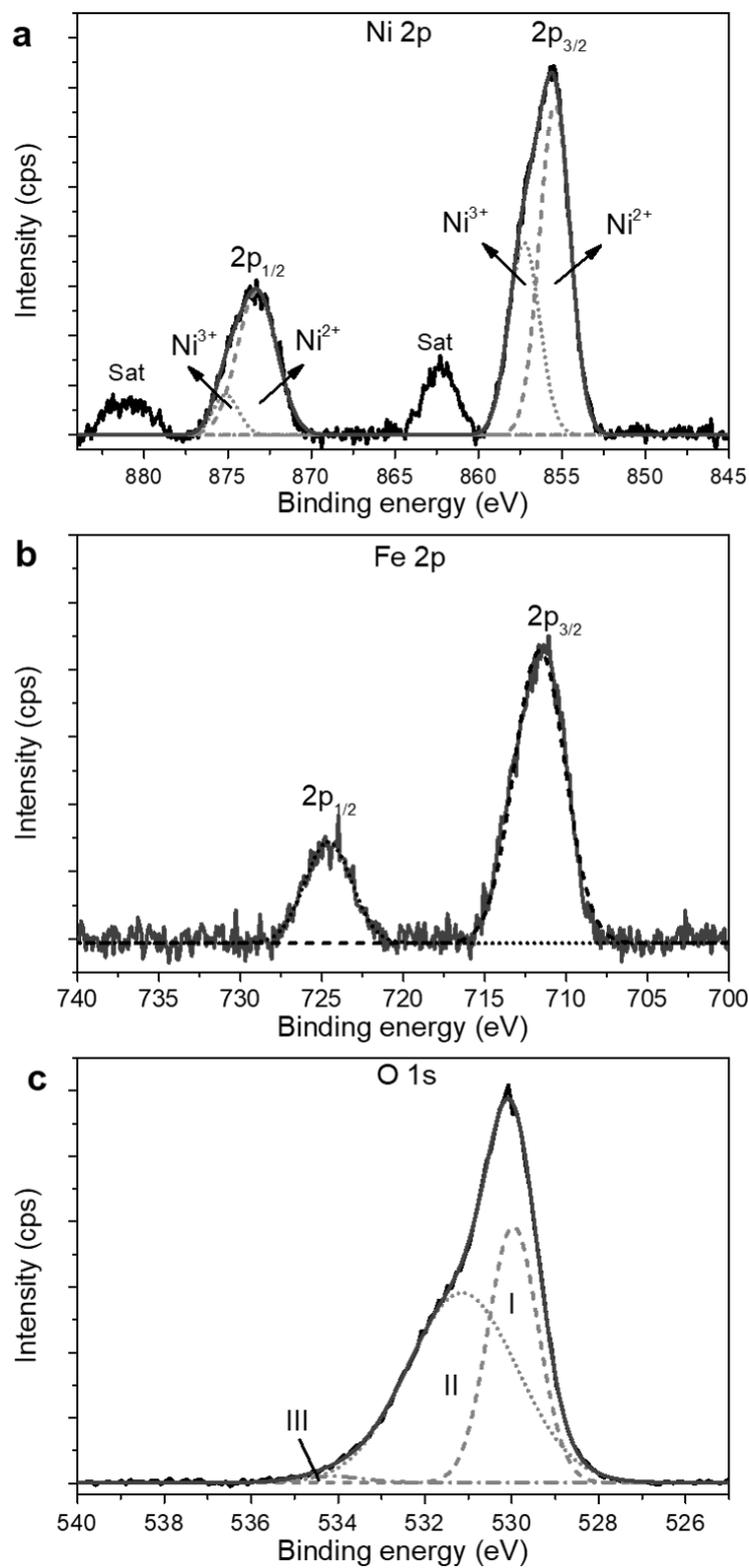
Figure 5.18. XPS (a) Ni 2p, (b) Fe2p and (c) O 1s spectra NiFe$_2$O$_4$-NiO nanoparticles

ICP-OES was utilized to investigate the elemental composition and mass percent of each element in the material, and the amount of Fe and Ni were determined to be 21 wt% and 49 wt%, respectively. The mole ratio was calculated using ICP-OES data. The calculation resulted in $NiFe_2O_4$:NiO ratio of 1:3.44 which suggest presence of higher amount of NiO in the synthesized material. BET surface area and pore size of nanomaterials were studied via N_2 adsorption-desorption analysis. The isotherm can be categorized as type IV based on the International Union of Pure and Applied Chemistry (IUPAC) classification.[81,82] $NiFe_2O_4$-NiO nanoparticles exhibit a large BET surface area of 79.04 m^2 g^{-1} along with pore size and pore volume of 4.4 nm and 0.62 cm^3 g^{-1}, respectively. Pore size data along with BET isotherm (Figure A2) show that obtained $NiFe_2O_4$-NiO nanoparticles have mesoporous nature. Large surface area and high porosity of this material are believed to have significant effect on water oxidation activity.

5.1.4   Characterization of $NiCo_2O_4$-NiO Microspheres

$NiCo_2O_4$-NiO nanomaterials were synthesized in two different morphologies via two different structure directing agents; urea and CTAC through simple hydrothermal method. Similar to that of $FeMnO_3$ nanowires and $NiFe_2O_4$-NiO nanoparticles, in $NiCo_2O_4$-NiO nanomaterials too, CTAC and urea coordinate to transition metal ions and gather to form microspheres of NiCo-surfactant precursor complexes. The formation of $NiCo_2O_4$-NiO structures take place by the following calcination step. Reaction with urea resulted in urchin-like morphology (Figure 5.19) while with use of CTAC microspheres with nanoplate assembly are formed (Figure 5.20).
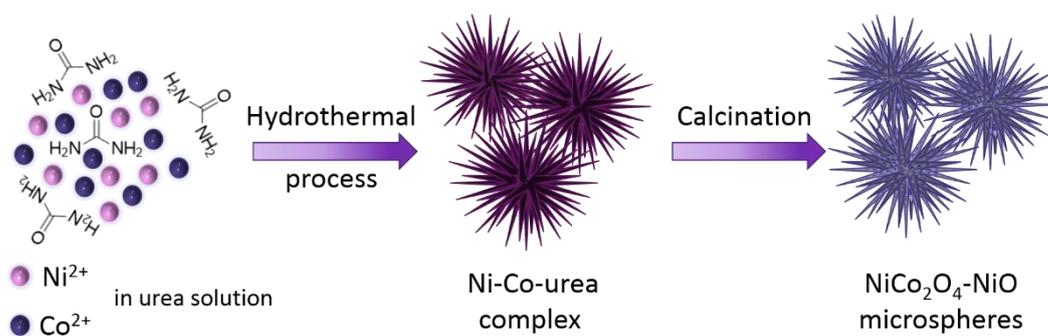
Figure 5.19. Illustration for the formation of urea stabilized NiCo$_2$O$_4$-NiO microspheres
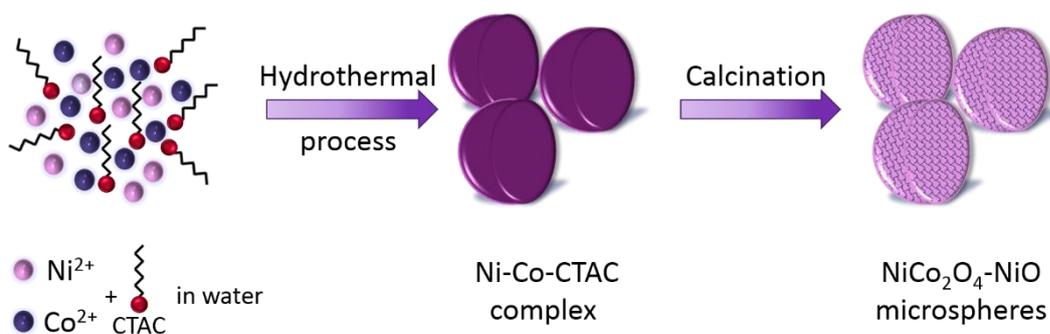
Figure 5.20. Illustration for the formation of CTAC stabilized NiCo$_2$O$_4$-NiO microspheres

Figure 5.21 displays the SEM and TEM images of hierarchical NiCo$_2$O$_4$-NiO nanomaterials synthesized by using urea (U-NiCo). The microscopy images exhibit that urchin-like microspheres are formed by the assembly of NWs grown out from the center of the spheres. The NWs have approximately 650 nm ± 50 nm of length and 75 nm ± 10 nm of thickness. Further inspection of the images reveals that Nanoparticles with average size of 25 nm ± 5nm are assembled to form the observed NWs. EDX analysis which was performed in conjunction with SEM analysis confirm the existence of Co and Ni in the synthesized hierarchical nanomaterial (Figure 5.22).

A detailed analysis on the elemental composition of the material was studied by elemental mapping of Ni, Co and O on the urchin-like microspheres. The mapping shows the uniform distribution of the elements forming the nanomaterial (Figure 5.21g).
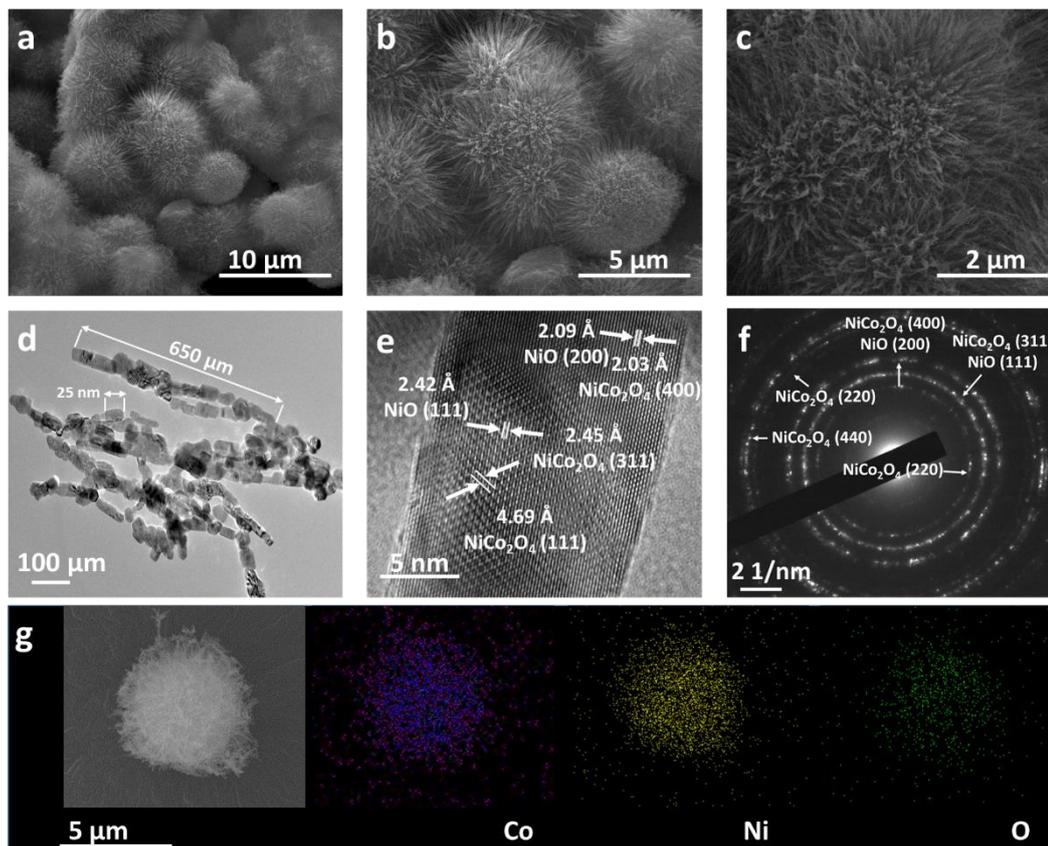
Figure 5.21. (a-c) SEM and (d-e) TEM images at different magnification, (f) SAED pattern and (g) Element mapping (Co (blue), Ni (yellow), O (green)) of U-NiCo microspheres
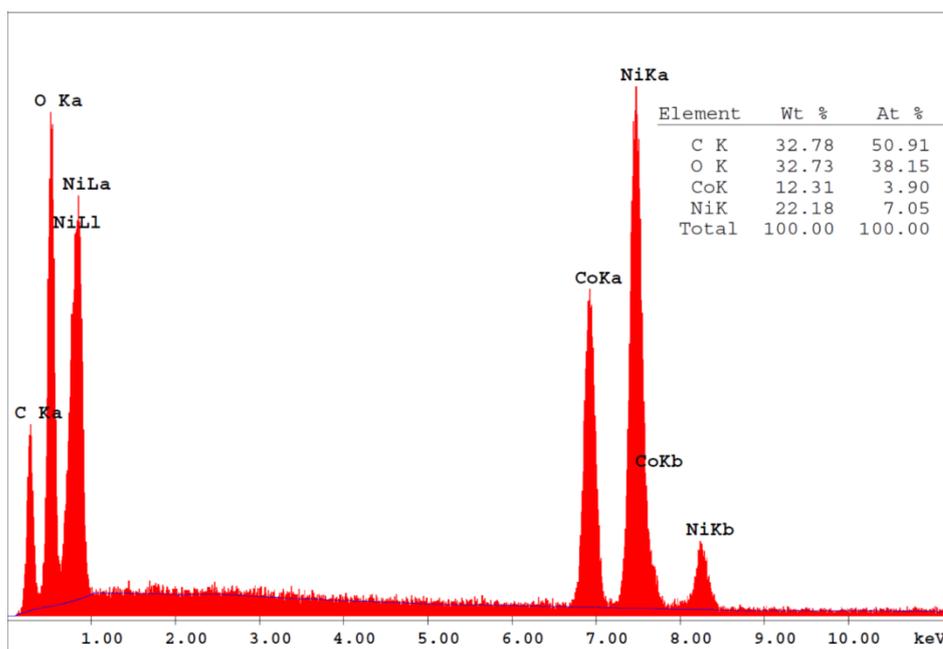
Figure 5.22. EDX spectrum of U-NiCo microspheres

SEM and TEM images of $NiCo_2O_4$-NiO nanomaterials synthesized by using CTAC (C-NiCo) are demonstrated in Figure 5.23. Unlike U-NiCo, numerous nanoplates of C-NiCo are assembled to form a spherical structure. TEM images shown in Figure 5.23d,e reveal that nanoplates are assemblies of nanoparticles with average of 85 nm ± 10 nm. EDX analysis was also utilized to prove the presence of Co and Ni in the structure (Figure 5.24). Similar to U-NiCo, elemental mapping of C-NiCo hierarchical microspheres shows that Ni, Co and O are distributed homogeneously across the whole structure.
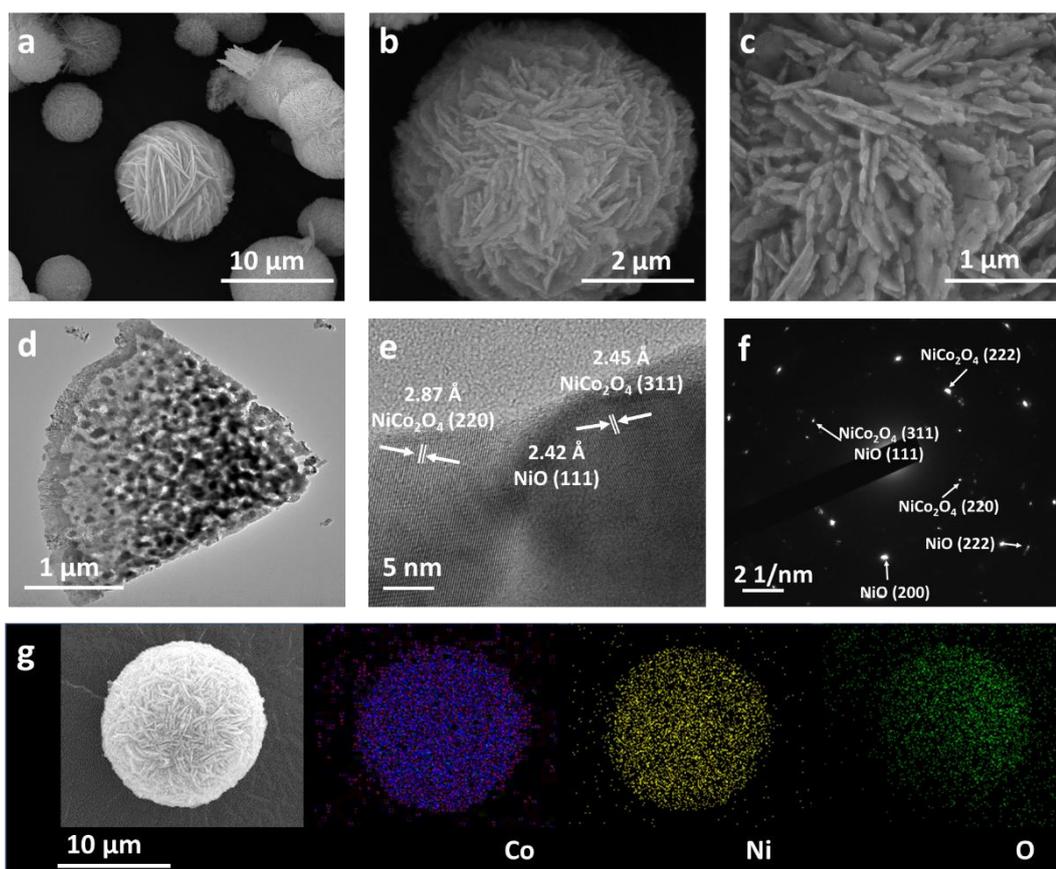
Figure 5.23. (a-c) SEM and (d-e) TEM images at different magnifications, (f) SAED pattern and (g) Element mapping (Co (blue), Ni (yellow), O (green)) of C-NiCo microspheres
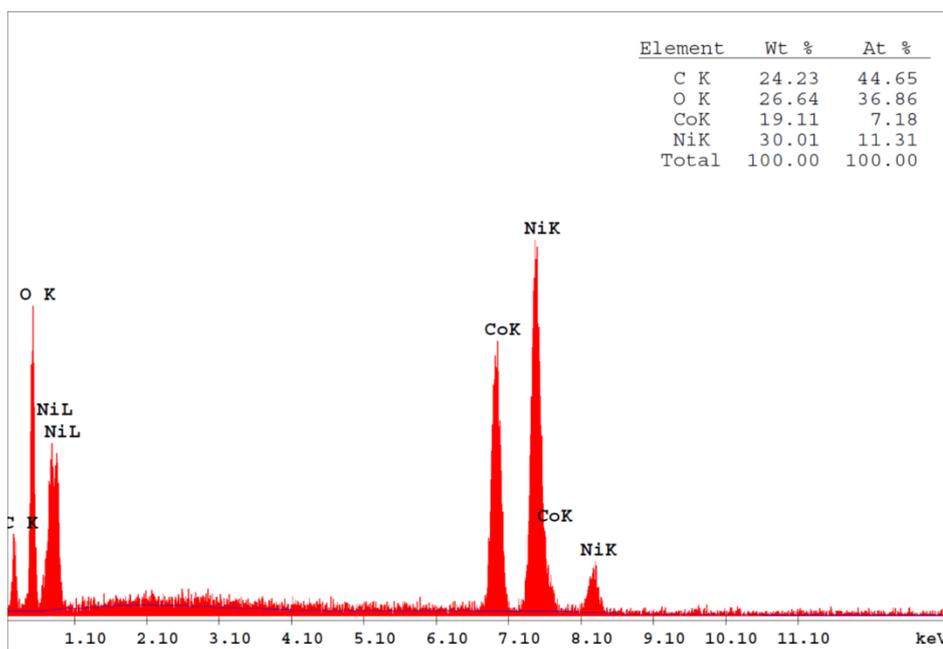
Figure 5.24. EDX spectrum of C-NiCo microspheres

XRD patterns of $NiCo_2O_4$-NiO microspheres are given in Figure 5.25. The patterns of both materials demonstrate peaks at 2θ values of 18.9°, 31.1°, 36.7°, 38.4°, 44.6°, 55.4°, 59.2°, 65.2° and 77.1° which were indexed to (111), (220), (311), (222), (400), (422), (511), (440) and (533) planes of $NiCo_2O_4$, respectively (PDF 01-073-1702). In addition, diffraction peaks located at 2θ values of 37.2°, 43.2°, 62.7°, 75.3° and 79.2° were assigned to (111), (200), (220), (311) and (222) planes of cubic NiO (PDF 01-071-1179), suggesting the formation of NiO along with spinel $NiCo_2O_4$. XRD peak analysis[38] was performed to estimate crystallite sizes which were calculated as ca. 17.8 nm and 28.9 nm for U-NiCo and C-NiCo, respectively. The diffraction peak at 43.2° (200) was used in the analysis. The crystallite sizes are slightly smaller than the sizes of particles measured by TEM analysis.
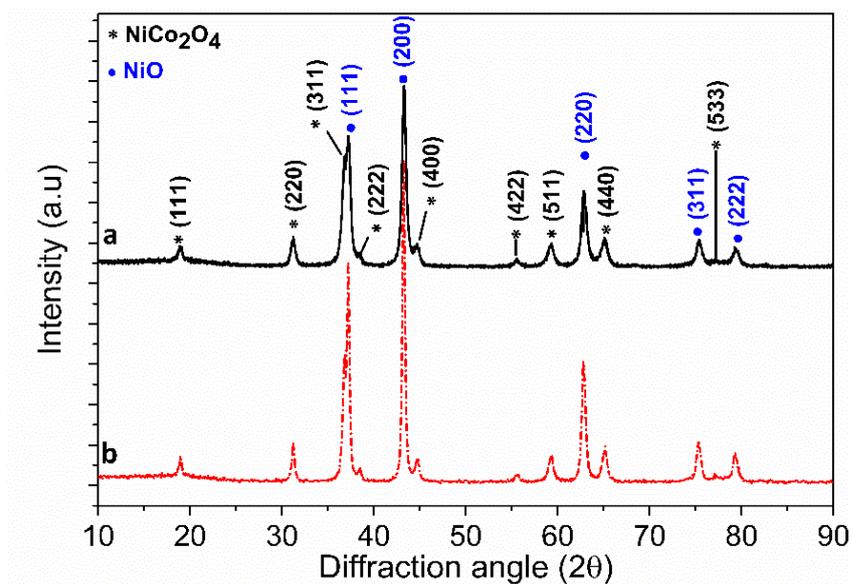
Figure 5.25. XRD patterns of (a) U-NiCo and (b) C-NiCo microspheres

Figures 5.26, 5.27 and 5.28 show the XPS spectra of $NiCo_2O_4$-NiO microspheres. The survey spectra of both U- and C-NiCo reveal the presence of Co, Ni, O and C, which was used for calibration (Figure 5.26).
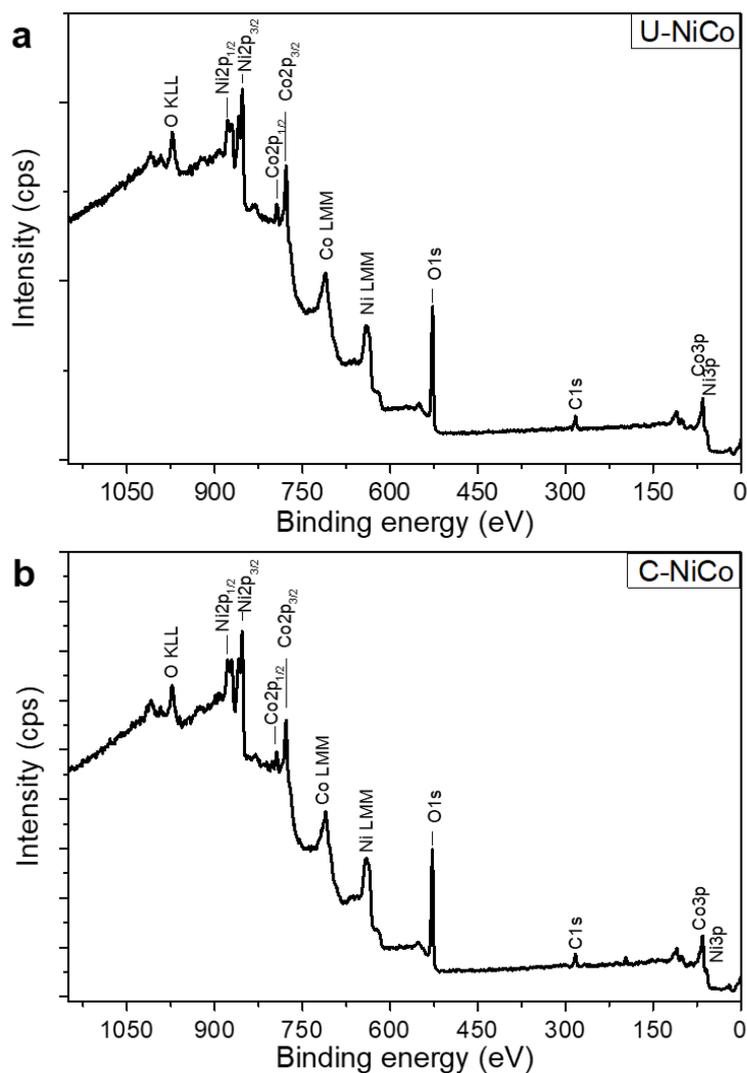
Figure 5.26. XPS Survey spectra of (a) U-NiCo and (b) C-NiCo microspheres

The Co 2p core-level spectra of U- and C-NiCo microspheres are given in Figure 5.27a and 5.28a. The peaks were fitted to two spin-orbit doublets at 777.9 eV and 793.0 eV corresponding to $2p_{3/2}$ and $2p_{1/2}$, respectively. Two bands under each Co 2p peak were observed by Gaussian fitting process. The peaks were assigned to Co^{2+} (777.4 eV and 792.5 eV) and Co^{3+} (778.7 eV and 794.1 eV) which agree well with the values reported in previous studies.[23,29,56,83–86] The Ni 2p core-level spectrum exhibits two spin-orbit doublets at 852.1 eV and 870.1eV with two shakeup satellite

peaks (Figure 5.27b and 5.28b). The fitted peaks at 851.9 eV and 869.6 eV were ascribed to Ni^{2+} while the ones at 853.8 eV and 871.5 eV were assigned to Ni^{3+}.[56,84–86] The spectrum of O 1s shows two oxygen contributions which were ascribed to metal-oxygen bond (peak I at 527.5 eV) and oxygen species (i.e O_2^{2-}, OH^-) adsorbed onto the catalyst surface (peak II at 528.8 eV) suggesting the existence of low oxygen coordination sites in the materials (Figure 5.27c and 5.28c).[23,29]
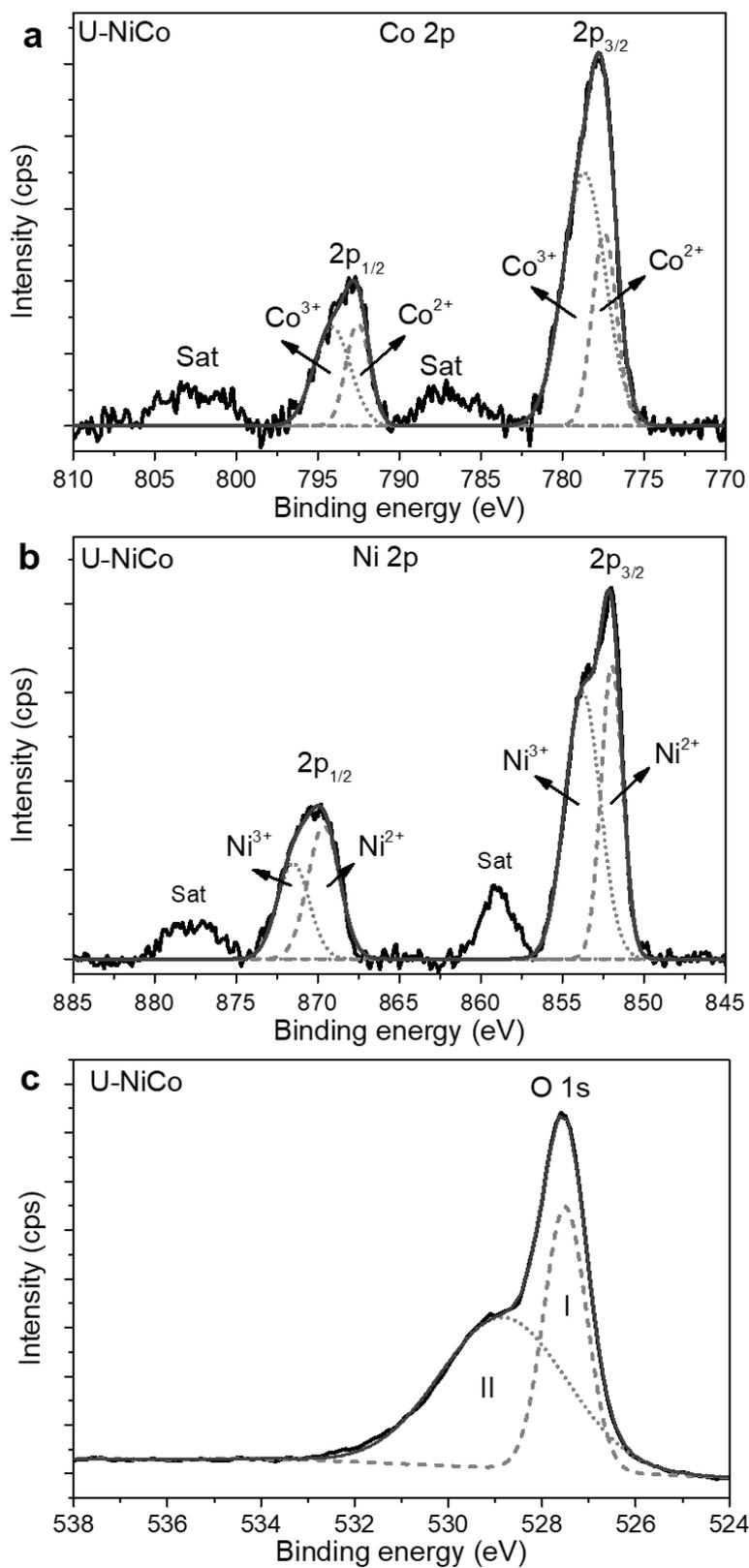
Figure 5.27. XPS (a) Co 2p, (b) Ni 2p and (c) O 1s spectra of U-NiCo microspheres
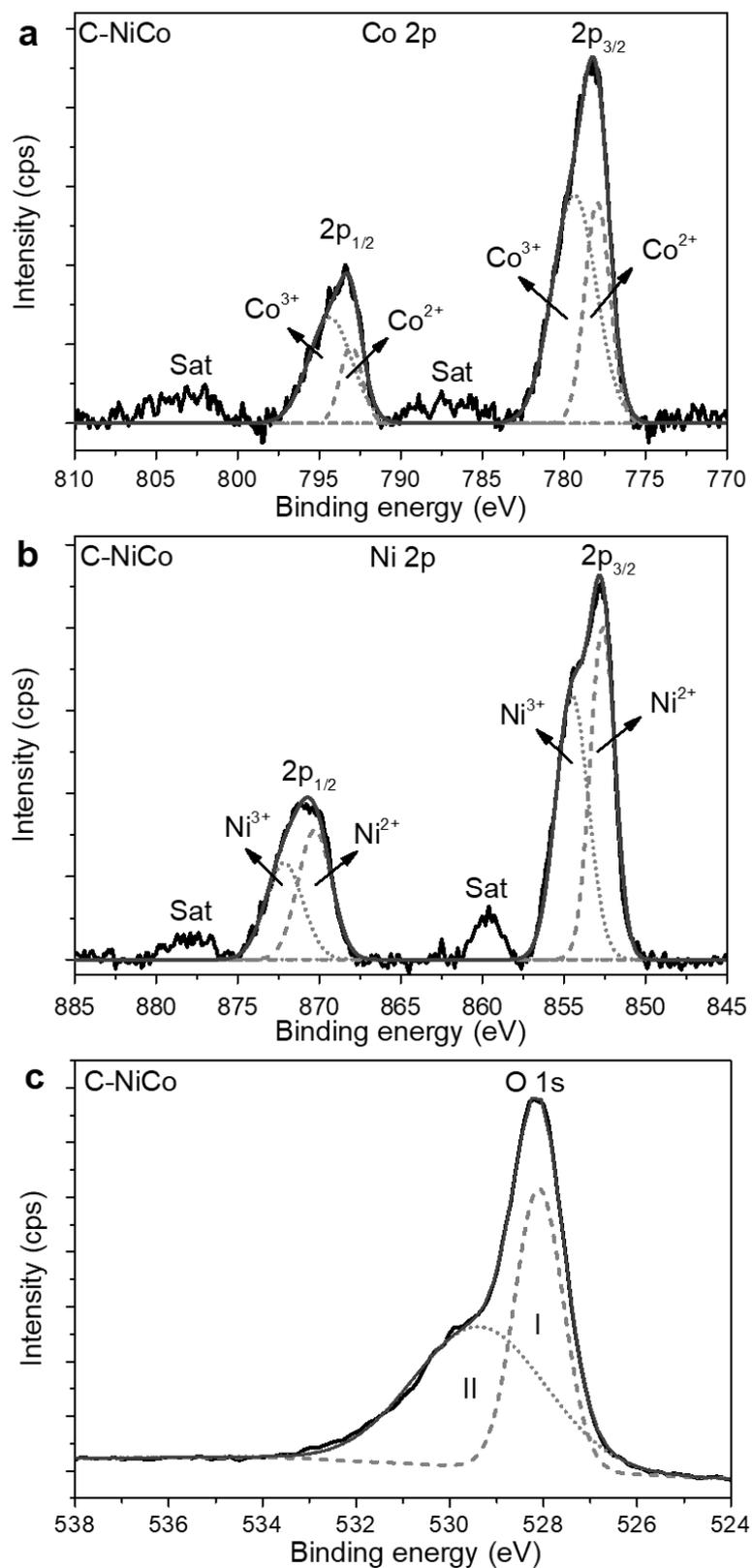
Figure 5.28. XPS (a) Co 2p, (b) Ni 2p and (c) O 1s spectra of C-NiCo microspheres

Elemental composition and mass percent of each element in the microspheres were investigated by ICP-OES. The amount of Co was found to be 28 wt% and 27 wt% in U-NiCo and C-NiCo, respectively. The amount of Ni in U-NiCo was determined as 53 wt%, whereas it was found as 57 wt% in C-NiCo. $NiCo_2O_4$:NiO mole ratio were calculated using ICP-OES data, and found to be 1:2.8 and 1:3.2 for U-NiCo and C-NiCo, respectively. N_2 adsorption-desorption analyses were performed to examine the BET surface areas and pore size of the synthesized nanomaterials. BET surface areas were determined as 41.3 m^2 g^{-1} and 13.4 m^2 g^{-1} for U-NiCo and C-NiCo, respectively. BET isotherms (Figure A.3) suggest the mesoporous nature of $NiCo_2O_4$-NiO microspheres with average pore sizes of 2.5 nm and 3.0 nm for U-NiCo and C-NiCo, respectively. Moreover, pore volume of U-NiCo was determined as 0.45 cm^3 g^{-1} while for C-NiCo it was 0.20 cm^3 g^{-1}. Larger pore volume with smaller pore size suggest that U-NiCo nanomaterials possess higher number of pores than that of C-NiCo.

5.2 Electrocatalytic Activities of of Transition Metal Oxide Nanomaterials for Water Oxidation Reaction

5.2.1 Electrocatalytic activity of $CuCr_2O_4$ nanoparticles

Being the first material investigated in this study, important parameters (i.e. preparation of the electrode, catalyst loading, and type of electrolyte) for electrocatalytic water oxidation reaction was determined with $CuCr_2O_4$ nanoparticles. Effect of carbon materials (Printex L6 (PL6), Super C65 (SC65), multiwalled carbon nanotube (MWCNT)) addition into catalyst solution as well as effect of carbon and Nafion® amount on onset potential and current density were studied (see Appendix). However, no significant difference was noted with the addition of carbon materials. During the preliminary measurements, optimum amount of Nafion® was determined as 19.0 μL. Hence, same amount of Nafion® was used throughout the study of electrochemical activities of other nanomaterials.

Electrochemical measurements were performed in two different electrolyte solution, namely 0.1 M sodium borate (pH:9.2) and 0.1 M KOH solution. Maximum current density value the catalyst could generate was 1.68 mA cm^{-2} at an overpotential of 830 mV with the use of sodium borate solution (Figure B.1 and Table B.1). Therefore, 0.1 M KOH solution was used in the investigation of electrochemical activities of nanomaterials for water oxidation reaction.

Figure 5.29a shows the polarization curve of $CuCr_2O_4$ nanoparticles along with that of bare GCE. $CuCr_2O_4$ nanoparticles exhibited an onset potential of 2.07 V (vs RHE) with an overpotential of 1.05 V to drive current density of 10 mA cm^{-2} (η_{10}). Both onset potential and η_{10} are very high indicating that $CuCr_2O_4$ nanoparticles are not very active in water oxidation reaction. Water oxidation kinetics of the nanoparticles were examined by fitting polarization curves to Tafel equation. Tafel slope was determined as 67 mV dec^{-1} (Figure 5.29b).
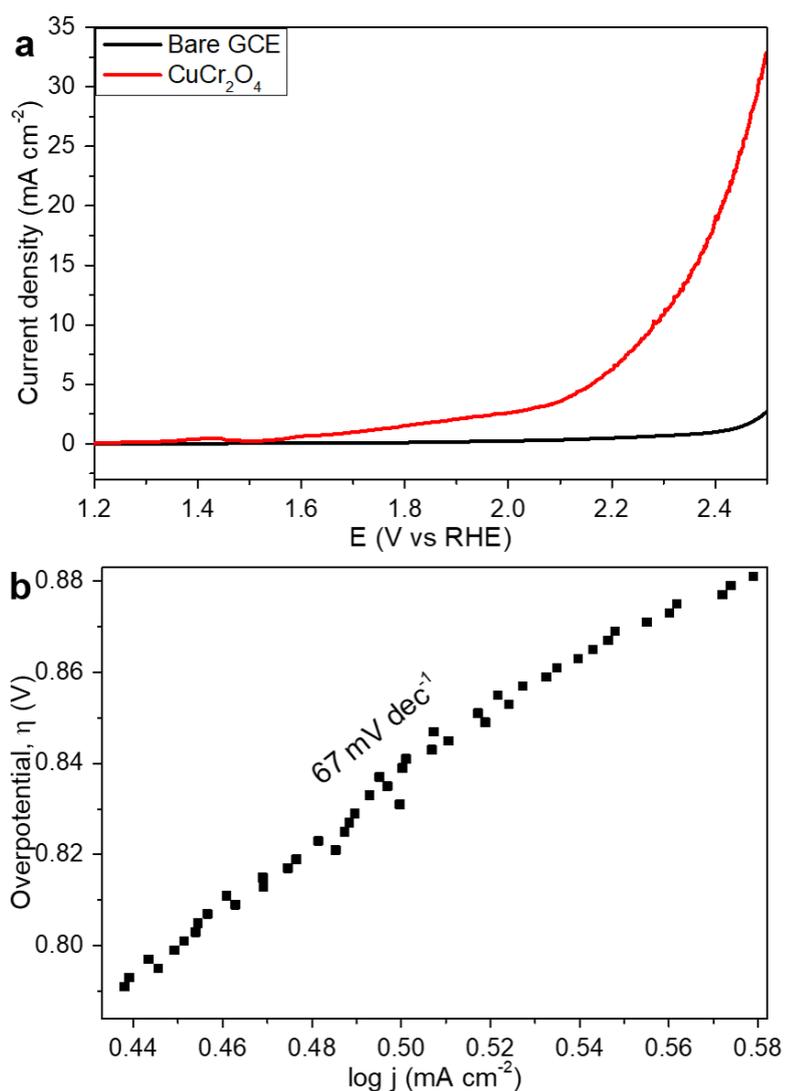
Figure 5.29. (a) Polarization curves of bare GCE and CuCr$_2$O$_4$ nanoparticles in 0.1 M KOH at a scan rate of 5 mV s^{-1} and (b) The corresponding Tafel plot obtained from polarization curve

EIS was utilized to further investigate the kinetic properties of the prepared catalyst. Semicircles demonstrated in Figure 5.30 are associated with the charge transfer resistance (R$_{ct}$) at high frequencies. The diameter of the semicircle decreases with increasing overpotential, which indicates enhanced electrical conductivity as well as

faster charge transfer during oxygen evolution. R_{ct} of the electrode at onset potential was calculated as 76 Ω by fitting to constant phase element (CPE) model.
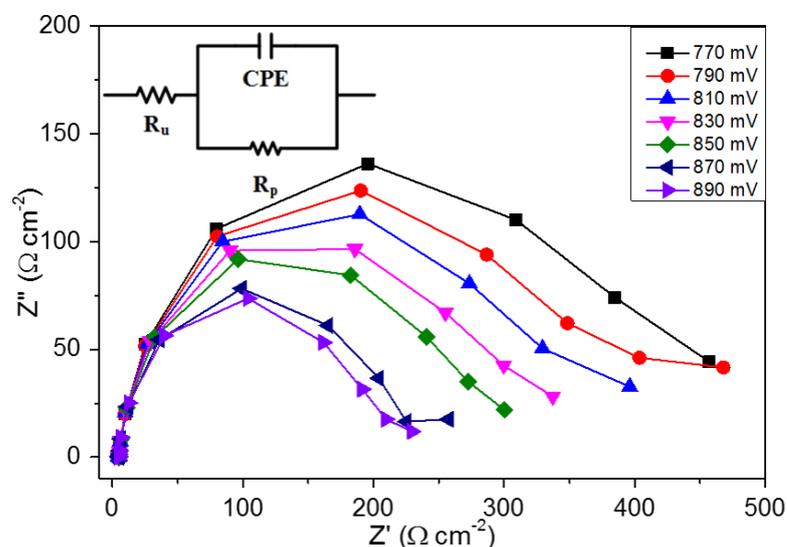
Figure 5.30. Nyquist plots of CuCr$_2$O$_4$ nanoparticles at various overpotential values in 0.1 M KOH

The durability of the nanoparticles was studied using chronopotentiometry (j=10 mA cm^{-2}) for 3 h (Figure 5.31) and chronoamperometry (η=1.10 V) for another 3 h (Figure 5.32). Figure 5.31a shows the polarization curves obtained before and after chronopotentiometry, while potential of time-dependent curve is given in Figure 5.31b. There is a slight decrease in the potential during the course of electrolysis. In addition, slight increase in both onset potential and overpotential (η=1.12 V) at j=10 mA cm^{-2} were observed after electrolysis.
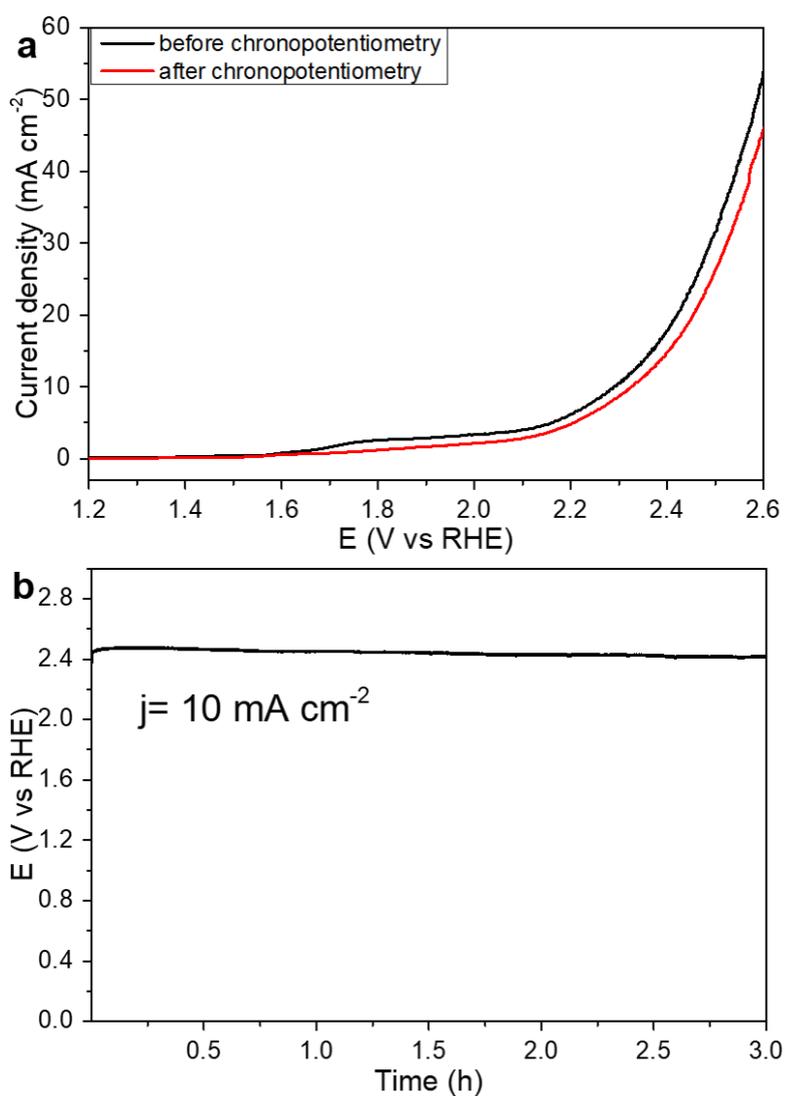
Figure 5.31. (a) Polarization curves before and after chronopotentiometric electrolysis at j=10 mA cm^{-2} and (b) the change in potential during chronopotentiometry in 0.1 M KOH

As shown in Figure 5.32b, the current density of 10 mA cm^{-2} was maintained for another 3 h. Even though CuCr$_2$O$_4$ nanoparticles do not exhibit very high electrocatalytic activity, both of the stability tests indicate good stability for water oxidation reaction when the required conditions are set.
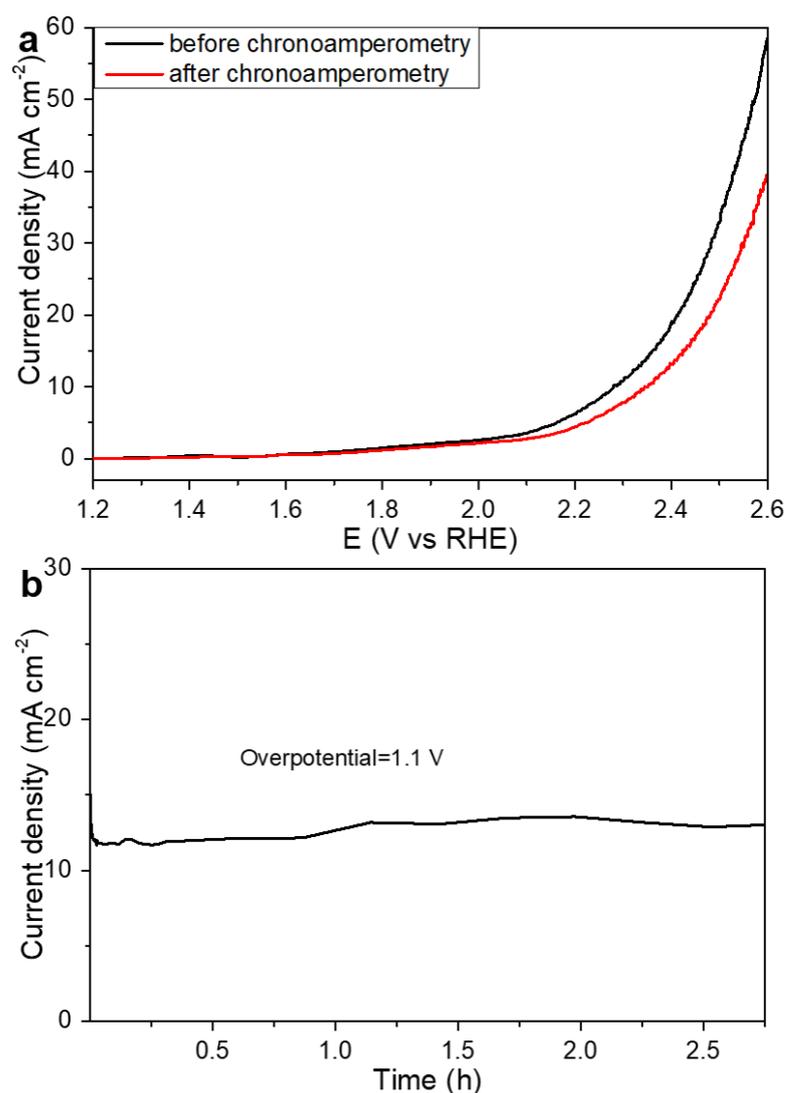
Figure 5.32. (a) Polarization curves before and after chronoamperometric electrolysis at η=1.1 V and (b) the change current density during chronoamperometry

5.2.2   Electrocatalytic activity of FeMnO₃ nanowires

The electrocatalytic activities of FTO substrates modified with FeMnO$_3$ nanowires were investigated towards water oxidation in alkaline medium (0.1 M KOH). FeMnO$_3$ modified FTO (FeMnO$_3$-FTO) was used as working electrode, and

evaluation of its performance was performed by studying polarization curves. For comparison, bare FTO electrode and RuO_2 were also tested under the same conditions and resulting voltammograms are depicted in Figure 5.33a. Inspection of the data reveals that $FeMnO_3$-FTO demonstrates relatively high electrocatalytic activity for OER with an onset potential of 1.60 V vs RHE. Bare FTO, on the other hand, was found to exhibit almost no activity in the same medium. Although the onset potential of $FeMnO_3$-FTO electrode was found to be higher than that of RuO_2 (1.45 V vs RHE), it is comparable to those of previously reported perovskite oxides especially $CaMnO_3$ (1.60 V vs RHE)[15], $LaFeO_{3-\delta}$ (1.63 V vs RHE)[87], $La0.8Sr_{0.2}MnO_3$ (1.57 V vs RHE)[18] and S-doped $CaMnO_3$ (1.60 V vs RHE)[16].
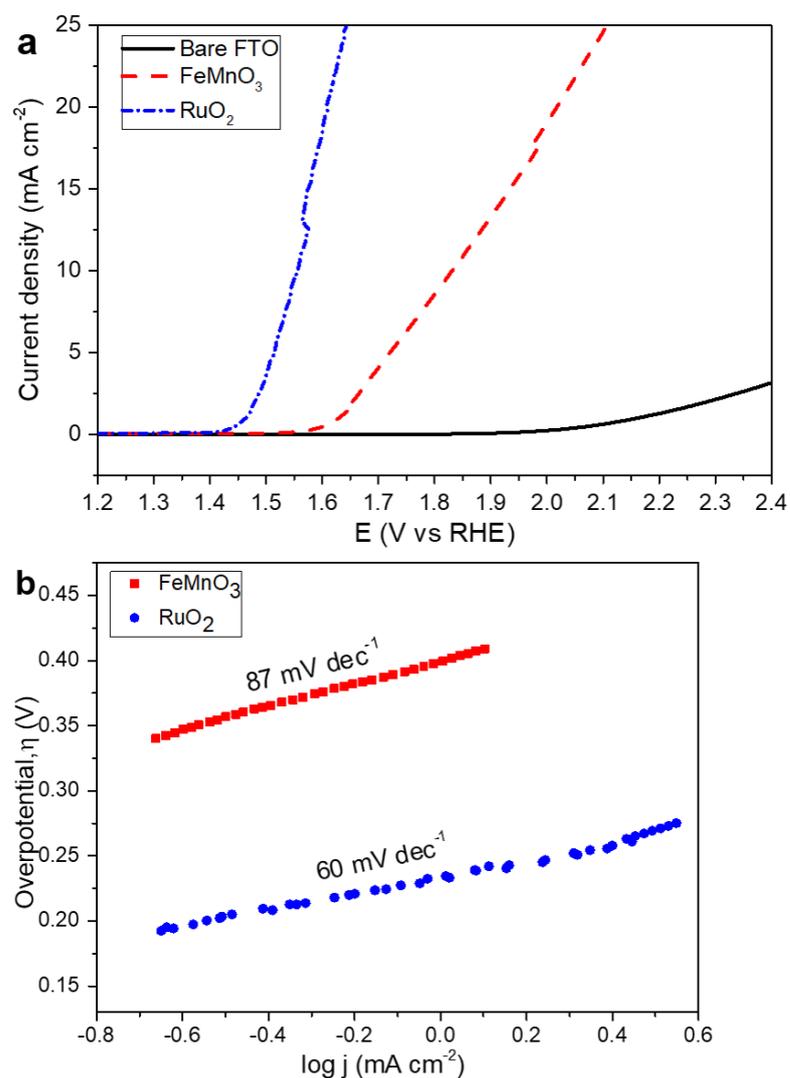
Figure 5.33. (a) Polarization curves bare GCE, FeMnO$_3$ nanowires and RuO$_2$ in 0.1 M KOH at a scan rate of 5 mV s^{-1} and (b) The corresponding Tafel plots obtained from polarization curves

The water oxidation activity of FeMnO$_3$ nanowires was also tested by using the overpotentials required to drive anodic current densities of 5 mA cm^{-2} (η_5) and 10 mA cm^{-2} (η_{10}). For FeMnO$_3$-FTO, the η_5 and η_{10} were measured as 490 mV and 600 mV, respectively. The results obtained from FeMnO$_3$-FTO are summarized in Table 3.1, as well as the ones of some reported catalysts, for comparison.

The water oxidation kinetics of $FeMnO_3$ nanowires were evaluated by fitting Tafel plot from polarization curves (Figure 5.33b). Tafel slope was estimated by employing the Tafel equation and was determined as 87 mV dec^{-1} for $FeMnO_3$-FTO. The slope was found to be much smaller than the ones of recently reported OER electrocatalysts such as $La_{0.45}Sr_{0.45}Mn_{0.9}Fe_{0.1}O_{3-\delta}$ (139 mV dec^{-1})[19], $CaMnO_3$ (197 mV dec^{-1}) and $Ca_2Mn_2O_5$ (149 mV dec^{-1})[15] indicating faster OER kinetics on $FeMnO_3$-FTO. Tafel slope of RuO_2 was found to be 60 mV dec^{-1}, and agree well with the ones reported in the literature (i.e. 69 mV dec^{-1} [5], 70 mV dec^{-1} [4], 90 mV dec^{-1} [2]).

Table 5.1 Summary of the data of some recently reported representative water oxidation electrocatalysts and $FeMnO_3$ nanowires in alkaline medium

	Onset (RHE)	η (@10 mA cm^{-2})	Tafel slope (mV dec^{-1})	Medium	REF
$FeMnO_3$	1.60	600	87	0.1 M KOH	This work [11]
$CaMnO_3$	1.6	-	197	0.1 M KOH	[15]
$Ca_2Mn_2O_5$	1.5	-	149	0.1 M KOH	[15]
$LaFeO_{3-\delta}$	1.63	465	50	1.0 M KOH	[87]
$La_{0.8}Sr_{0.2}MnO_3$*	1.57	985	-	0.1 M KOH	[18]
S-doped $CaMnO_3$	1.6	550	-	0.1 M KOH	[16]
$La_{0.45}Sr_{0.45}Mn_{0.9}Fe_{0.1}O_{3-\delta}$	-	340	139	0.1 M KOH	[19]
$BaMnO_3$	-	740 (η3)	-	0.1 M KOH	[20]
$BaMnO_3$@C	-	740 (η14)	-	0.1 M KOH	[20]
$CaMnO_{2.77}$	1.4	570 (η4)	-	1.0 M KOH	[17]
RuO_2	1.45	326	60	0.1 M KOH	This work

ECSA and RF values, which are directly proportional to the number of surface active sites were also determined to better analyze the electrocatalytic activity of the $FeMnO_3$ nanowires. CVs recorded at non-Faradaic potential range with various scan rates are given in Figure 5.34 along with the plot of double-layer charging current

(at 1.27 V vs RHE) versus scan rate. The slope of the plot, which gives the C_{dl} value of $FeMnO_3$ nanowires has been found as 1.78 mF. The ECSA and RF values were calculated as 29.6 cm^2 and 59.2, respectively. The high values of ECSA and RF is consistent with the large surface area of the nanowires. Moreover, mass activity and specific activity of $FeMnO_3$ nanowires were calculated at an overpotential of 600 mV and determined to be as 10.8 A g^{-1} and 0.17 A cm^{-2}_{ECSA}, respectively.
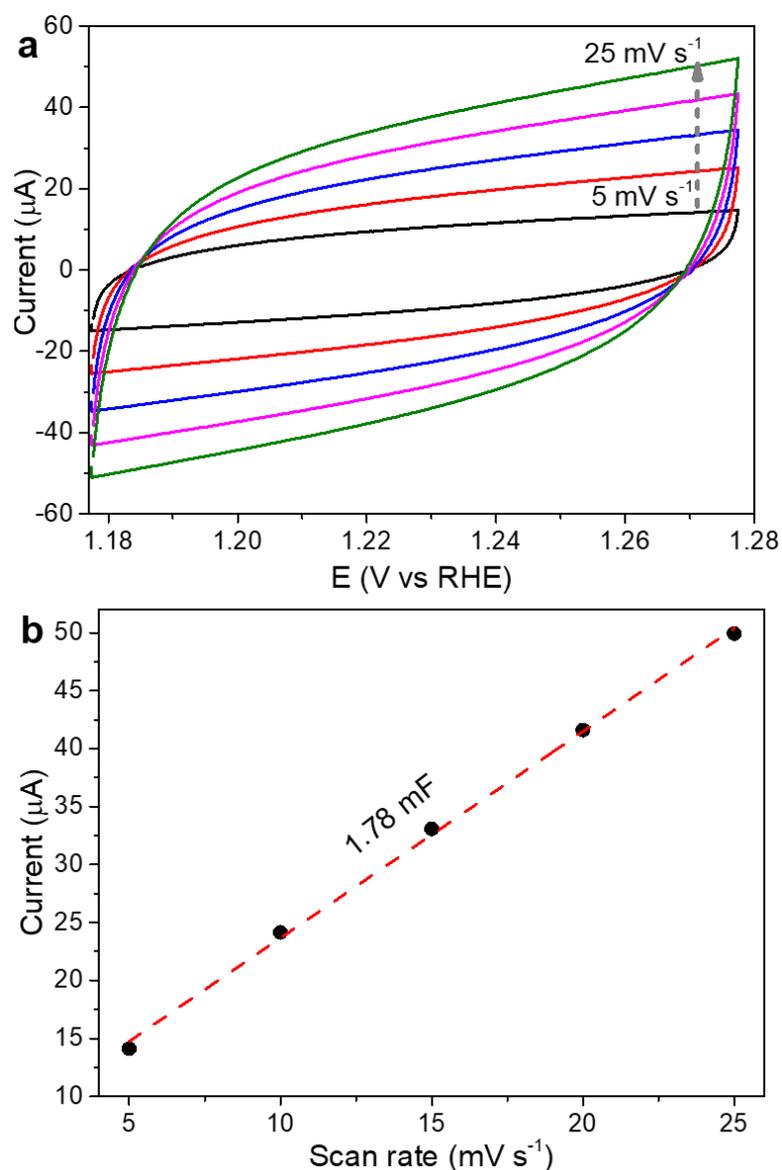
Figure 5.34. (a) CVs of $FeMnO_3$ nanowires measured at different scan rates from 5 to 25 mV s^{-1} and (b) Plot of current at 1.27 V (vs RHE) vs scan rate

77

EIS was also performed at different overpotentials to further investigate the kinetic properties of the prepared catalyst in water oxidation reaction. The Nyquist plots of $FeMnO_3$-FTO consist of semicircles, which fit to CPE model (see inset of Figure 5.35), where R_u and R_p correspond to solution resistance and charge transfer resistance (R_{ct}), respectively. The semicircles are associated with R_{ct} at high frequency region. The diameter of the semicircle decreases as the overpotential increases, which indicates enhanced electrical conductivity as well as faster charge transfer during water oxidation process.
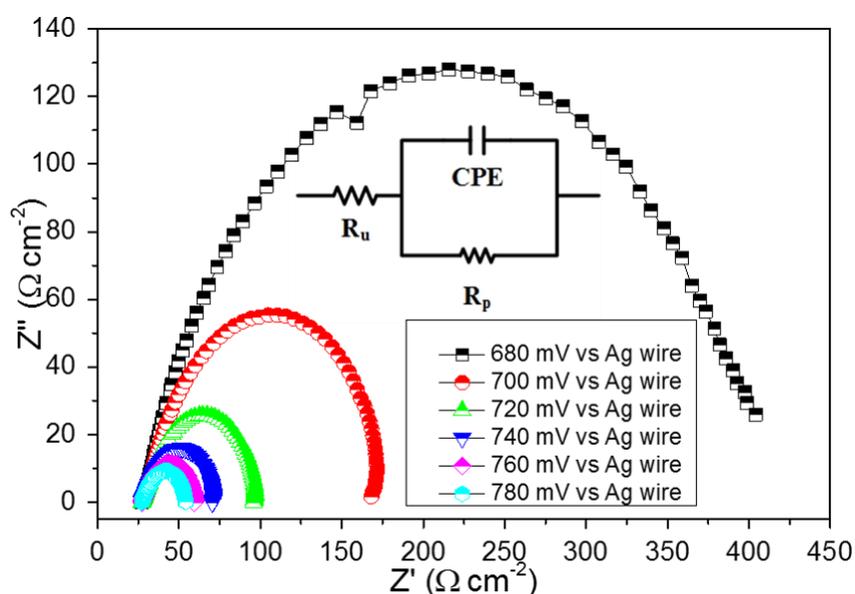
Figure 5.35. Nyquist plots for the $FeMnO_3$-FTO electrodes at different overpotentials

The durability of the modified FTO electrode was also tested in order to evaluate the water oxidation performance of the electrocatalyst for practical applications. Constant potential electrolysis was employed at overpotential of 650 mV for 10800 s in 0.1 M KOH. The polarization curves recorded before and after constant potential electrolysis are shown in Figure 5.36a. A slight shift to the higher potential

values in both onset potential (from 1.60 V to 1.70 V) and overpotential for 10 mA cm^{-2} (from 600 mV to 718 mV) was observed after 10800 s constant potential electrolysis.
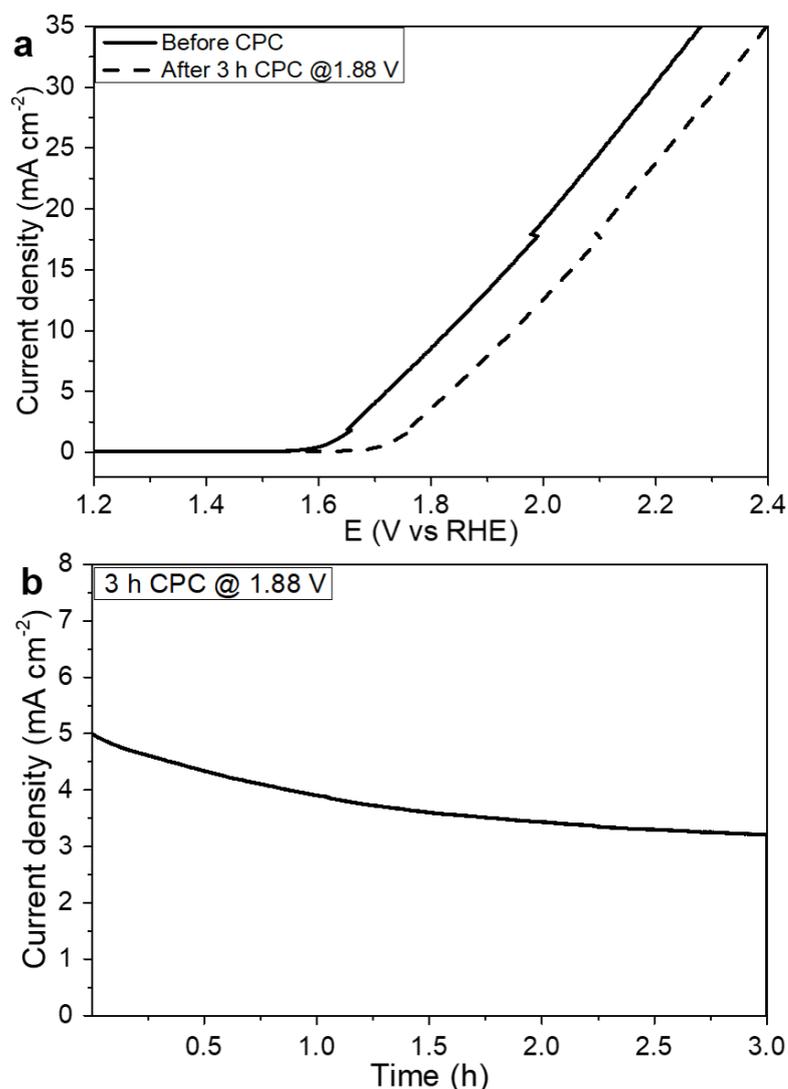
Figure 5.36. (a) Polarization curve of FeMnO$_3$-FTO electrode before and after controlled potential electrolysis at overpotential curresponding to initial current density of 5 mA cm^{-2} and (b) Change in current density during electrolysis in 0.1 M KOH

The water oxidation activity of $FeMnO_3$ nanowires was also evaluated by measuring the volume of O_2 gas produced during the electrolysis of water. The measurement was performed using the modified FTO electrode, $FeMnO_3$-FTO, as the anode in a Hoffman electrolysis set-up. The volume of O_2 released was monitored for 3600 s at a constant current of 5 mA at room temperature (Figure 5.37). The Faradaic yield of $FeMnO_3$-FTO for O_2 production was measured as >95% after the transfer of 18 C of charge. The amount of O_2 obtained is very close to the theoretical yield suggesting $FeMnO_3$ nanowires are promising candidates for OER electrocatalyst.
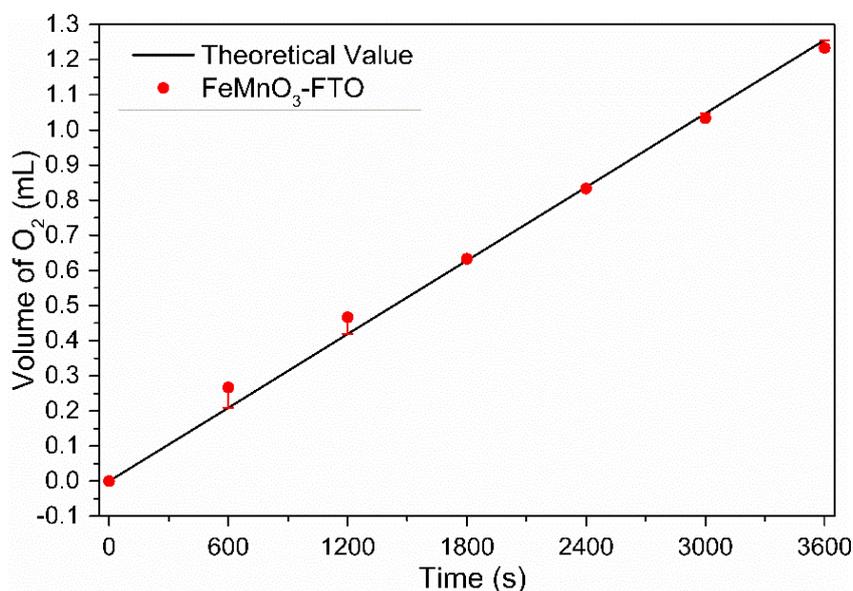
Figure 5.37. Plot of O_2 volume vs time during the electrolysis of water using $FeMnO_3$-FTO electrode

5.2.3   Electrocatalytic activity of $NiFe_2O_4$-NiO nanoparticles

The electrocatalytic activity of $NiFe_2O_4$-NiO nanoparticles for water oxidation was investigated by LSV in alkaline medium, at room temperature. Polarization curve of GCE decorated with $NiFe_2O_4$-NiO nanoparticles as well as the ones obtained for

RuO$_2$ and bare GCE are demonstrated in Figure 5.38a. Onset potential of 1.57 V (vs RHE) was observed for NiFe$_2$O$_4$-NiO nanoparticles suggesting a significant enhancement in the catalytic performance of GCE through alteration with nanoparticles. This value is comparable to or even smaller than those of previously reported similar structures such as NiO/NiFe$_2$O$_4$ nanorods (1.46 V vs RHE)[30], NiO/NiFe$_2$O$_4$ (1.50 V vs RHE)[88], NiO/NiFe$_2$O$_4$-rGO (1.436 V vs RHE)[71], NiFe$_2$O$_4$ nanofibers (1.67 V vs RHE) and NiFe$_2$O$_4$ nanoparticles (1.70 V vs RHE)[22]. Overpotential required to generate current density of 10 mA cm^{-2} (η_{10}) or even higher values is another essential parameter in the assessment of electrocatalytic activity of the nanomaterial. NiFe$_2$O$_4$-NiO nanoparticles can drive current densities of 10 and 20 mA cm^{-2} at overpotentials of 453 mV and 502 mV, respectively. On the other hand, RuO$_2$ can reach the same current densities at η_{10}=326 mV and η_{20}=380 mV. Nonetheless, it is also noteworthy at higher current densities (i.e 60 mA cm^{-2}) the activity of NiFe$_2$O$_4$-NiO becomes quite similar to that of RuO$_2$. RuO$_2$, for instance, produce current density of 60 mA cm^{-2} at an overpotential of 729 mV whereas NiFe$_2$O$_4$-NiO nanoparticles reach the same current density value at 760 mV. The most likely reason for this observation is the low stability of RuO$_2$ in alkaline medium under high anodic potentials, at which RuO$_2$ has been reported to oxidize to form RuO$_4$ and dissolve in solution.[6,89] The electrocatalytic activity results of NiFe$_2$O$_4$-NiO together with the ones of previously reported catalysts are summarized in Table 5.2.
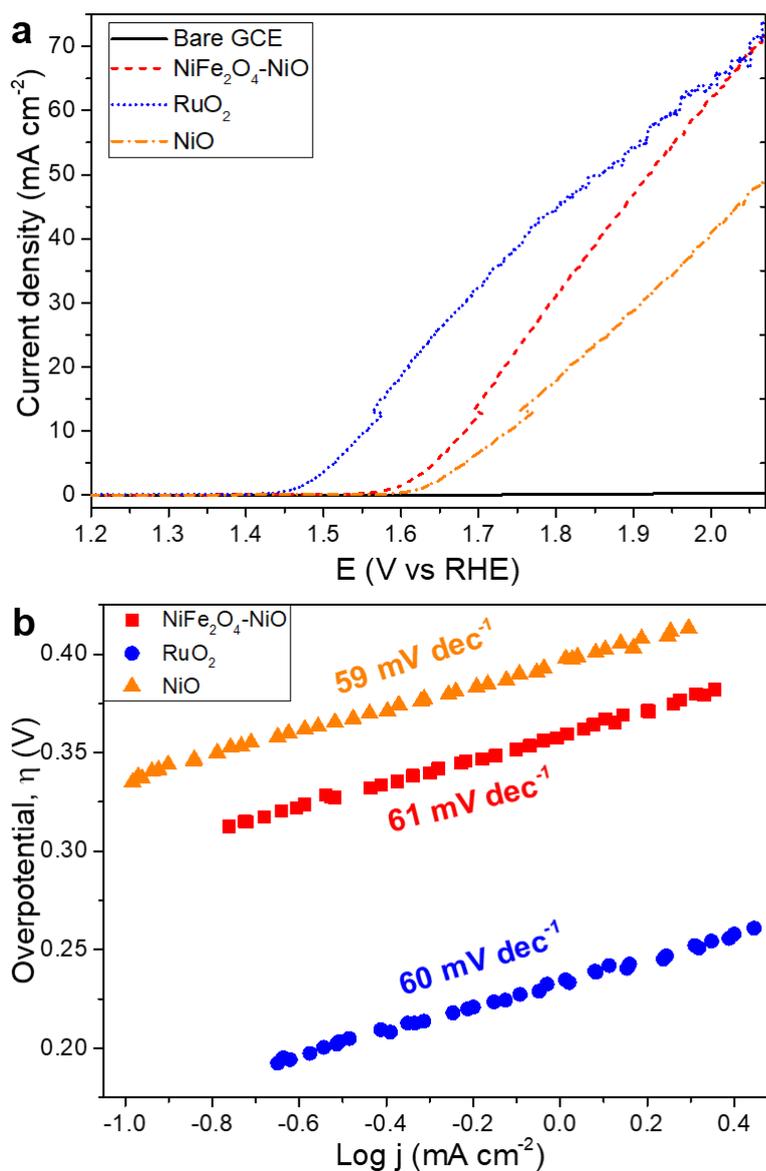
Figure 5.38. (a) Polarization curves of bare GCE, NiFe$_2$O$_4$-NiO nanoparticles, NiO and RuO$_2$ in 0.1 M KOH at a scan rate of 5 mV s^{-1} and (b) The corresponding Tafel plot obtained from polarization curves

Tafel slope, which can be obtained by fitting the linear part of polarization curve to Tafel equation, gives valuable insights about the electrocatalytic performance of the catalyst. Figure 5.38b shows the Tafel plots of NiFe$_2$O$_4$-NiO nanoparticles together with that of NiO and RuO$_2$, for comparison. Tafel slope of NiFe$_2$O$_4$-NiO

nanoparticles was calculated as 61 mV dec^{-1}, which is comparable to or even smaller than those of similar structure such as NiO/NiFe$_2$O$_4$ hollow cages (58.5 mV dec^{-1})[76], NiFe$_2$O$_4$ nanotubes (53.3 mV dec^{-1})[21], NiFe$_2$O$_4$/MWCNT (93 mV dec^{-1})[90], NiFe$_2$O$_4$/CNT (70 mV dec^{-1})[91], NiFe$_2$O$_4$ nanofibers (98.22 mV dec^{-1}) and NiFe$_2$O$_4$ nanoparticles (243.68 mV dec^{-1})[22]. In addition, Tafel slope of RuO$_2$ was determined 60 mV dec^{-1} pointing out that NiFe$_2$O$_4$-NiO nanoparticles exhibit comparable water oxidation kinetics to benchmark RuO$_2$ and previously reported nickel-iron oxide materials.

Table 5.2 Summary of the data for some recently reported representative water oxidation electrocatalysts and $NiFe_2O_4$-NiO nanoparticles

	Onset (RHE)	η_5 (mV)	η_{10} (mV)	Tafel slope (mV/dec)	Medium	REF
NiO-NiFe₂O₄	**1.57**	**412**	**453**	**61**	**0.1 M KOH**	**This work**
NiO/NiFe₂O₄ nanorods	1.46	-	302	42	1.0 M KOH	[30]
NiO/NiFe₂O₄ hollow cages	-	-	303	58.5	1.0 M KOH	[76]
NiO/NiFe₂O₄	1.50	-	370	48	1.0 M KOH	[88]
NiO/NiFe₂O₄-rGO	1.436	-	296	43	1.0 M KOH	[71]
NiFe₂O₄/MWCNT	1.38	-	-	93	0.1 M KOH	[90]
NiFe₂O₄/CNT	-	-	240	70	1.0 M KOH	[91]
NiFe₂O₄ nanorods	~1.55	-	342	44	1.0 M KOH	[31]
NiFe₂O₄ nanotubes	-	-	340	53.3	1.0 M KOH	[21]
CoFe₂O₄ nanotubes	-	-	392	64	1.0 M KOH	[21]
Fe₃O₄ nanotubes	-	-	432	122.5	1.0 M KOH	[21]
NiFe₂O₄ nanofibers	1.67	470	-	98.22	0.1 M KOH	[22]
NiFe₂O₄ nanoparticles	1.70	550	-	243.68	0.1 M KOH	[22]
CuFe₂O₄ nanofibers	1.64	450	-	93.97	0.1 M KOH	[22]
CuFe₂O₄ nanoparticles	1.71	540	-	237.32	0.1 M KOH	[22]
CoFe₂O₄ nanofibers	1.60	410	-	82.15	0.1 M KOH	[22]
CoFe₂O₄ nanoparticles	1.67	520	-	223.27	0.1 M KOH	[22]
MnFe₂O₄ nanofibers	1.67	520	-	113.62	0.1 M KOH	[22]
MnFe₂O₄ nanoparticles	1.72	640	-	249.16	0.1 M KOH	[22]
Fe₂O₃ nanofibers	1.71	550	-	148.84	0.1 M KOH	[22]
Fe₂O₃ nanoparticles	1.79	750	-	285.59	0.1 M KOH	[22]
RuO₂	1.45	282	326	60	0.1 M KOH	This work
NiO	1.60	450	510	59	0.1 M KOH	This work

Number of active sites on nanomaterials' surface play a crucial role in catalyst activity. Therefore, ECSA and RF, which are directly proportional to the number of active sites are also used for the evaluation of the electrocatalytic activity. ECSA can be estimated by C_{dl}. CVs at non-Faradaic potential range are recorded at various scan

rates to determine the C_{dl} of $NiFe_2O_4$-NiO nanomaterials (Figure 5.39). The slope of double-layer charging current (at 1.27 V vs RHE) versus scan rate plot gives the C_{dl} value of the catalyst. $NiFe_2O_4$-NiO nanoparticles have C_{dl} value of 0.061 mF and ECSA of 1.02 cm^2. In addition, RF value was determined as 14.6. Mass activity and specific activity of $NiFe_2O_4$-NiO nanoparticles was calculated at an overpotential of 760 mV and found as 150 A g^{-1} and 4.12 mA cm$^{-2}_{ECSA}$ while they were calculated as 165 A g^{-1} and 0.23 mA cm$^{-2}_{ECSA}$ for RuO_2, respectively. Mass activity value obtained for $NiFe_2O_4$-NiO nanoparticles is very close to that of RuO_2 verifying the comparable electrocatalytic activity of them.
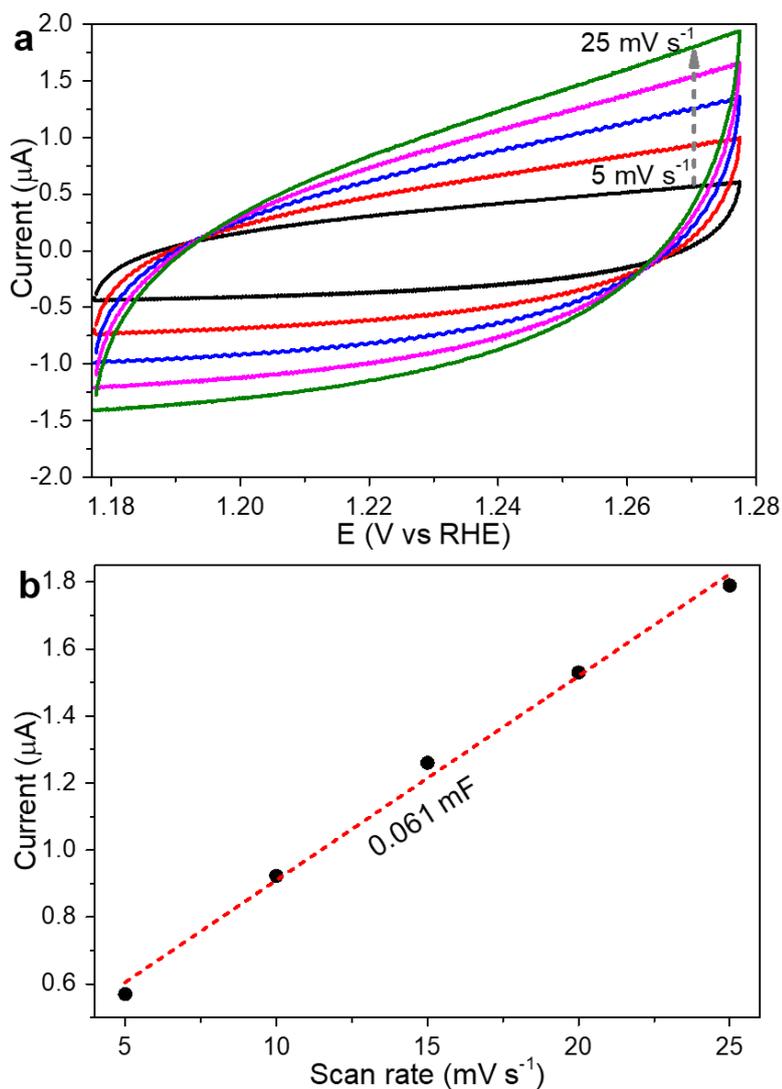
Figure 5.39. (a) CVs of NiFe₂O₄-NiO nanoparticles measured at different scan rate from 5 to 25 mV s^{-1} and (b) Plot of current at 1.27 V (vs RHE) vs scan rate

The kinetic properties of NiFe₂O₄-NiO nanoparticles further investigated by EIS. Nyquist plots of the catalyst obtained at various overpotentials are given in Figure 5.40. The semicircles were fitted to CPE model, where solution resistance and charge transfer resistance (R_{ct}) are denoted as R_u and R_p, respectively. As the applied overpotential increase, a decrease in diameter of the semicircles is observed implying

the reduction of charge transfer resistance. Improvement of the electrical conductivity with lower R_{ct}, and thus easier charge transfer leads to enhanced catalytic activity of NiFe$_2$O$_4$-NiO nanoparticles during water oxidation reaction.
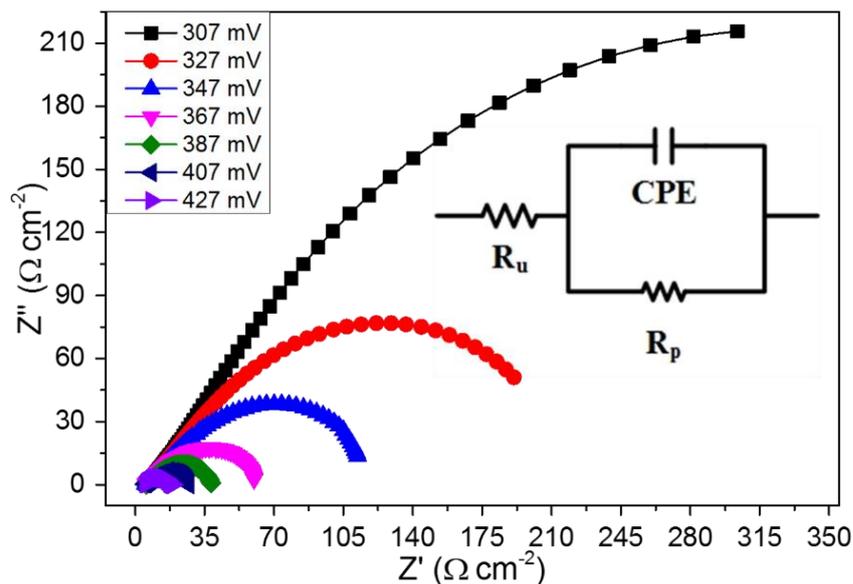
Figure 5.40. Nyquist plots of NiFe$_2$O$_4$/NiO nanoparticles at various overpotentials (inset shows the equivalent curcuit diagram)

The assessment of NiFe$_2$O$_4$-NiO nanoparticles' stability was done by employing controlled potential coulometry in 0.1 M KOH solution. Overpotential of 415 mV was applied for 18000 s and polarization curves were recorded before and after electrolysis (Figure 5.41). A very slight increase in η_{10} (453 mV to 470 mV) was recorded while no change was observed on the onset potential signifying high stability of the synthesized nanomaterials during water oxidation.
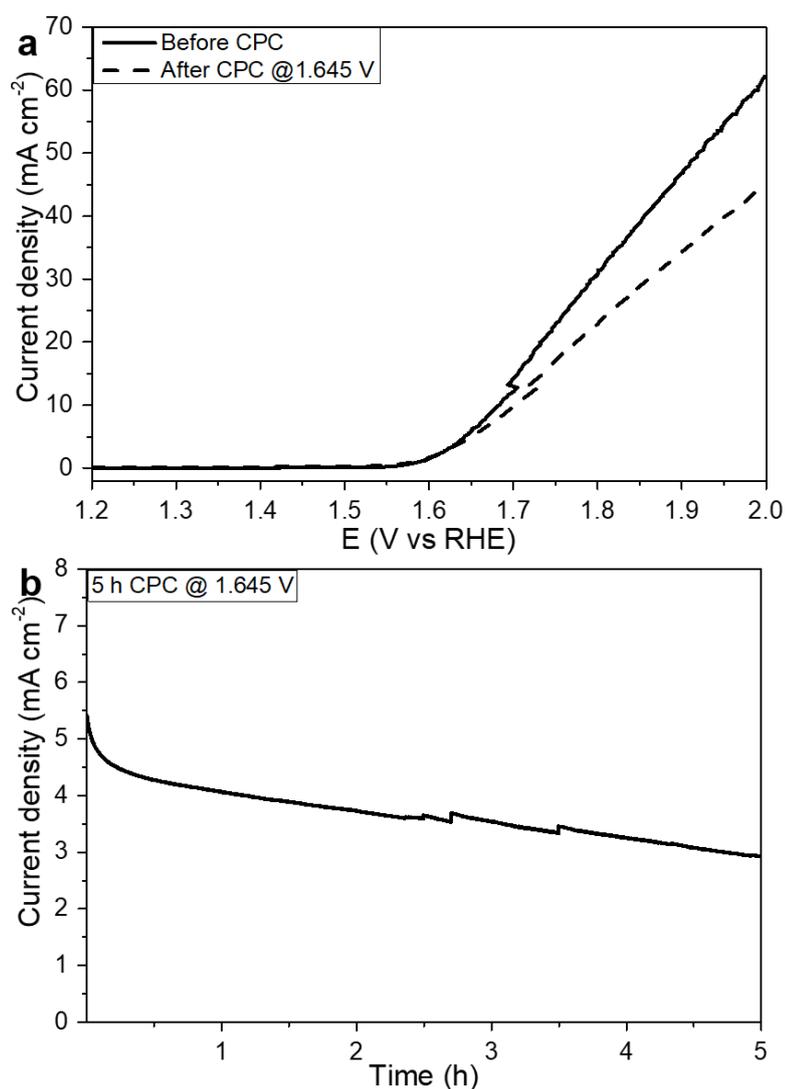
Figure 5.41. (a) Polarization curves of NiFe$_2$O$_4$-NiO nanoparticles recorded before and after controlled potential electrolysis at overpotential corresponding to initial current density of 5 mA cm^{-2} and (b) Change in current density during electrolysis in 0.1 M KOH

5.2.4 Electrocatalytic activities of NiCo$_2$O$_4$-NiO microspheres

The electrocatalytic activities of NiCo$_2$O$_4$-NiO microspheres towards water oxidation reaction were evaluated using LSV. GCE modified with NiCo$_2$O$_4$-NiO

microspheres were used as working electrodes and the electrochemical measurements were performed in alkaline medium (0.1 M KOH) at room temperature. Figure 5.42a shows the resulting polarization curves as well as the ones obtained for bare RuO_2, Co_3O_4, NiO and GCE. Inspection of the data revealed that the electrocatalytic performance of GCE was significantly improved upon modification with $NiCo_2O_4$-NiO. The onset potentials of U-NiCo and C-NiCo were found to be 1.56 V and 1.57 V (vs RHE), respectively. These values are comparable to or even smaller than those of similar previously reported materials such as $NiCo_2O_4$ nanowires (1.56 V vs RHE)[26], $NiCo_2O_4$ (1.63 V vs RHE)[25], $NiCo_2O_4$ (1.66 V vs RHE)[29], $NiCo_2O_4$-NiO nanosheets (1.59 V vs RHE)[29] and MOF-derived $NiCo_2O_4$-NiO (1.58 V vs RHE)[86]. Although U-NiCo and C-NiCo exhibit similar onset potentials, differences in overpotentials to drive the same catalytic current densities were noted. U-NiCo can generate current densities of 10 mA cm^{-2} (η_{10}) and 20 mA cm^{-2} (η_{20}) at overpotentials of 387 mV and 410 mV, respectively. For C-NiCo, on the other hand, η_{10} and η_{20} were measured as 430 mV and 467 mV, respectively. As these results suggest, U-NiCo exhibits better electrocatalytic activity than C-NiCo. The activities of $NiCo_2O_4$-NiO microspheres were also compared to that of RuO_2 under the same conditions. RuO_2 demands overpotentials of 326 mV and 380 mV to reach 10 and 20 mA cm^{-2}. However, it is also important to note that U-NiCo demonstrates better electrocatalytic performance than RuO_2 at higher current densities (i.e. current densities > 30 mA cm^{-2}) (Figure 3.32a). For instance, U-NiCo can generate current density of 50 mA cm^{-2} at an overpotential of 518 mV while RuO_2 requires 622 mV to reach the same current density value. As mentioned in $NiFe_2O_4$-NiO nanomaterials, the reason for this observation is the low stability of RuO_2 in alkaline medium under high anodic potentials, at which RuO_2 has been reported to oxidize to form RuO_4 and dissolve in solution.[6,89] In addition, RuO_2 is known to be the best electrocatalyst for water oxidation reaction, and thus it is expected to observe high amount of gas formation. At higher applied potential, the gas bubble formation increases and accumulates on to electrode surface blocking the electrode which has a very small surface area (0.07 cm^2). The observed lower current

density at higher potential for RuO_2 is due to this gas accumulation on the electrode surface. The results obtained from $NiCo_2O_4$-NiO microspheres are summarized in Table 5.3, along with the ones of previously reported similar catalysts, for comparison.
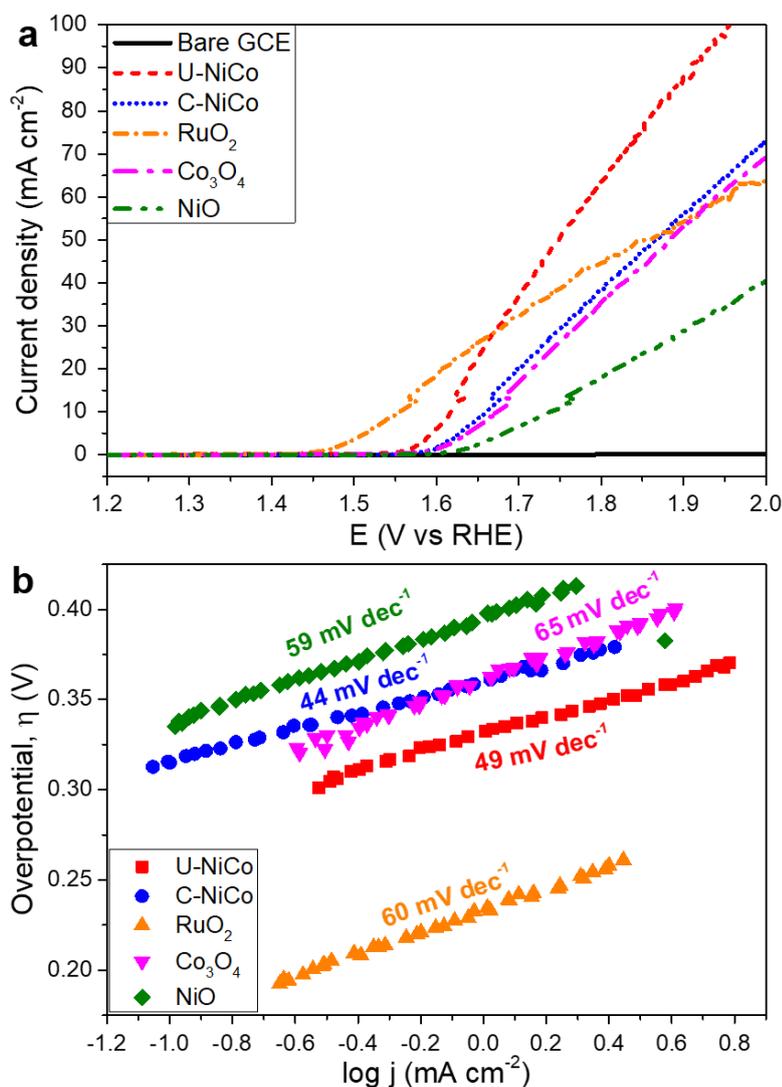
Figure 5.42. (a) Polarization curves of bare GCE, $NiCo_2O_4$-NiO microspheres, RuO_2, Co_3O_4 and NiO in 0.1 M KOH at a scan rate of 5 mV s^{-1} and (b) The corresponding Tafel plots obtained from polarization curves

The water oxidation kinetics of $NiCo_2O_4$-NiO microspheres were elucidated by fitting the linear part of polarization curves to Tafel equation. Tafel slopes of U-NiCo and C-NiCo were determined as 49 and 44 mV dec^{-1}, respectively (Figure 5.42b). The slopes of $NiCo_2O_4$-NiO microspheres were calculated as smaller than the ones of both supported and free-standing nickel-cobalt oxide electrocatalysts such as MOF-derived $NiCo_2O_4$-NiO (49 mV dec^{-1}) and MOF-derived NiO-$NiCo_2O_4$-rGO (66 mV dec^{-1})[86], $NiCo_2O_4$-NiO nanosheets (61 mV dec^{-1})[29], $NiCo_2O_4$ nanoframes (82 mV dec^{-1})[56], $NiCo_2O_4$-NiO nanocrystals (79 mV dec^{-1})[85] and $NiCo_2O_4$ nanowires (60 mV dec^{-1})[26]. For comparison, Tafel slope of RuO_2 and Co_3O_4 were determined as 60 and 65 mV dec^{-1}, respectively. These results verify that U-NiCo and C-NiCo microspheres demonstrate faster water oxidation kinetics than benchmark RuO_2, Co_3O_4 and previously reported nickel cobalt oxide catalysts in different morphologies and/or on various supports.

Table 5.3 Summary of some recently reported representative water oxidation electrocatalysts and $NiCo_2O_4$-NiO microspheres

	Onset (RHE)	η_{10} (mV)	η_{50} (mV)	Tafel slope (mV/dec)	Medium	REF
U-NiCo₂O₄-NiO	**1.56**	**387**	**518**	**49**	**0.1 M KOH**	**This work**[14]
C-NiCo₂O₄-NiO	**1.57**	**430**	**638**	**44**	**0.1 M KOH**	**This work**[14]
NiO/NiCo₂O₄ nanosheets	1.59	360	-	61	1.0 M NaOH	[29]
NiCo₂O₄	1.66	430	-	139	1.0 M NaOH	[29]
NiO/NiCo₂O₄ nanocrystals	-	264	-	79.3	1.0 M KOH	[85]
NiCo₂O₄ on stainless steel	1.6	530	-	49	0.1 M NaOH	[24]
NiCo₂O₄ nanoframes (Cu₂O)	-	265	-	82	1.0 M KOH	[56]
NiCo₂O₄ nanowires	1.56	-	-	60	1.0 M KOH	[26]
NiCo₂O₄ nanowires	-	460	-	90	1.0 M KOH	[27]
MOF-NiO/NiCo₂O₄	1.58	410	-	49	1.0 M KOH	[86]
MOF-NiO/NiCo₂O₄-rGO	1.51	340	-	66	1.0 M KOH	[86]
NiCo₂O₄@NiO@Ni	1.45	240	-	43	1.0 M KOH	[83]
NiCo₂O₄	1.63	440	-	85	1.0 M KOH	[25]
NiCo₂O₄ nanowire array	-	350	-	62	1.0 M KOH	[28]
RuO₂	1.45	326	622	60	0.1 M KOH	This work
Co₃O₄	1.59	443	653	65	0.1 M KOH	This work
NiO	1.60	510	704	59	0.1 M KOH	This work

Further evaluation of the polarization curve demonstrates a broad oxidation peak at ca. 1.4 V (vs. RHE) suggesting the formation of active species; NiOOH and CoOOH during water oxidation (Figure 5.43).[30,83,85,92] It has been reported that oxidation of Ni^{2+} in NiO and $NiCo_2O_4$ lead to formation of NiOOH ($NiO + OH^- \rightarrow NiOOH + e^-$) along with CoOOH ($NiCo_2O_4 + OH^- \rightarrow NiOOH + 2CoOOH + e^-$) in alkaline medium.[30,83,85,92] Thus, area of the observed oxidation peak affirms the formation of these active species during catalysis, and associate with the water oxidation performance of the catalyst. Therefore, comparison of the oxidation peak intensity

for U-NiCo and C-NiCo suggest that water oxidation efficiency of U-NiCo with higher peak intensity is better than the one of C-NiCo.
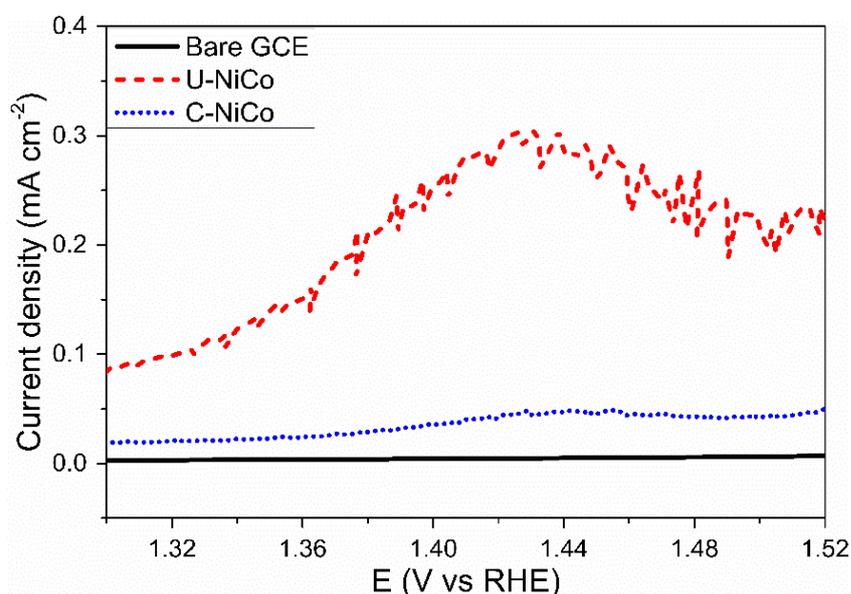
Figure 5.43. Polarization curves (in 1.30-1.52 V range) of bare GCE, U- and C-NiCo microspheres in 0.1 M KOH at a scan rate of 5 mV s^{-1}

ECSA was also estimated for the U- and C-NiCo microspheres by determining C_{dl} values (Figure 5.44). For U-NiCo, C_{dl} and ECSA were determined as 0.185 mF and 3.08 cm^2, respectively. On the other hand, C-NiCo has C_{dl} value of 0.095 mF and ECSA of 1.58 cm^2. Furthermore, RF values for U-NiCo and C-NiCo were determined to be 44 and 22.6, respectively. Higher C_{dl}, ECSA and RF values verify that U-NiCo possess larger number of active sites, and thus exhibit better electrocatalytic performance towards water oxidation reaction. At overpotential of 518 mV, mass activities and specific activities of both NiCo$_2$O$_4$-NiO microspheres were calculated as 125 A g^{-1} and 1.14 mA cm$^{-2}_{ECSA}$ for U-NiCo while they were found to be 72.5 A g^{-1} and 1.28 mA cm$^{-2}_{ECSA}$ for C-NiCo, respectively. Higher mass and specific activities further confirm higher electrocatalytic activity of U-NiCo compared to C-NiCo. Furthermore, both U-NiO and C-NiO have significantly higher

mass activity and specific activity than those of monometallic Co_3O_4 (64.8 A g^{-1}, 0.93 mA cm^{-2}_{ECSA}) and NiO (61.6 A g^{-1}, 0.80 mA cm^{-2}_{ECSA}). All mass and specific activity calculated in this study are summarized in Table 5.4.
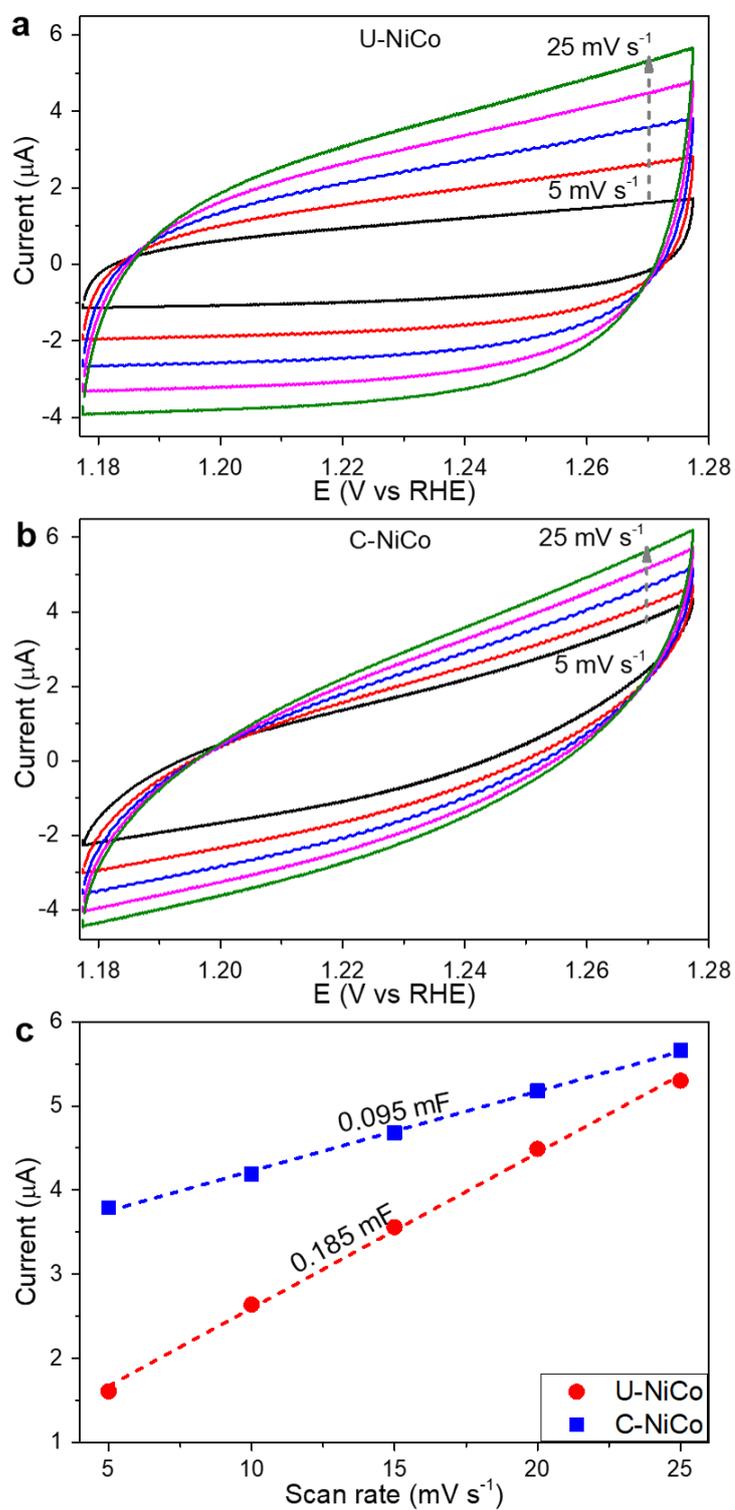
Figure 5.44. CVs of (a) U-NiCo, (b) C-NiCo microspheres measured at different scan rates from 5 to 25 mV s^{-1} and (c) Plot of current density at 1.27 V (vs RHE) vs scan rate of NiCo$_2$O$_4$-NiO microspheres

Table 5.4 Summary of water oxidation properties of $NiCo_2O_4$-NiO microspheres

	Mass activity (A g^{-1}) at η=518 mV	Specific activity (mA cm^{-2}$_{ECSA}$)	C$_{dl}$ (mF)	ECSA (cm^2)	RF
U-NiCo$_2$O$_4$-NiO	125	1.14	0.185	3.08	44
C-NiCo$_2$O$_4$-NiO	72.5	1.28	0.095	1.58	22.6
NiO	61.6	0.8	0.129	2.15	30.7
Co$_3$O$_4$	64.8	0.93	0.078	1.95	27.8

The kinetics of the prepared catalysts in water oxidation reaction were further examined by EIS at various overpotentials. Nyquist plots of both U-NiCo and C-NiCo exhibited semicircles fitted to equivalent circuit of CPE, which is composed of R_u, constant-phase element and R_p (R_{ct}) (Figure 5.45). Diameter of the semicircles, which are associated with R_{ct}, decrease with the increasing overpotential. Lower charge transfer resistance indicates improved electrical conductivity resulting an increase in charge transfer during OER. The results reveal that U-NiCo has smaller R_{ct} (13.2 Ω) than the one of C-NiCo (18.5 Ω) at same applied potential (i.e. 640 mV vs Ag/AgCl), suggesting better conductivity and thus catalytic activity of U-NiCo.
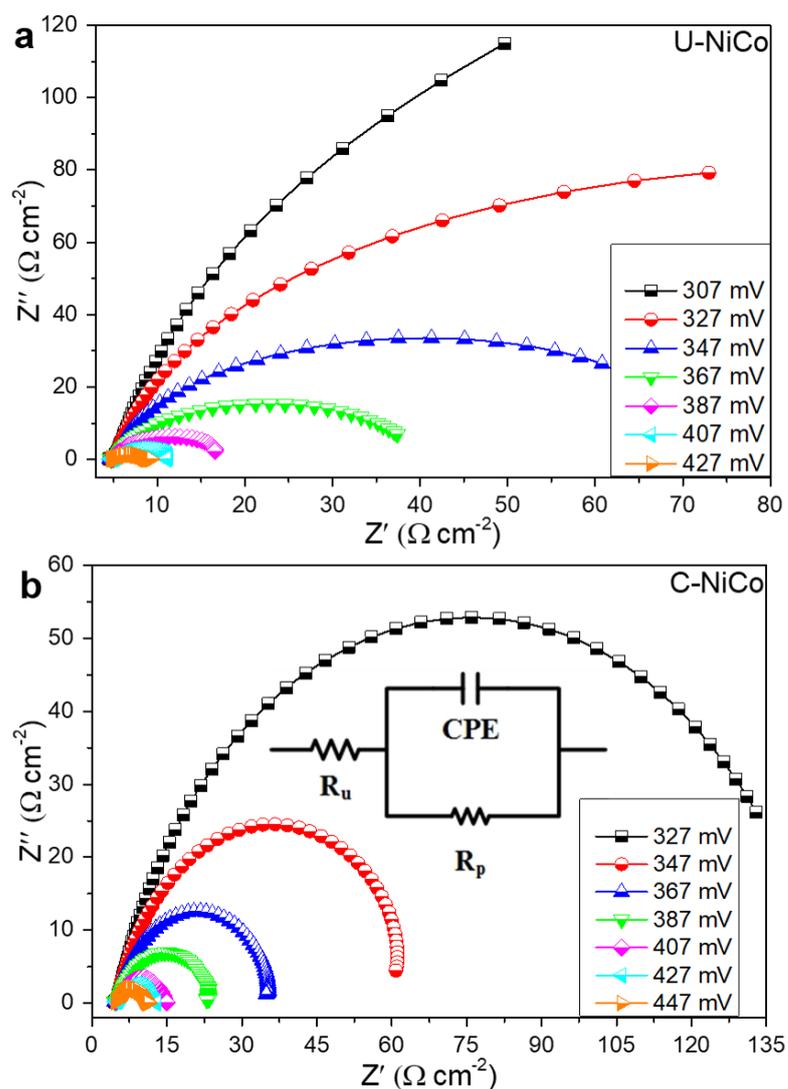
Figure 5.45. Nyquist plots of (a) U-NiCo and (b) C-NiCo microspheres at various overpotentials (inset shows the equivalent circuit diagram)

The durability of an electrocatalyst is a significant factor affecting its practical applications. Therefore, the stability of GCEs modified with $NiCo_2O_4$-NiO nanomaterials were tested employing constant potential electrolysis in 0.1 M KOH solution. Overpotentials of 365 mV and 400 mV were applied for 10800 s for U-NiCo and C-NiCo, respectively. Figures 5.46a and 5.47a show the polarization curves recorded before and after electrolysis. A slight shift to higher overpotential

value (430 mV to 455 mV) at current density of 10 mA cm^{-2} was noted for C-NiCo while no noticeable change was recorded for U-NiCo. In addition, onset potentials of both U-NiCo and C-NiCo remained unchanged after 3 h of electrolysis, indicating that NiCo$_2$O$_4$/NiO microspheres exhibit good stability under alkaline conditions.
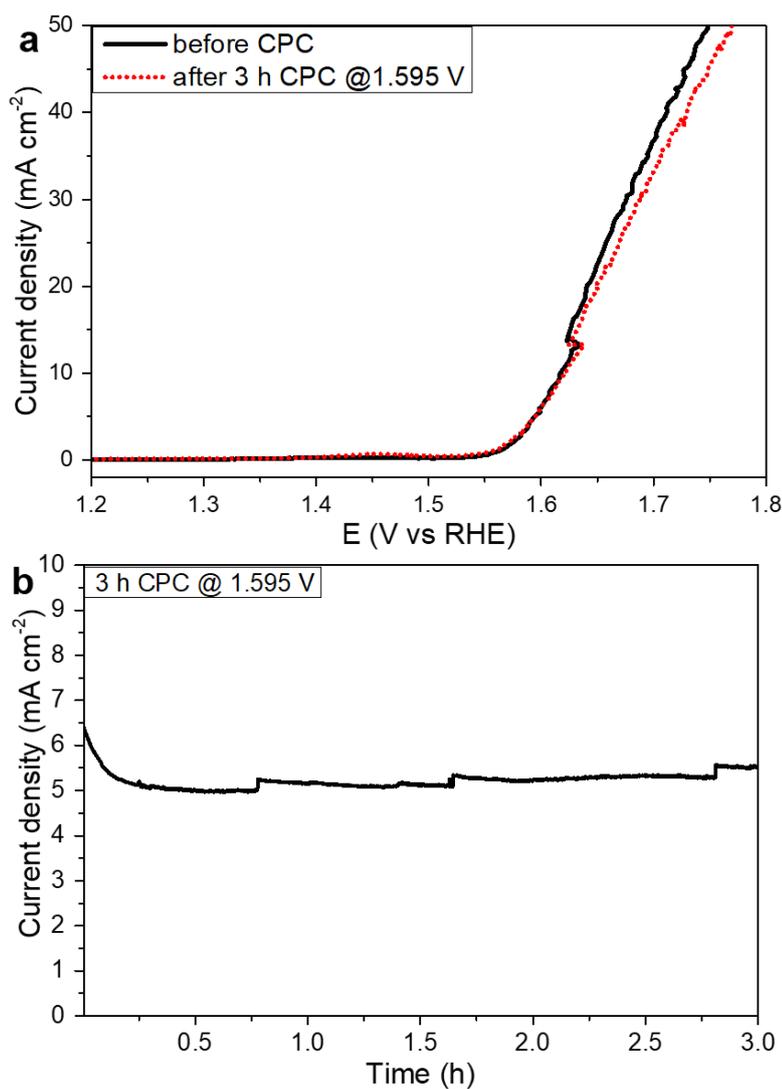
Figure 5.46. (a) Polarization curves of U-NiCo microspheres recorded before and after controlled potential electrolysis at overpotential corresponding to initial current density of 5 mA cm^{-2} and (b) The change in current density during electrolysis in 0.1 M KOH
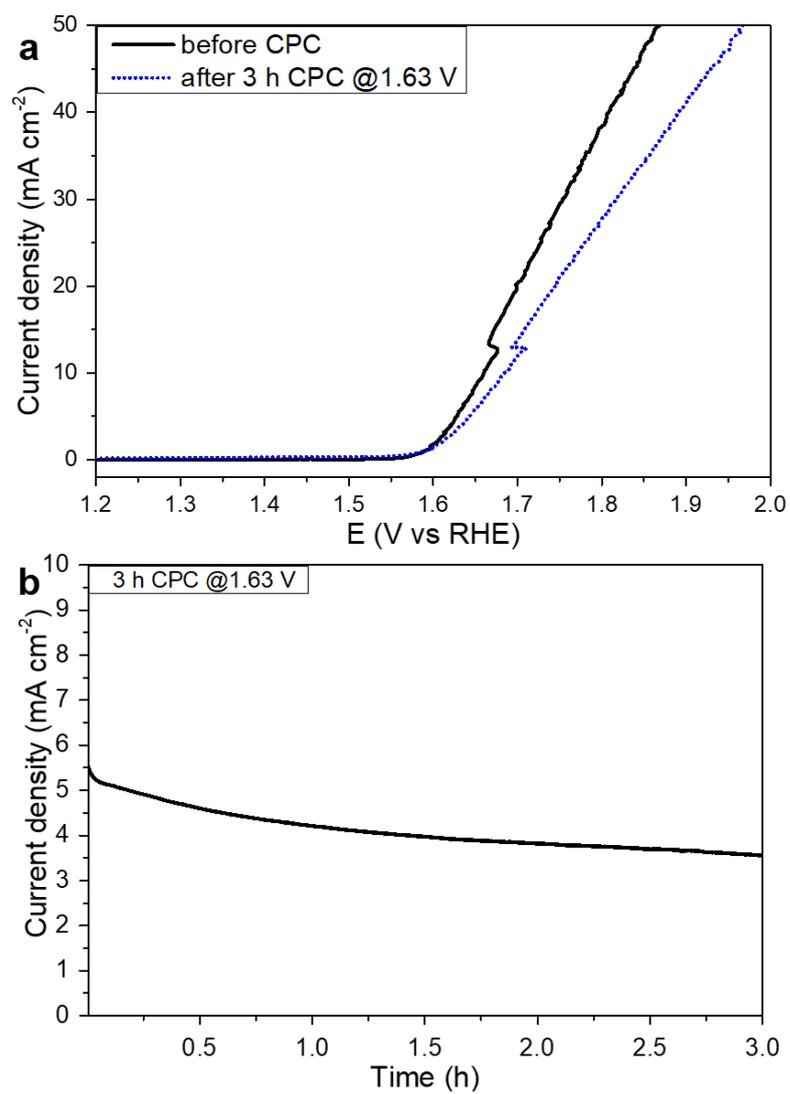
Figure 5.47. (a) Polarization curves of C-NiCo microspheres recorded before and after controlled potential electrolysis at overpotential corresponding to initial current density of 5 mA cm^{-2} and (b) The change in current density during electrolysis in 0.1 M KOH

5.2.5 Evaluation of electrocatalytic activities of the synthesized transition metal oxide nanomaterials for water oxidation reaction

Catalytic activity of the synthesized nanomaterials towards water oxidation reaction is governed by several chemical and morphological properties of the materials. Foremost, the large surface area, as evidenced by BET analyses (Table 5.5), enables more contact areas between electrode and electrolyte, facilitating the adsorption of the reactants and reaction intermediates. They are also valuable for enhanced electron transfer, and thus catalytic water oxidation.

In addition to surface area, presence of defect sites with low oxygen coordination in the material is also a significant parameter influencing the water oxidation activity of the catalyst. A number of studies reported that oxygen vacant sites promote H_2O adsorption onto catalyst surface. Consequently, it improves the reactivity of the catalyst.[8,93–95] XPS O1s core-level spectra exhibit the presence of oxygen vacancies in all of the synthesized nanomaterials. Further inspection of the spectra revealed that relative peak areas are 51%, 46%, 61%, 63% and 58% for $CuCr_2O_4$ nanoparticles, $FeMnO_3$ nanowires, $NiFe_2O_4$-NiO nanoparticles, U-NiCo and C-NiCo microspheres, respectively. These slight differences in degree of oxygen deficiency is believed to contribute the variances in catalytic activity of the nanomaterials.

Table 5.5 Comparison of BET surface areas and degree of oxygen deficiencies of the synthesized nanomaterials

Catalyst	BET surface area (m^2 g^{-1})	Degree of oxygen deficiency (%)
$CuCr_2O_4$	10.63	51
$FeMnO_3$	14.21	46
$NiFe_2O_4$-NiO	79.04	61
C-NiCo	13.40	58
U-NiCo	41.30	63

It has also been proposed that co-presence of two different metals in the structure can promote formation of multiple valence states of the cations.[7,85,96] XPS spectra of the synthesized nanomaterials affirm the presence of metals with multiple oxidation states in each material. For instance, $Fe^{2+/3+}$ and $Mn^{3+/4+}$ ions coexist in nanowire structure. Furthermore, both U-NiCo and C-NiCo microspheres embody $Ni^{2+/3+}$ and $Co^{2+/3+}$ ions in their structure. The formation of such redox couples leads to higher electrical conductivity and enhanced surface adsorption properties, and thus improved electrocatalytic performances towards water oxidation reaction.
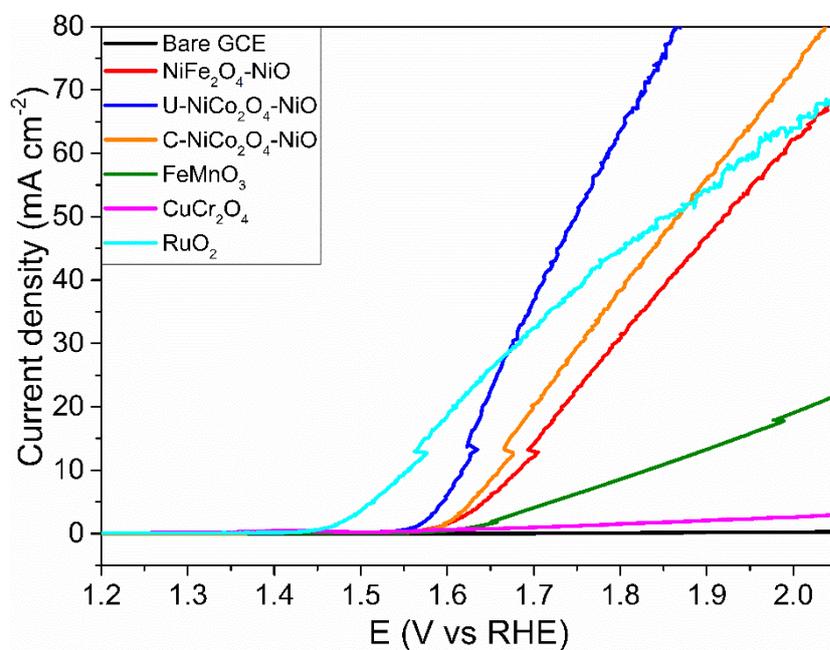
Figure 5.48. Polarization curves of bare GCE, CuCr$_2$O$_4$ nanoparticles, FeMnO$_3$ nanowires, NiFe$_2$O$_4$-NiO nanoparticles, NiCo$_2$O$_4$-NiO microspheres and RuO$_2$ in 0.1 M KOH solution at a scan rate of 5 mV s^{-1}

Table 5.6 Summary of water oxidation activity data of the nanomaterials synthesized in this study

	Electrode (cm^2)	Catalyst loading (mg cm^{-2})	Onset (RHE)	η_{10} (mV)	η_{50} (mV)	Tafel slope (mV/dec)	ECSA (cm^2)	RF
U-NiCo	GC (0.07)	0.4	1.56	387	518	49	3.08	44
C-NiCo$_2$	GC (0.07)	0.4	1.57	430	638	44	1.58	22.6
NiFe$_2$O$_4$-NiO	GC (0.07)	0.4	1.57	453	688	61	1.02	14.6
FeMnO$_3$*	FTO (0.5)	0.92	1.60	600	-	87	29.6	59.2
CuCr$_2$O$_4$	GC (0.07)	0.4	2.07	1050	-	67	-	-
RuO$_2$	GC (0.07)	0.4	1.45	326	622	60	20.5	292.8

* Surface area of electrode and catalyst loading is higher than the other studied electrodes.

Large surface area and presence of low oxygen coordination sites are significant parameters in the interpretation of catalyst activity. However, having larger surface area or higher degree of oxygen deficiency does not always result in more enhanced electrocatalytic activity. For instance, when relation of oxygen deficiency and catalytic activity of studied materials are compared, CuCr$_2$O$_4$ nanoparticles with relatively higher oxygen deficiency than FeMnO$_3$ nanowires have significantly lower activity in OER. On the other hand, comparison of BET surface areas reveal that CuCr$_2$O$_4$ has the lowest area among all synthesized materials. NiFe$_2$O$_4$-NiO nanoparticles are expected to have the highest catalytic activity for water oxidation reaction since they bear the largest surface area. In addition, having similar BET surface areas of 14.21 m^2 g^{-1} and 13.40 m^2 g^{-1}, FeMnO$_3$ nanowires and C-NiCo microspheres should display similar performance, respectively. Nevertheless, U-NiCo microspheres exhibit the highest electrocatalytic activity with its lower BET surface area of 41.30 m^2 g^{-1} compared to that of NiFe$_2$O$_4$-NiO nanoparticles (Figure 5.47). These comparisons suggest that oxygen deficiency and/or surface area can not be considered as only parameters affecting catalytic activity, and individual or combination of possible other factors such as chemical composition, electrochemically active surface area and conductivity can be the reason for observed activities. Therefore, determination of ECSA, which is directly related with the

number of sites acting as catalyst, is crucial to make more reliable assessment of catalyst performance. As summarized in Table 5.6, enhancement of the water oxidation activity is observed with increasing ECSA of the catalyst. $FeMnO_3$ nanowires exhibit lower electrocatalytic activity than the Ni-based ones even though it has the largest ECSA value. It is important to note that the large ECSA value is most likely due to the large surface area of FTO electrode and the higher amount of catalyst on the surface. In addition, RuO_2 has the largest ECSA value which correlate well with the observed water oxidation activity. Thus, our results clearly show that increase in the ECSA of the studied catalyst results in the increased activity as expected.

CHAPTER 6

CONCLUSIONS

The aim of this thesis was to design and prepare bimetallic oxide nanomaterials using earth abundant, first row transition metals to be used as catalysts in the electrochemical water oxidation reaction. Synthesized materials were characterized by a combination of analytical techniques including SEM, TEM, EDX, XRD, XPS, ICP-OES and BET. Then, their activities were studied for water oxidation reaction by utilizing electrochemical techniques.

In summary, a series of bimetallic transition metal oxide nanomaterials with various morphologies were synthesized by facile, solution-phase procedures using different structure directing agents. Specifically, $CuCr_2O_4$ nanoparticles were obtained via sol-gel route in which citric acid was used as surfactant. $FeMnO_3$, $NiFe_2O_4$-NiO and $NiCo_2O_4$-NiO nanomaterials were obtained by utilizing hydrothermal process. NTA was used as structure directing agent in the synthesis of $FeMnO_3$, while $NiFe_2O_4$-NiO and $NiCo_2O_4$-NiO were synthesized with the use of urea. In addition to urea, CTAC was also used as structure directing agent in the synthesis of $NiCo_2O_4$-NiO.

Electron microscopy studies revealed that synthesized materials comprise of assembled individual nanoparticles. $CuCr_2O_4$ nanoparticles are of quasi-spherical morphology with average size of 28 nm. $FeMnO_3$ nanowires are formed by the assembly of approximately 70 nm particles. $NiFe_2O_4$-NiO nanoparticles resulted from the accumulation of approximately 30 nm spherical like particles. Moreover, by using two different surfactants, namely urea and CTAC, $NiCo_2O_4$-NiO nanomaterials are obtained as microspheres. Urea-stabilized $NiCo_2O_4$-NiO has urchin-like morphology assembled by nanowires, and CTAC stabilization lead to the formation of microspheres with nanoplate assembly. In addition, both wires and plates are composed of individual nanoparticles.

The electrocatalytic performances of synthesized nanomaterials in water oxidation reaction were evaluated in alkaline medium (0.1 M KOH) (Figure 5.48). The results revealed that $CuCr_2O_4$ nanoparticles exhibit almost no activity towards water oxidation reaction with very high onset (2.07 V vs RHE) and overpotentials (η_{10} = 1.05 V). $FeMnO_3$ nanowires had onset potential of 1.60 V (vs RHE) with an overpotential of 600 mV at current density of 10 mA cm^{-2} and Tafel slope of 87 mV dec^{-1}. $NiFe_2O_4$-NiO nanoparticles demonstrate slightly better activity with an onset potential of 1.57 V (vs RHE), and overpotential required to generate current density of 10 mA cm^{-2} was 453 mV. In addition, Tafel slope was determined as 61 mV dec^{-1} indicating faster water oxidation kinetics. $NiCo_2O_4$-NiO microspheres, on the other hand, present more enhanced activity. Onset potentials observed for U-NiCo and C-NiCo were 1.56 V (vs RHE) and 1.57 V (vs RHE), respectively. Additionally, U-NiCo and C-NiCo can promote 10 mA cm^{-2} current density at lower overpotentials of 387 mV and 430 mV, respectively. Tafel slope of U-NiCo was determined as 49 mV dec^{-1} while for C-NiCo it was found as 44 mV dec^{-1}. These results suggest that $NiCo_2O_4$-NiO microspheres display the best water oxidation activity among the nanomaterials synthesized in this study (Table 5.6).

The durability of the prepared catalysts was also studied by long term controlled potential coulometry. After 3 h of electrolysis, a slight increase in onset potential was noted for $FeMnO_3$ nanowires. On the other hand, this value remained constant for $NiFe_2O_4$-NiO nanoparticles (after 5 h of electrolysis) and $NiCo_2O_4$-NiO microspheres (after 3 h of electrolysis) indicating very good stability of these materials during water oxidation reaction.

As a result, bimetallic transition metal oxide nanomaterials, namely $CuCr_2O_4$ nanoparticles, $FeMnO_3$ nanowires, $NiFe_2O_4$-NiO nanoparticles and $NiCo_2O_4$-NiO hierarchical microspheres with interesting morphologies were synthesized and their electrochemical activities for water oxidation reaction were investigated. The overall water oxidation activity of the synthesized materials was observed to be comparable or superior to some of the water oxidation electrocatalysts having similar structures. These new materials with their exciting morphologies, easy synthesis from earth

abundant elements, stability and ability to deliver high current densities are practically very useful and effective catalysts for water oxidation reaction.

For future work, water oxidation reaction mechanism, the active sites in each catalyst as well as the rate determining step can be investigated in detail with the aid of computational analysis. Moreover, their potential utility in other applications such as supercapacitors, metal-air batteries, hydrogen evolution reaction (HER), oxygen reduction reaction (ORR) or various other catalysis applications such as dehydrogenation, hydrogen peroxide reduction, CO oxidation.

REFERENCES

(1)   Grzelczak, M.; Zhang, J.; Pfrommer, J.; Hartmann, J.; Driess, M.; Antonietti, M.; Wang, X. Electro- and Photochemical Water Oxidation on Ligand-Free Co_3O_4 Nanoparticles with Tunable Sizes. *ACS Catal.* **2013**, *3*, 383–388. https://doi.org/10.1021/cs3007523.

(2)   Gao, M.; Sheng, W.; Zhuang, Z.; Fang, Q.; Gu, S.; Jiang, J.; Yan, Y. Efficient Water Oxidation Using Nanostructured α-Nickel-Hydroxide as an Electrocatalyst. *J. Am. Chem. Soc.* **2014**, *136*, 7077–7084. https://doi.org/10.1021/ja502128j.

(3)   Liu, X.; Cui, S.; Sun, Z.; Du, P. Copper Oxide Nanomaterials Synthesized from Simple Copper Salts as Active Catalysts for Electrocatalytic Water Oxidation. *Electrochim. Acta* **2015**, *160*, 202–208. https://doi.org/10.1016/j.electacta.2015.01.123.

(4)   Liu, J.; Nan, Y.; Chang, X.; Li, X.; Fang, Y.; Liu, Y.; Tang, Y.; Wang, X.; Li, R.; Ma, J. Hierarchical Nitrogen-Enriched Porous Carbon Materials Derived from Schiff-Base Networks Supported $FeCo_2O_4$ Nanoparticles for Efficient Water Oxidation. *Int. J. Hydrogen Energy* **2017**, *42*, 10802–10812. https://doi.org/10.1016/j.ijhydene.2017.03.100.

(5)   Sun, C.; Yang, J.; Dai, Z.; Wang, X.; Zhang, Y.; Li, L.; Chen, P.; Huang, W.; Dong, X. Nanowires Assembled from $MnCo_2O_4$@C Nanoparticles for Water Splitting and All-Solid-State Supercapacitor. *Nano Res.* **2016**, *9*, 1300–1309. https://doi.org/10.1007/s12274-016-1025-x.

(6)   Suen, N.-T.; Hung, S.-F.; Quan, Q.; Zhang, N.; Xu, Y.-J.; Chen, H. M. Electrocatalysis for the Oxygen Evolution Reaction: Recent Development and Future Perspectives. *Chem. Soc. Rev.* **2017**, *46*, 337–365. https://doi.org/10.1039/C6CS00328A.

(7)   Vij, V.; Sultan, S.; Harzandi, A. M.; Meena, A.; Tiwari, J. N.; Lee, W.-G.;
        Yoon, T.; Kim, K. S. Nickel-Based Electrocatalysts for Energy-Related
        Applications: Oxygen Reduction, Oxygen Evolution, and Hydrogen
        Evolution Reactions. *ACS Catal.* **2017**, *7*, 7196–7225.
        https://doi.org/10.1021/acscatal.7b01800.

(8)   Zhao, Q.; Yan, Z.; Chen, C.; Chen, J. Spinels: Controlled Preparation, Oxygen
        Reduction/Evolution Reaction Application, and Beyond. *Chem. Rev.* **2017**,
        117, 10121–10211. https://doi.org/10.1021/acs.chemrev.7b00051.

(9)   Kong, X.; Peng, Z. Low-Dimensional Materials for Alkaline Oxygen
        Evolution Electrocatalysis. *Mater. Today Chem.* **2019**, *11*, 119–132.
        https://doi.org/10.1016/j.mtchem.2018.10.011.

(10)   Lyu, F.; Bai, Y.; Wang, Q.; Wang, L.; Zhang, X.; Yin, Y. Coordination-
        Assisted Synthesis of Iron-Incorporated Cobalt Oxide Nanoplates for
        Enhanced Oxygen Evolution. *Mater. Today Chem.* **2019**, *11*, 112–118.
        https://doi.org/10.1016/j.mtchem.2018.10.010.

(11)   Cetin, A.; Önal, A. M.; Esenturk, E. N. Nanowires Assembled from Iron
        Manganite Nanoparticles: Synthesis, Characterization, and Investigation of
        Electrocatalytic Properties for Water Oxidation Reaction. *J. Mater. Res.* **2019**,
        34, 3231–3239. https://doi.org/10.1557/jmr.2019.215.

(12)   Kocabas, S.; Cetin, A.; Önal, A. M.; Esenturk, E. N. Chromium Substituted
        Iron Oxide Nanowires as Affordable Electrocatalysts for Oxygen Evolution
        Reaction. *J. Nanoparticle Res.* **2019**, *21*, 143. https://doi.org/10.1007/s11051-
        019-4591-5.

(13)   Ekebas, E.; Cetin, A.; Önal, A. M.; Nalbant Esenturk, E. Magnesium
        Substituted Cobalt Spinel Nanostructures for Electrocatalytic
        Water Oxidation. *J. Appl. Electrochem.* **2019**, *49*, 315–325.
        https://doi.org/10.1007/s10800-018-01285-9.

(14)   Cetin, A.; Esenturk, E. N. Hierarchical Nanowire and Nanoplate-Assembled

110

NiCo2O4–NiO Biphasic Microspheres as Effective Electrocatalysts for Oxygen Evolution Reaction. *Mater. Today Chem.* **2019**, *14*, 100215. https://doi.org/10.1016/j.mtchem.2019.100215.

(15) Kim, J.; Yin, X.; Tsao, K.-C.; Fang, S.; Yang, H. $Ca_2Mn_2O_5$ as Oxygen-Deficient Perovskite Electrocatalyst for Oxygen Evolution Reaction. *J. Am. Chem. Soc.* **2014**, *136*, 14646–14649. https://doi.org/10.1021/ja506254g.

(16) Peng, S.; Han, X.; Li, L.; Chou, S.; Ji, D.; Huang, H.; Du, Y.; Liu, J.; Ramakrishna, S. Electronic and Defective Engineering of Electrospun $CaMnO_3$ Nanotubes for Enhanced Oxygen Electrocatalysis in Rechargeable Zinc-Air Batteries. *Adv. Energy Mater.* **2018**, *8*, 1800612. https://doi.org/10.1002/aenm.201800612.

(17) Du, J.; Zhang, T.; Cheng, F.; Chu, W.; Wu, Z.; Chen, J. Nonstoichiometric Perovskite $CaMnO_{3-\delta}$ for Oxygen Electrocatalysis with High Activity. *Inorg. Chem.* **2014**, *53*, 9106–9114. https://doi.org/10.1021/ic501631h.

(18) Jin, C.; Cao, X.; Zhang, L.; Zhang, C.; Yang, R. Preparation and Electrochemical Properties of Urchin-like $La_{0.8}Sr_{0.2}MnO_3$ Perovskite Oxide as a Bifunctional Catalyst for Oxygen Reduction and Oxygen Evolution Reaction. *J. Power Sources* **2013**, *241*, 225–230. https://doi.org/10.1016/j.jpowsour.2013.04.116.

(19) Hua, B.; Li, M.; Luo, J.-L. A Facile Surface Chemistry Approach to Bifunctional Excellence for Perovskite Electrocatalysis. *Nano Energy* **2018**, *49*, 117–125. https://doi.org/10.1016/j.nanoen.2018.04.050.

(20) Xu, Y.; Tsou, A.; Fu, Y.; Wang, J.; Tian, J.-H.; Yang, R. Carbon-Coated Perovskite $BaMnO_3$ Porous Nanorods with Enhanced Electrocatalytic Perporites for Oxygen Reduction and Oxygen Evolution. *Electrochim. Acta* **2015**, *174*, 551–556. https://doi.org/10.1016/j.electacta.2015.05.184.

(21) Yuan, F.; Cheng, X.; Wang, M.; Ni, Y. Controlled Synthesis of Tubular Ferrite MFe_2O_4 (M = Fe, Co, Ni) Microstructures with Efficiently

Electrocatalytic Activity for Water Splitting. *Electrochim. Acta* **2019**, *324*, 134883. https://doi.org/10.1016/j.electacta.2019.134883.

(22) Li, M.; Xiong, Y.; Liu, X.; Bo, X.; Zhang, Y.; Han, C.; Guo, L. Facile Synthesis of Electrospun MFe_2O_4 (M = Co, Ni, Cu, Mn) Spinel Nanofibers with Excellent Electrocatalytic Properties for Oxygen Evolution and Hydrogen Peroxide Reduction. *Nanoscale* **2015**, *7*, 8920–8930. https://doi.org/10.1039/C4NR07243J.

(23) Zhao, W.; Li, X.; Yin, R.; Qian, L.; Huang, X.; Liu, H.; Zhang, J.; Wang, J.; Ding, T.; Guo, Z. Urchin-like $NiO–NiCo_2O_4$ Heterostructure Microsphere Catalysts for Enhanced Rechargeable Non-Aqueous $Li–O_2$ Batteries. *Nanoscale* **2019**, *11*, 50–59. https://doi.org/10.1039/C8NR08457B.

(24) Barauskienė, I.; Valatka, E. Layered Nickel-Cobalt Oxide Coatings on Stainless Steel as an Electrocatalyst for Oxygen Evolution Reaction. *Electrocatalysis* **2019**, *10*, 63–71. https://doi.org/10.1007/s12678-018-0495-x.

(25) Zhao, Y.; Zhou, X.; Ding, Y.; Huang, J.; Zheng, M.; Ye, W. A Study of Photocatalytic, Chemical, and Electrocatalytic Water Oxidation on ACo_2O_4 (A=Ni, Cu, Zn) Samples through Doping Different Metal Ions. *J. Catal.* **2016**, *338*, 30–37. https://doi.org/10.1016/j.jcat.2016.02.003.

(26) Peng, Z.; Jia, D.; Al-Enizi, A. M.; Elzatahry, A. A.; Zheng, G. From Water Oxidation to Reduction: Homologous Ni-Co Based Nanowires as Complementary Water Splitting Electrocatalysts. *Adv. Energy Mater.* **2015**, *5*, 1402031. https://doi.org/10.1002/aenm.201402031.

(27) Yu, X.; Sun, Z.; Yan, Z.; Xiang, B.; Liu, X.; Du, P. Direct Growth of Porous Crystalline $NiCo_2O_4$ Nanowire Arrays on a Conductive Electrode for High-Performance Electrocatalytic Water Oxidation. *J. Mater. Chem. A* **2014**, *2*, 20823–20831. https://doi.org/10.1039/C4TA05315J.

(28) Su, Y.-Z.; Xu, Q.-Z.; Chen, G.-F.; Cheng, H.; Li, N.; Liu, Z.-Q. One

Dimensionally Spinel $NiCo_2O_4$ Nanowire Arrays: Facile Synthesis, Water Oxidation, and Magnetic Properties. *Electrochim. Acta* **2015**, *174*, 1216–1224. https://doi.org/10.1016/j.electacta.2015.06.092.

(29) Mahala, C.; Basu, M. Nanosheets of $NiCo_2O_4$/NiO as Efficient and Stable Electrocatalyst for Oxygen Evolution Reaction. *ACS Omega* **2017**, *2*, 7559–7567. https://doi.org/10.1021/acsomega.7b00957.

(30) Liu, G.; Gao, X.; Wang, K.; He, D.; Li, J. Uniformly Mesoporous $NiO/NiFe_2O_4$ Biphasic Nanorods as Efficient Oxygen Evolving Catalyst for Water Splitting. *Int. J. Hydrogen Energy* **2016**, *41*, 17976–17986. https://doi.org/10.1016/j.ijhydene.2016.07.268.

(31) Liu, G.; Wang, K.; Gao, X.; He, D.; Li, J. Fabrication of Mesoporous $NiFe_2O_4$ Nanorods as Efficient Oxygen Evolution Catalyst for Water Splitting. *Electrochim. Acta* **2016**, *211*, 871–878. https://doi.org/10.1016/j.electacta.2016.06.113.

(32) Ashrit, P. Introduction to Transition Metal Oxides and Thin Films. In *Transition Metal Oxide Thin Film based Chromogenics and Devices*; Elsevier, **2017**; pp 13–72. https://doi.org/10.1016/B978-0-08-101747-0.00002-7.

(33) Kung, H. H. Chapter 2 Bulk and Surface Structure of Transition Metal Oxide. In *Transition Metal Oxides: Surface Chemistry and Catalysis*; **1989**; pp 6–26. https://doi.org/10.1016/S0167-2991(08)60925-8.

(34) Housecroft, C. E.; Sharpe, A. G. *Inorganic Chemistry*, 2nd ed.; Pearson Education Limited, **2005**.

(35) Carrier, X.; Royer, S.; Marceau, E. Synthesis of Metal Oxide Catalysts. In *Metal Oxides in Heterogeneous Catalysis*; Elsevier, **2018**; pp 43–103. https://doi.org/10.1016/B978-0-12-811631-9.00002-8.

(36) Niederberger, M.; Pinna, N. *Metal Oxide Nanoparticles in Organic Solvents*;

Engineering Materials and Processes; Springer London: London, **2009**. https://doi.org/10.1007/978-1-84882-671-7.

(37) *Nanocatalysis Synthesis and Applications*; Polshettiwar, V., Asefa, T., Eds.; John Wiley & Sons, Inc.: Hoboken, NJ, USA, **2013**. https://doi.org/10.1002/9781118609811.

(38) Kim, D.-W.; Rhee, K.-Y.; Park, S.-J. Synthesis of Activated Carbon Nanotube/Copper Oxide Composites and Their Electrochemical Performance. *J. Alloys Compd.* **2012**, *530*, 6–10. https://doi.org/10.1016/j.jallcom.2012.02.157.

(39) Schlögl, R. The Role of Chemistry in the Energy Challenge. *ChemSusChem* **2010**, *3*, 209–222. https://doi.org/10.1002/cssc.200900183.

(40) Balzani, V.; Credi, A.; Venturi, M. Photochemical Conversion of Solar Energy. *ChemSusChem* **2008**, *1*, 26–58. https://doi.org/10.1002/cssc.200700087.

(41) Kuznetsov, V. L.; Edwards, P. P. Functional Materials for Sustainable Energy Technologies: Four Case Studies. *ChemSusChem* **2010**, *3*, 44–58. https://doi.org/10.1002/cssc.200900190.

(42) Inoue, H.; Shimada, T.; Kou, Y.; Nabetani, Y.; Masui, D.; Takagi, S.; Tachibana, H. The Water Oxidation Bottleneck in Artificial Photosynthesis: How Can We Get Through It? An Alternative Route Involving a Two-Electron Process. *ChemSusChem* **2011**, *397*, 173-179. https://doi.org/10.1002/cssc.201000385.

(43) Lubitz, W.; Reijerse, E. J.; Messinger, J. Solar Water-Splitting into H2 and O2: Design Principles of Photosystem II and Hydrogenases. *Energy Environ. Sci.* **2008**, *1*, 15-31. https://doi.org/10.1039/b808792j.

(44) Lewis, N. S.; Nocera, D. G. Powering the Planet: Chemical Challenges in Solar Energy Utilization. *Proc. Natl. Acad. Sci.* **2006**, *103*, 15729–15735.

https://doi.org/10.1073/pnas.0603395103.

(45)   Faunce, T.; Styring, S.; Wasielewski, M. R.; Brudvig, G. W.; Rutherford, A. W.; Messinger, J.; Lee, A. F.; Hill, C. L.; DeGroot, H.; Fontecave, M.; et al. Artificial Photosynthesis as a Frontier Technology for Energy Sustainability. *Energy Environ. Sci.* **2013**, *6*, 1074-1076. https://doi.org/10.1039/c3ee40534f.

(46)   Singh, A.; Spiccia, L. Water Oxidation Catalysts Based on Abundant 1st Row Transition Metals. *Coord. Chem. Rev.* **2013**, *257*, 2607–2622. https://doi.org/10.1016/j.ccr.2013.02.027.

(47)   Bofill, R.; García-Antón, J.; Escriche, L.; Sala, X. Chemical, Electrochemical and Photochemical Molecular Water Oxidation Catalysts. *J. Photochem. Photobiol. B Biol.* **2015**, *152*, 71–81. https://doi.org/10.1016/j.jphotobiol.2014.10.022.

(48)   Maeda, K. Photocatalytic Water Splitting Using Semiconductor Particles: History and Recent Developments. *J. Photochem. Photobiol. C Photochem. Rev.* **2011**, *12*, 237–268. https://doi.org/10.1016/j.jphotochemrev.2011.07.001.

(49)   Parent, A. R.; Sakai, K. Progress in Base-Metal Water Oxidation Catalysis. *ChemSusChem* **2014**, *7*, 2070–2080. https://doi.org/10.1002/cssc.201402322.

(50)   Demir, E.; Akbayrak, S.; Önal, A. M.; Özkar, S. Nanoceria-Supported Ruthenium(0) Nanoparticles: Highly Active and Stable Catalysts for Hydrogen Evolution from Water. *ACS Appl. Mater. Interfaces* **2018**, *10*, 6299–6308. https://doi.org/10.1021/acsami.7b17469.

(51)   Hosseini, S. G.; Abazari, R.; Gavi, A. Pure $CuCr_2O_4$ Nanoparticles: Synthesis, Characterization and Their Morphological and Size Effects on the Catalytic Thermal Decomposition of Ammonium Perchlorate. *Solid State Sci.* **2014**, *37*, 72–79. https://doi.org/10.1016/j.solidstatesciences.2014.08.014.

(52) Hwang, B. J.; Santhanam, R.; Liu, D. G. Characterization of Nanoparticles of LiMn$_2$O$_4$ Synthesized by Citric Acid Sol–Gel Method. *J. Power Sources* **2001**, *97–98*, 443–446. https://doi.org/10.1016/S0378-7753(01)00635-8.

(53) Xu, J.; Wang, L.; Zhang, J.; Qian, J.; Liu, J.; Zhang, Z.; Zhang, H.; Liu, X. Fabrication of Porous Double-Urchin-like MgCo$_2$O$_4$ Hierarchical Architectures for High-Rate Supercapacitors. *J. Alloys Compd.* **2016**, *688*, 933–938. https://doi.org/10.1016/j.jallcom.2016.07.250.

(54) Kuo, C.-H.; Mosa, I. M.; Poyraz, A. S.; Biswas, S.; El-Sawy, A. M.; Song, W.; Luo, Z.; Chen, S.-Y.; Rusling, J. F.; He, J.; et al. Robust Mesoporous Manganese Oxide Catalysts for Water Oxidation. *ACS Catal.* **2015**, *5*, 1693–1699. https://doi.org/10.1021/cs501739e.

(55) Lee, S. Y.; González-Flores, D.; Ohms, J.; Trost, T.; Dau, H.; Zaharieva, I.; Kurz, P. Screen-Printed Calcium-Birnessite Electrodes for Water Oxidation at Neutral PH and an "Electrochemical Harriman Series." *ChemSusChem* **2014**, *7*, 3442–3451. https://doi.org/10.1002/cssc.201402533.

(56) Chen, Z.; Zhao, B.; He, Y.-C.; Wen, H.-R.; Fu, X.-Z.; Sun, R.; Wong, C.-P. NiCo$_2$O$_4$ Nanoframes with a Nanosheet Surface as Efficient Electrocatalysts for the Oxygen Evolution Reaction. *Mater. Chem. Front.* **2018**, *2*, 1155–1164. https://doi.org/10.1039/C8QM00027A.

(57) Cui, B.; Lin, H.; Li, J.-B.; Li, X.; Yang, J.; Tao, J. Core-Ring Structured NiCo$_2$O$_4$ Nanoplatelets: Synthesis, Characterization, and Electrocatalytic Applications. *Adv. Funct. Mater.* **2008**, *18*, 1440–1447. https://doi.org/10.1002/adfm.200700982.

(58) Acharyya, S. S.; Ghosh, S.; Bal, R. Catalytic Oxidation of Aniline to Azoxybenzene Over CuCr$_2$O$_4$ Spinel Nanoparticle Catalyst. *ACS Sustain. Chem. Eng.* **2014**, *2*, 584–589. https://doi.org/10.1021/sc5000545.

(59) Chen, Z.; Tang, B.; Shen, J.; Chen, Q.; He, G.; Chen, H. Synthesis of CuCr$_2$O$_4$/Reduced Graphene Oxide Composite: A Green Catalyst for

Selective Oxidation of Cyclohexane to Cyclohexanone with Hydrogen Peroxide. *ChemistrySelect* **2017**, *2*, 10941–10945. https://doi.org/10.1002/slct.201702318.

(60)   Acharyya, S. S.; Ghosh, S.; Tiwari, R.; Pendem, C.; Sasaki, T.; Bal, R. Synergistic Effect between Ultrasmall Cu(II) Oxide and $CuCr_2O_4$ Spinel Nanoparticles in Selective Hydroxylation of Benzene to Phenol with Air as Oxidant. *ACS Catal.* **2015**, *5*, 2850–2858. https://doi.org/10.1021/cs5020699.

(61)   Xu, S.; Dong, D.; Wang, Y.; Doherty, W.; Xie, K.; Wu, Y. Perovskite Chromates Cathode with Resolved and Anchored Nickel Nano-Particles for Direct High-Temperature Steam Electrolysis. *J. Power Sources* **2014**, *246*, 346–355. https://doi.org/10.1016/j.jpowsour.2013.07.082.

(62)   Yao, W.; Duan, T.; Li, Y.; Yang, L.; Xie, K. Perovskite Chromate Doped with Titanium for Direct Carbon Dioxide Electrolysis. *New J. Chem.* **2015**, *39*, 2956–2965. https://doi.org/10.1039/C4NJ01868K.

(63)   Jiménez, V. M.; Fernández, A.; Espinós, J. P.; González-Elipe, A. R. The State of the Oxygen at the Surface of Polycrystalline Cobalt Oxide. *J. Electron Spectros. Relat. Phenomena* **1995**, *71*, 61–71. https://doi.org/10.1016/0368-2048(94)02238-0.

(64)   Al-Mamun, M.; Su, X.; Zhang, H.; Yin, H.; Liu, P.; Yang, H.; Wang, D.; Tang, Z.; Wang, Y.; Zhao, H. Strongly Coupled $CoCr_2O_4$/Carbon Nanosheets as High Performance Electrocatalysts for Oxygen Evolution Reaction. *Small* **2016**, *12*, 2866–2871. https://doi.org/10.1002/smll.201600549.

(65)   Lobo, L. S.; Rubankumar, A. Investigation on Structural and Electrical Properties of $FeMnO_3$ Synthesized by Sol-Gel Method. *Ionics (Kiel).* **2019**, *25*, 1341–1350. https://doi.org/10.1007/s11581-018-2776-z.

(66)   Ding, J.; Zhong, Q.; Zhang, S. Simultaneous Removal of NO_X and SO_2 with H_2O_2 over Fe Based Catalysts at Low Temperature. *RSC Adv.* **2014**, *4*, 5394. https://doi.org/10.1039/c3ra46418k.

(67) Pham, M.-H.; Dinh, C.-T.; Vuong, G.-T.; Ta, N.-D.; Do, T.-O. Visible Light Induced Hydrogen Generation Using a Hollow Photocatalyst with Two Cocatalysts Separated on Two Surface Sides. *Phys. Chem. Chem. Phys.* **2014**, *16*, 5937. https://doi.org/10.1039/c3cp54629b.

(68) Tang, Q.; Jiang, L.; Liu, J.; Wang, S.; Sun, G. Effect of Surface Manganese Valence of Manganese Oxides on the Activity of the Oxygen Reduction Reaction in Alkaline Media. *ACS Catal.* **2014**, *4*, 457–463. https://doi.org/10.1021/cs400938s.

(69) Nagamuthu, S.; Vijayakumar, S.; Lee, S.-H.; Ryu, K.-S. Hybrid Supercapacitor Devices Based on $MnCo_2O_4$ as the Positive Electrode and $FeMn_2O_4$ as the Negative Electrode. *Appl. Surf. Sci.* **2016**, *390*, 202–208. https://doi.org/10.1016/j.apsusc.2016.08.072.

(70) Pyeon, M.; Ruoko, T.-P.; Leduc, J.; Gönüllü, Y.; Deo, M.; Tkachenko, N. V.; Mathur, S. Critical Role and Modification of Surface States in Hematite Films for Enhancing Oxygen Evolution Activity. *J. Mater. Res.* **2018**, *33*, 455–466. https://doi.org/10.1557/jmr.2017.465.

(71) Zhang, G.; Li, Y.; Zhou, Y.; Yang, F. NiFe Layered-Double-Hydroxide-Derived $NiO-NiFe_2O_4$/Reduced Graphene Oxide Architectures for Enhanced Electrocatalysis of Alkaline Water Splitting. *ChemElectroChem* **2016**, *3*, 1927–1936. https://doi.org/10.1002/celc.201600301.

(72) Zhao, X.; Xu, S.; Wang, L.; Duan, X.; Zhang, F. Exchange-Biased $NiFe_2O_4$/NiO Nanocomposites Derived from NiFe-Layered Double Hydroxides as a Single Precursor. *Nano Res.* **2010**, *3*, 200–210. https://doi.org/10.1007/s12274-010-1023-3.

(73) Zhang, B. B.; Xu, J. C.; Wang, P. F.; Han, Y. B.; Hong, B.; Jin, H. X.; Jin, D. F.; Peng, X. L.; Li, J.; Gong, J.; et al. Ordered $NiO/NiFe_2O_4$ Nanocomposites: Synthesis, Exchange Bias and Magnetic Properties. *J. Alloys Compd.* **2016**, *662*, 348–354. https://doi.org/10.1016/j.jallcom.2015.12.079.

(74) Lee, J. M.; Gu, T. H.; Kwon, N. H.; Oh, S. M.; Hwang, S.-J. Rapid Synthetic Route to Nanocrystalline Carbon-Mixed Metal Oxide Nanocomposites with Enhanced Electrode Functionality. *J. Phys. Chem. C* **2016**, *120*, 8451–8460. https://doi.org/10.1021/acs.jpcc.6b00841.

(75) Liu, Q.; Jin, J.; Zhang, J. $NiCo_2S_4$@graphene as a Bifunctional Electrocatalyst for Oxygen Reduction and Evolution Reactions. *ACS Appl. Mater. Interfaces* **2013**, *5*, 5002–5008. https://doi.org/10.1021/am4007897.

(76) Kang, B. K.; Woo, M. H.; Lee, J.; Song, Y. H.; Wang, Z.; Guo, Y.; Yamauchi, Y.; Kim, J. H.; Lim, B.; Yoon, D. H. Mesoporous Ni–Fe Oxide Multi-Composite Hollow Nanocages for Efficient Electrocatalytic Water Oxidation Reactions. *J. Mater. Chem. A* **2017**, *5*, 4320–4324. https://doi.org/10.1039/C6TA10094E.

(77) Wang, Y.; Pan, D.; Zhang, M.; Ma, T.; Liu, H.; Yan, Z.; Xie, J. Construction of Three-Dimensional Nitrogen-Doped Graphene Coated with Uniform Nickel Oxide/Nickel Ferrite Nanoparticles with Enhanced Electrochemical Properties for Supercapacitors. *J. Alloys Compd.* **2018**, *765*, 480–488. https://doi.org/10.1016/j.jallcom.2018.06.222.

(78) Yan, W.; Cao, X.; Tian, J.; Jin, C.; Ke, K.; Yang, R. Nitrogen/Sulfur Dual-Doped 3D Reduced Graphene Oxide Networks-Supported $CoFe_2O_4$ with Enhanced Electrocatalytic Activities for Oxygen Reduction and Evolution Reactions. *Carbon N. Y.* **2016**, *99*, 195–202. https://doi.org/10.1016/j.carbon.2015.12.011.

(79) Long, X.; Li, J.; Xiao, S.; Yan, K.; Wang, Z.; Chen, H.; Yang, S. A Strongly Coupled Graphene and FeNi Double Hydroxide Hybrid as an Excellent Electrocatalyst for the Oxygen Evolution Reaction. *Angew. Chemie Int. Ed.* **2014**, *53*, 7584–7588. https://doi.org/10.1002/anie.201402822.

(80) Wang, Y.; Wu, S.; Wang, C.; Wang, Y.; Han, X. Morphology Controllable Synthesis of $NiO/NiFe_2O_4$ Hetero-Structures for Ultrafast

Lithium-Ion   Battery.   *Front.   Chem.*   **2019**,   *6,   654*.
https://doi.org/10.3389/fchem.2018.00654.

(81)   Shao, M.; Ning, F.; Zhao, Y.; Zhao, J.; Wei, M.; Evans, D. G.; Duan, X. Core–
Shell Layered Double Hydroxide Microspheres with Tunable Interior
Architecture for Supercapacitors. *Chem. Mater.* **2012**, *24*, 1192–1197.
https://doi.org/10.1021/cm203831p.

(82)   Xu, K.; Yang, J.; Hu, J. Synthesis of Hollow NiCo$_2$O$_4$ Nanospheres with
Large Specific Surface Area for Asymmetric Supercapacitors. *J. Colloid
Interface Sci.* **2018**, *511*, 456–462. https://doi.org/10.1016/j.jcis.2017.09.113.

(83)   Wang, L.; Gu, C.; Ge, X.; Zhang, J.; Zhu, H.; Tu, J. Highly Efficient
Bifunctional Catalyst of NiCo$_2$O$_4$@NiO@Ni Core/Shell Nanocone Array for
Stable Overall Water Splitting. *Part. Part. Syst. Charact.* **2017**, *34*, 1700228.
https://doi.org/10.1002/ppsc.201700228.

(84)   Chen, R.; Wang, H.-Y.; Miao, J.; Yang, H.; Liu, B. A Flexible High-
Performance Oxygen Evolution Electrode with Three-Dimensional
NiCo$_2$O$_4$ Core-Shell Nanowires. *Nano Energy* **2015**, *11*, 333–340.
https://doi.org/10.1016/j.nanoen.2014.11.021.

(85)   Chang, C.; Zhang, L.; Hsu, C.-W.; Chuah, X.-F.; Lu, S.-Y. Mixed
NiO/NiCo$_2$O$_4$ Nanocrystals Grown from the Skeleton of a 3D Porous Nickel
Network as Efficient Electrocatalysts for Oxygen Evolution Reactions.
ACS   Appl.   Mater.   Interfaces   **2018**,   *10*,   417–426.
https://doi.org/10.1021/acsami.7b13127.

(86)   Wang, Y.; Zhang, Z.; Liu, X.; Ding, F.; Zou, P.; Wang, X.; Zhao, Q.; Rao, H.
MOF-Derived NiO/NiCo$_2$O$_4$ and NiO/NiCo$_2$O$_4$-RGO as Highly Efficient and
Stable Electrocatalysts for Oxygen Evolution Reaction.
ACS   Sustain.   Chem.   Eng.   **2018**,   *6*,   12511–12521.
https://doi.org/10.1021/acssuschemeng.8b03221.

(87)   Li, Z.; Lv, L.; Wang, J.; Ao, X.; Ruan, Y.; Zha, D.; Hong, G.; Wu, Q.; Lan,

Y.; Wang, C.; et al. Engineering Phosphorus-Doped LaFeO$_{3-\delta}$ Perovskite Oxide as Robust Bifunctional Oxygen Electrocatalysts in Alkaline Solutions. *Nano Energy* **2018**, *47*, 199–209. https://doi.org/10.1016/j.nanoen.2018.02.051.

(88) Xie, Z.; Zhang, C.; He, X.; Liang, Y.; Meng, D.; Wang, J.; Liang, P.; Zhang, Z. Iron and Nickel Mixed Oxides Derived From NiIIIFeII-PBA for Oxygen Evolution Electrocatalysis. *Front. Chem.* **2019**, *7*. https://doi.org/10.3389/fchem.2019.00539.

(89) Kötz, R. XPS Studies of Oxygen Evolution on Ru and RuO$_2$ Anodes. *J. Electrochem. Soc.* **1983**, *130*, 825. https://doi.org/10.1149/1.2119829.

(90) Li, P.; Ma, R.; Zhou, Y.; Chen, Y.; Liu, Q.; Peng, G.; Liang, Z.; Wang, J. Spinel Nickel Ferrite Nanoparticles Strongly Cross-Linked with Multiwalled Carbon Nanotubes as a Bi-Efficient Electrocatalyst for Oxygen Reduction and Oxygen Evolution. *RSC Adv.* **2015**, *5*, 73834–73841. https://doi.org/10.1039/C5RA14713A.

(91) Xu, Y.; Yan, Y.; He, T.; Zhan, K.; Yang, J.; Zhao, B.; Qi, K.; Xia, B. Y. Supercritical CO$_2$-Assisted Synthesis of NiFe$_2$O$_4$/Vertically-Aligned Carbon Nanotube Arrays Hybrid as a Bifunctional Electrocatalyst for Efficient Overall Water Splitting. *Carbon N. Y.* **2019**, *145*, 201–208. https://doi.org/10.1016/j.carbon.2019.01.011.

(92) Xia, W.-Y.; Li, N.; Li, Q.-Y.; Ye, K.-H.; Xu, C.-W. Au-NiCo$_2$O$_4$ Supported on Three-Dimensional Hierarchical Porous Graphene-like Material for Highly Effective Oxygen Evolution Reaction. *Sci. Rep.* **2016**, *6*, 23398. https://doi.org/10.1038/srep23398.

(93) Bao, J.; Zhang, X.; Fan, B.; Zhang, J.; Zhou, M.; Yang, W.; Hu, X.; Wang, H.; Pan, B.; Xie, Y. Ultrathin Spinel-Structured Nanosheets Rich in Oxygen Deficiencies for Enhanced Electrocatalytic Water Oxidation. *Angew. Chemie Int. Ed.* **2015**, *54*, 7399–7404. https://doi.org/10.1002/anie.201502226.

(94)   Cheng, F.; Zhang, T.; Zhang, Y.; Du, J.; Han, X.; Chen, J. Enhancing Electrocatalytic Oxygen Reduction on MnO_2 with Vacancies. *Angew. Chemie Int. Ed.* **2013**, *52*, 2474–2477. https://doi.org/10.1002/anie.201208582.

(95)   Pal, S.; Azad, U. P.; Singh, A. K.; Kumar, D.; Prakash, R. Electrochimica Acta Studies on Some Spinel Oxides Based Electrocatalysts for Oxygen Evolution and Capacitive Applications. *Electrochim. Acta* **2019**, *320*, 134584. https://doi.org/10.1016/j.electacta.2019.134584.

(96)   Dutta, A.; Pradhan, N. Developments of Metal Phosphides as Efficient OER Precatalysts. *J. Phys. Chem. Lett.* **2017**, *8*, 144–152. https://doi.org/10.1021/acs.jpclett.6b02249.

(97)   Gardner, G.; Al-Sharab, J.; Danilovic, N.; Go, Y. B.; Ayers, K.; Greenblatt, M.; Charles Dismukes, G. Structural Basis for Differing Electrocatalytic Water Oxidation by the Cubic, Layered and Spinel Forms of Lithium Cobalt Oxides. *Energy Environ. Sci.* **2016**, *9*, 184–192. https://doi.org/10.1039/C5EE02195B.

(98)   Yang, Y.; Lun, Z.; Xia, G.; Zheng, F.; He, M.; Chen, Q. Non-Precious Alloy Encapsulated in Nitrogen-Doped Graphene Layers Derived from MOFs as an Active and Durable Hydrogen Evolution Reaction Catalyst. *Energy Environ. Sci* **2015**, *8*, 3563. https://doi.org/10.1039/c5ee02460a.

(99)   Liang, Y.; Wang, H.; Zhou, J.; Li, Y.; Wang, J.; Regier, T.; Dai, H. Covalent Hybrid of Spinel Manganese–Cobalt Oxide and Graphene as Advanced Oxygen Reduction Electrocatalysts. *J. Am. Chem. Soc.* **2012**, *134*, 3517–3523. https://doi.org/10.1021/ja210924t.

A. N₂ adsorption – desorption isotherms of synthesized materials
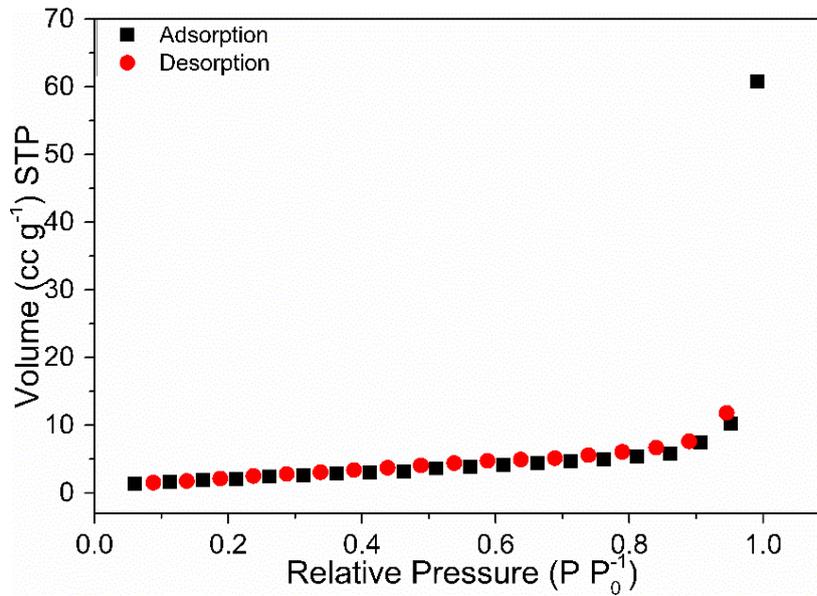
Figure A.1. N₂ adsorption – desorption isotherm of CuCr₂O₄ nanoparticles
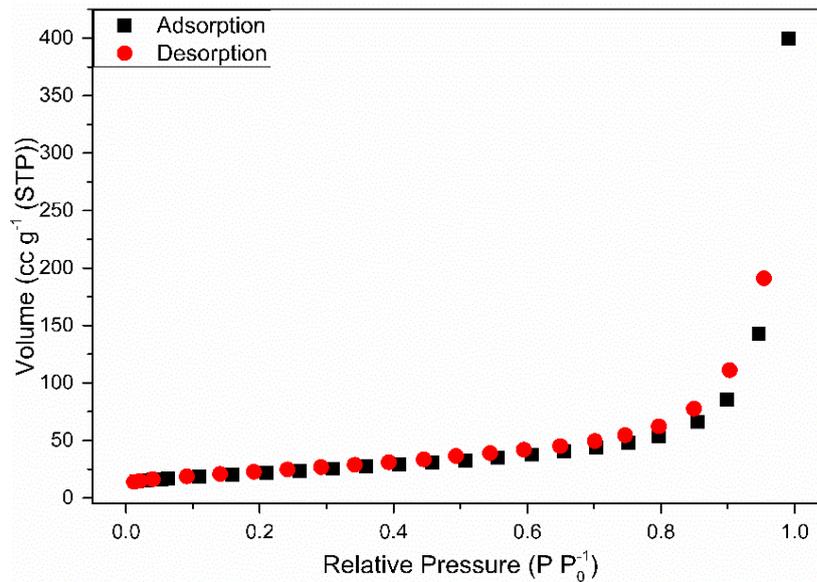
Figure A.2. N₂ adsorption – desorption isotherm of NiFe₂O₄-NiO nanoparticles
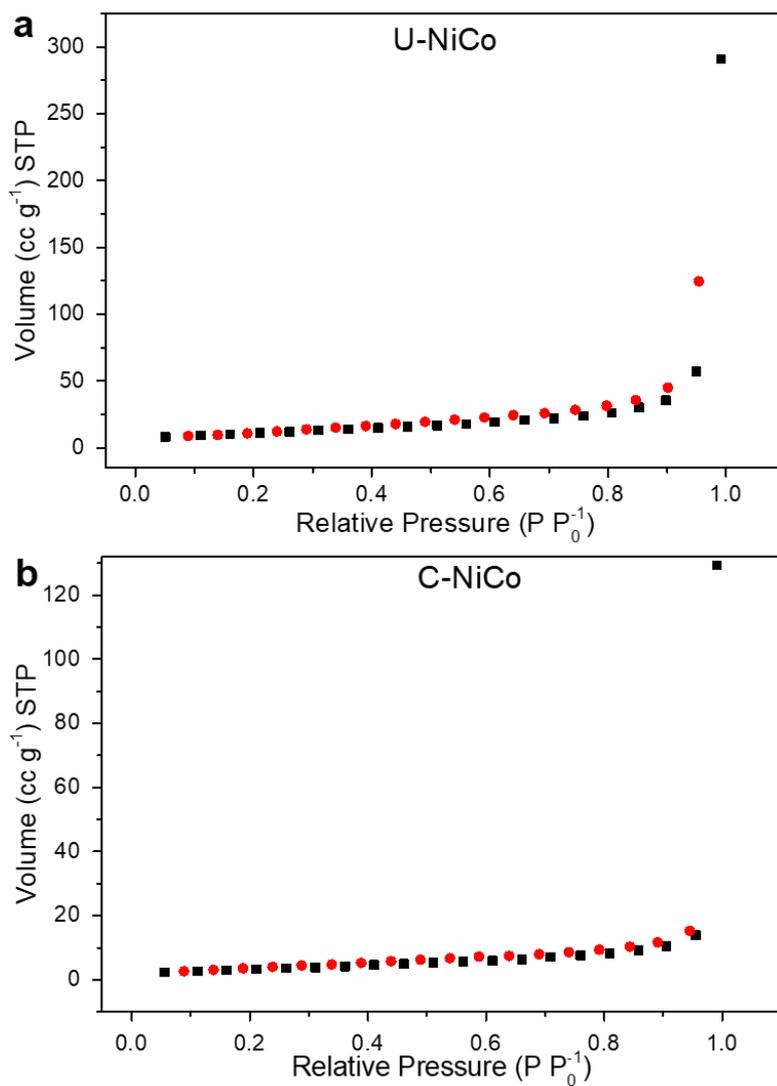
Figure A.3. N$_2$ adsorption – desorption isotherms of (a) U-NiCo and (b) C-NiCo microspheres

B. Electrochemical Activity of $CuCr_2O_4$ Nanoparticles for Water Oxidation in Sodium Borate Buffer Solution

Electrode Preparation

Electrodes modified with $CuCr_2O_4$ Nanoparticles were prepared by a method reported by Kuo et al.[54] Briefly, 4.0 mg of catalyst was dispersed in 1.0 mL ethanol and 1.0 mL deionized water mixture. After ultrasonication, Nafion was added and sonicated for 20 min. 7.5 µL of solution was dropped onto GC electrodes and dried in oven (90 °C). The effect of carbon materials (Printex L6 (PL6), Super C65, multiwalled carbon nanotube (MWCNT)) addition into catalyst solution as well as effect of carbon and Nafion® amount on onset potential and current density were also investigated and the electrodes were prepared by the same recipe.

Electrochemical Measurements

All electrochemical measurements were performed at room temperature with Gamry PCI4/300 potentiostat-galvanostat. GC electrode modified with $CuCr_2O_4$ Nanoparticles were used as working electrode in a standard three-electrode configuration with Pt wire as cathode and Ag/AgCl as reference electrode. LSV of GC electrode modified with $CuCr_2O_4$ Nanoparticles were obtained by scanning the potential from $0 – 1.2$ V (vs Ag/AgCl) with a scan rate of 10 mV s^{-1} in 0.1 M sodium borate buffer (pH: 9.2).

Effect of Nafion® amount on onset potential

Effect of Nafion® amount on onset potential was investigated in order to determine the optimum value. Figure B.1 demonstrates the polarization curves obtained from electrodes prepared by different amount of Nafion® (i.e. 9.5 µL, 19.0 µL and 38.0 µL) to the catalyst mixture. Comparison of the curves revealed that addition of 38.0 µL of Nafion® resulted in higher onset potential and lower current density values. The most likely reason for this observation is that high amount of polymer solution may have blocked the electrode surface, and thus limited the electron transfer.

Among the other two electrodes, the electrode with 9.5 μL of Nafion® exhibited slightly higher onset potential and lower current density compared to the one with 19.0 μL Nafion®. Therefore, 19.0 μL Nafion® was used in the preparation of electrodes in the following electrochemical measurements.
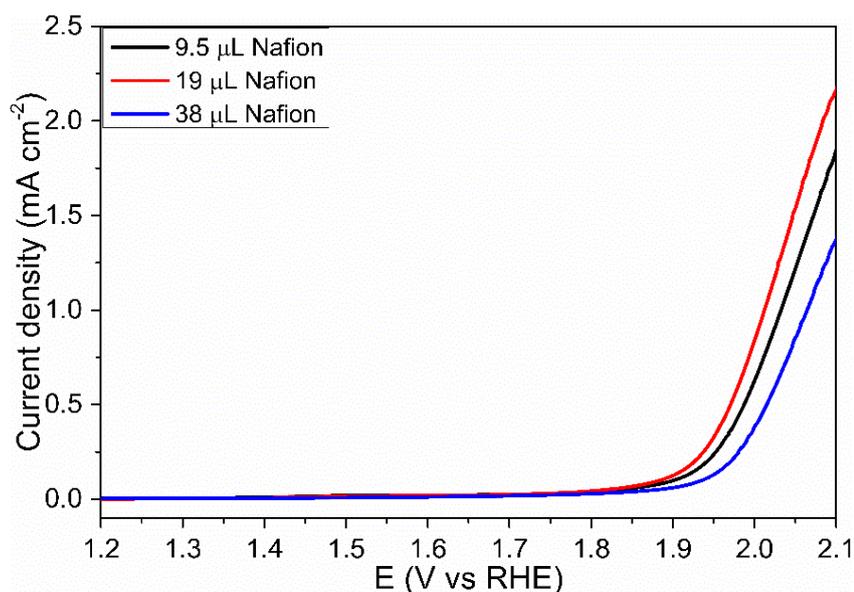
Figure B.1. Polarization curves of $CuCr_2O_4$ nanoparticles with different amount of Nafion® in 0.1 M KOH at a scan rate of 5 mV s^{-1}

Effect of Carbon Materials on onset potential

Previously reported studies have shown that adding carbon to the solution from which the electrodes were prepared have increased the current passing the electrode, and thus prepared electrodes by mixing carbon and catalyst in deionized water/ethanol mixture.[5,54,97–99] Therefore, in this study too, the effect of carbon presence was investigated.

Figure B.2a shows the polarization curves of $CuCr_2O_4$ Nanoparticles along with the one mixed with carbon (PL6) and bare GCE. Modified electrodes exhibited lower onset potentials compare to bare GC electrode as expected. No significant change

126

was observed for onset potentials upon addition of PL6 while a slight increase in current density was noted. However, adding carbon to the catalyst mixture appears to have no significant effect on water oxidation activity. The effect of only carbon on onset potential was also investigated (Figure B.2b). Carbon material has no effect on neither onset potential nor current density, as expected. As a result, the decrease in onset potential in $CuCr_2O_4$-GC electrodes are attributed to presence of the nanoparticles.
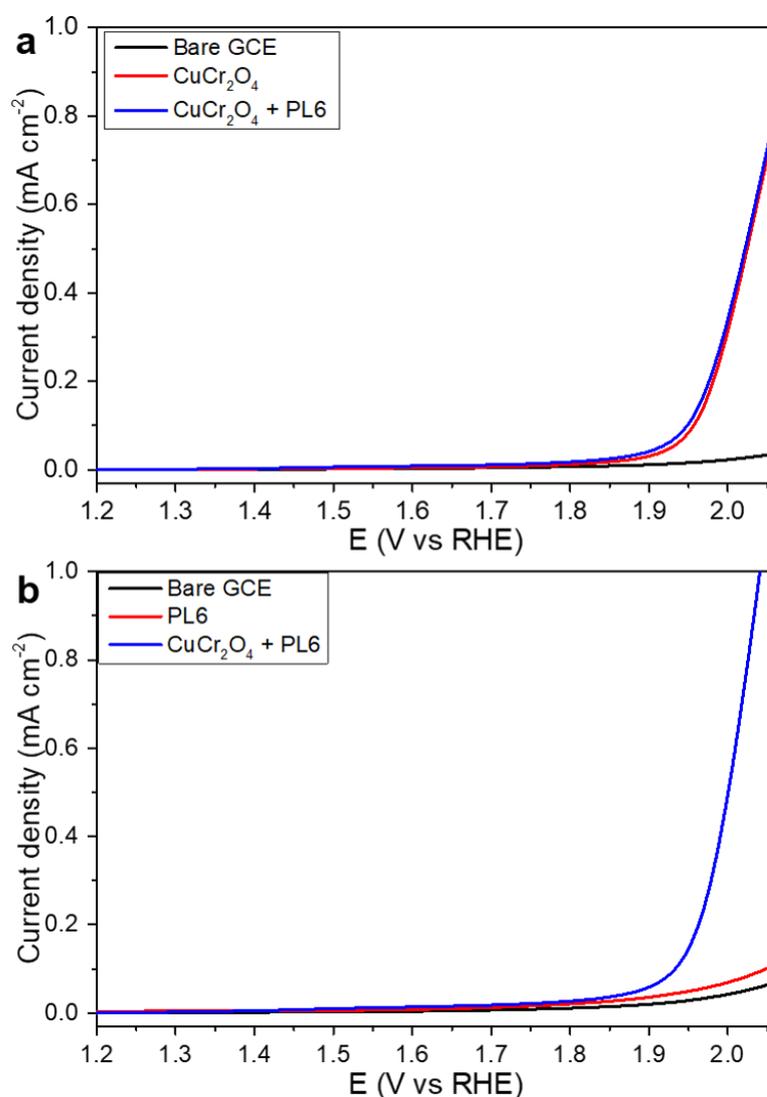
Figure B.2. Polarization curves of bare GCE, $CuCr_2O_4$ nanoparticles and $CuCr_2O_4$ nanoparticles mixed with PL6 in 0.1 M KOH at a scan rate of 5 mV s^{-1}

Figure B.3a shows the polarization curves of electrodes prepared by different carbon loading (w/w % relative to amount of catalyst). Very slight differences in onset potentials were recorded with different carbon loadings. The most significant change in both onset potential and current density was noted for the electrode with 10% carbon. Therefore, 10% carbon loading used for the following measurements. Electrodes were also prepared by using Super C65 carbon instead of PL6. The resulting polarization curves are given in Figure B.3b. Inspection of the curves reveal that the type of carbon material used has no significant effect neither on onset potential or current density.
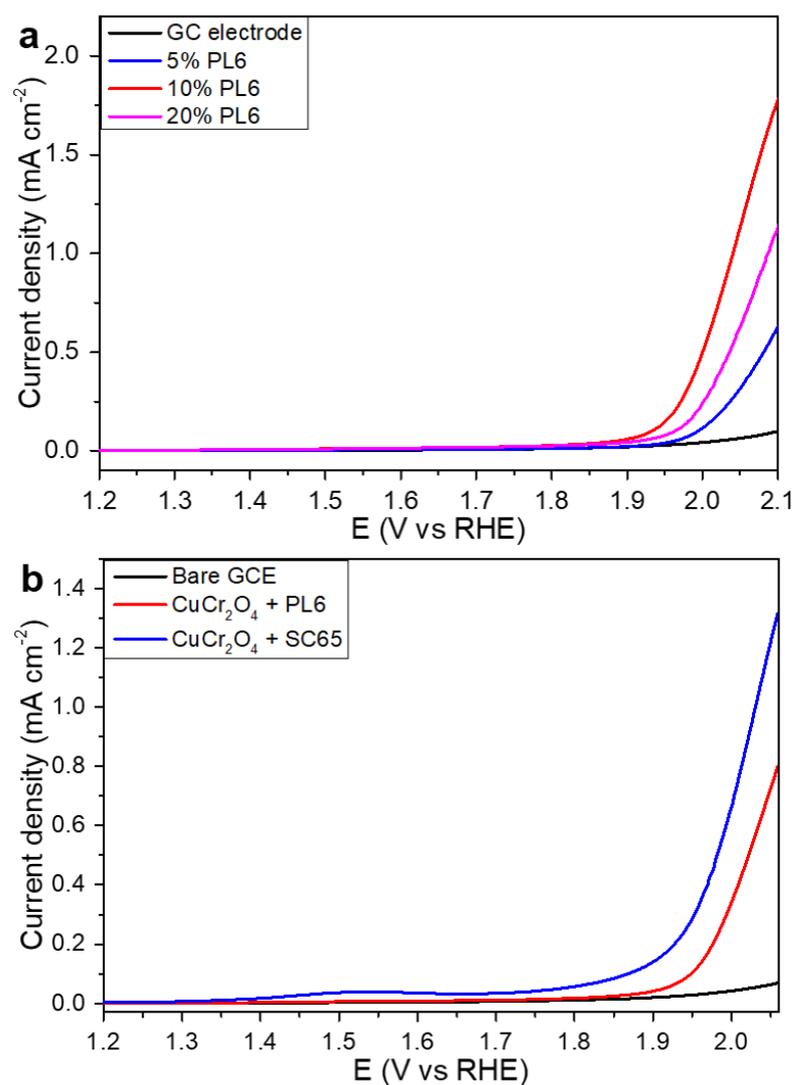
Figure B.3. Polarization curves of $CuCr_2O_4$ nanoparticles obtained with (a) different carbon loadings and (b) different carbon materials in 0.1 M KOH at a scan rate of 5 mV s^{-1}

During these studies it was observed that modified GC electrodes were not as stable and Nanoparticles were detaching from the electrode surface. Therefore, GC electrodes were modified by the method described in Section 4.4.1. In addition to previous studies, the effect of MWCNT on onset potential was also tested. Polarization curves of $CuCr_2O_4$ nanoparticles along with the one mixed with carbon

(PL6 and MWCNT) and bare GC electrode are given in Figure B.4. As observed from the curves, addition of carbon to the catalyst solution has no effect on onset potential and current density, and thus electrocatalytic activity of the Nanoparticles toward water oxidation reaction. Moreover, maximum current density value the catalyst could generate was 1.2 mA cm^{-2} with the use of sodium borate solution, as explained in Section 3.1.2. Therefore, 0.1 M KOH solution was used in the investigation of electrochemical activities of nanomaterials for water oxidation reaction. The data obtained for $CuCr_2O_4$ Nanoparticles in sodium borate solution is summarized in Table B1.
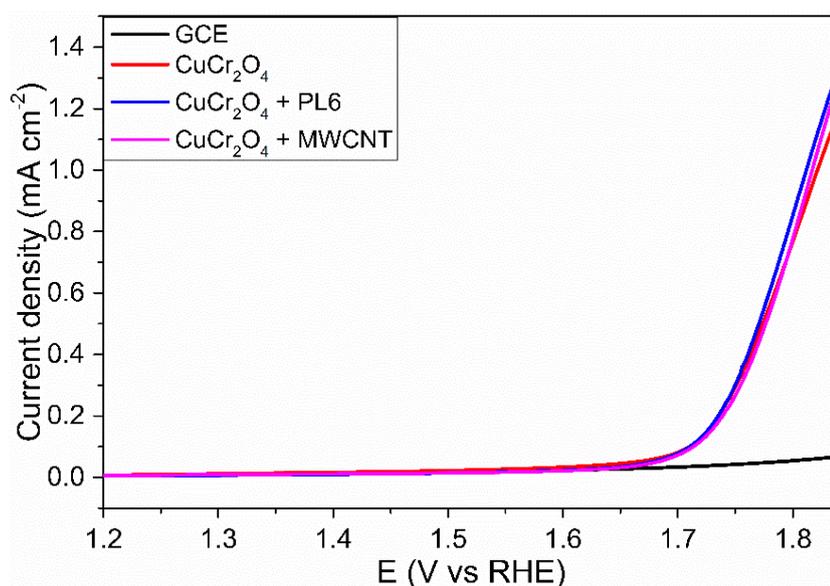
Figure B.4. Polarization curves of $CuCr_2O_4$ nanoparticles and $CuCr_2O_4$ nanoparticles mixed with PL6 and MWCNT in 0.1 M KOH at a scan rate of 5 mV s^{-1}

Table B.1 Summary of the data obtained for $CuCr_2O_4$ nanoparticles in sodium borate buffer solution

Electrode		Onset (V) (RHE)	Max j (mA cm^{-2}) at η:830 mV
Nafion®	9.5 μL	1.9	1.35
	19.0 μL	1.89	1.68
	38.0 μL	1.96	0.95
CuCr₂O₄		1.95	0.776
CuCr₂O₄ + PL6	5 %	1.98	0.37
	10 %	1.94	1.27
	20 %	1.96	0.72
CuCr₂O₄ + SC65	10 %	1.9	1.32
CuCr₂O₄ + MWCNT	10 %	1.92	1.3

C. EIS fitting data of the synthesized nanomaterials

Table C.1 EIS data of FeMnO$_3$ nanowires

Potential (mV vs Ag wire)	R$_u$ (Ω cm^{-2})	R$_p$ (Ω cm^{-2})	Y$_0$
680	28.4	380	388.5 x 10^{-6}
700	29.8	150.7	386.3 x 10^{-6}
720	29.0	70.7	408.2 x 10^{-6}
740	28.4	44.8	454.2 x 10^{-6}
760	28.0	32.7	483.4 x 10^{-6}
780	27.8	26.8	486.4 x 10^{-6}

Table C.2 EIS data of NiFe$_2$O$_4$-NiO nanoparticles

Potential (mV vs Ag/AgCl)	R$_u$ (Ω cm^{-2})	R$_p$ (Ω cm^{-2})	Y$_0$
560	8.8	949.7	3.0 x 10^{-3}
580	9.4	251.4	2.8 x 10^{-3}
600	8.4	122.6	2.7 x 10^{-3}
620	7.2	58.1	2.6 x 10^{-3}
640	7.2	33.0	2.4 x 10^{-3}
660	5.5	22.5	2.8 x 10^{-3}
680	5.0	13.4	2.2 x 10^{-3}

Table C.3 EIS data of C-NiCo microspheres

Potential (mV vs Ag/AgCl)	R_u (Ω cm^{-2})	R_p (Ω cm^{-2})	Y_0
580	5.0	141.8	2.5×10^{-3}
600	5.0	61.1	2.3×10^{-3}
620	5.0	32.3	2.3×10^{-3}
640	5.2	18.8	2.3×10^{-3}
660	5.2	9.5	2.5×10^{-3}
680	5.2	7.1	2.4×10^{-3}
700	5.2	5.6	2.3×10^{-3}

Table C.4 EIS data of U-NiCo microspheres

Potential (mV vs Ag/AgCl)	R_u (Ω cm^{-2})	R_p (Ω cm^{-2})	Y_0
560	5.4	448.6	12.2×10^{-3}
580	5.1	188.5	11.8×10^{-3}
600	5.1	74.0	11.5×10^{-3}
620	5.4	34.3	11.0×10^{-3}
640	5.2	12.8	10.0×10^{-3}
660	5.1	6.4	10.0×10^{-3}
680	5.4	3.2	12.3×10^{-3}

D. Summary of the parametric studies conducted for the attempted synthesis of the nanomaterials

Table D.1 Parameter for the hydrothermal/solvothermal synthesis of the nanomaterials

Material	Precursors	Surfactant	Solvent	Reaction T (°C) / time (s)	Calcination T (°C) / time (s)
$FeCr_2O_4$	$Fe(NO_3)_2.6H_2O$ + $Cr(NO_3)_3.9H_2O$	NTA	2-propanol + UPW	180 °C / 6 h	350 °C / 2 h
		CTAB	2-propanol + UPW	180 °C / 6 h	350 °C / 2 h
		Urea	2-propanol + UPW	120 °C / 6 h	350 °C / 2 h
$CuMn_2O_4$	$Cu(NO_3)_2.3H_2O$ + $Mn(NO_3)_2.4H_2O$	EG	Methanol + UPW	160 °C / 12 h	-
		TEG	Methanol + UPW	160 °C / 12 h	-
		CTAC	Methanol + UPW	160 °C / 12 h	-
		CTAB	Methanol + UPW	160 °C / 12 h	-
		NTA	Methanol + UPW	160 °C / 12 h	-
		Urea	Methanol + UPW	160 °C / 12 h	-
	$CuCl_2$ + $MnCl_2.4H_2O$	-	2-propanol + UPW	180 °C / 6 h	-
	$Cu(OAc)_2.H_2O$ + $MnCl_2.4H_2O$	-	2-propanol + UPW	180 °C / 6 h	-
	$Cu(OAc)_2.H_2O$ + $MnCl_2.4H_2O$		2-propanol	180 °C / 6 h	-
	$CuCl_2$ + $MnCl_2.4H_2O$	-	2-propanol	180 °C / 6 h	-

Table D.1 (cont'd) Parameters for the hydrothermal/solvothermal synthesis of the nanomaterials

Material	Precursors	Surfactant	Solvent	Reaction T (°C) / time (s)	Calcination T (°C) / time (s)
CuMn$_2$O$_4$	Cu(acac)$_2$ + MnCl$_2$.4H$_2$O	-	2-propanol	180 °C / 6 h	-
	Cu(acac)$_2$ + MnSO$_4$	-		180 °C / 6 h	-
	CuCl$_2$ + MnSO$_4$	-		180 °C / 6 h	-
	Cu(OAc)$_2$.H$_2$O + MnSO$_4$	-		180 °C / 6 h	-
CoMn$_2$O$_4$	Co(OAc)$_2$.4H$_2$O + MnCl$_2$.4H$_2$O	-	2-propanol + UPW	180 °C / 6 h	-
	CoCl$_2$.6H$_2$O + MnCl$_2$.4H$_2$O	-		180 °C / 6 h	-
	Co(OAc)$_2$.4H$_2$O + MnCl$_2$.4H$_2$O	-	2-propanol	180 °C / 6 h	-
ZnMn$_2$O$_4$	Zn(OAc)$_2$.2H$_2$O + MnCl$_2$.4H$_2$O	-	2-propanol + UPW	180 °C / 6 h	-
	Zn(OAc)$_2$.2H$_2$O + MnCl$_2$.4H$_2$O	-	2-propanol	180 °C / 6 h	-
	Zn(OAc)$_2$.2H$_2$O + MnSO$_4$	-	2-propanol	180 °C / 6 h	-

Table D.1 (cont'd) Parameters for the hydrothermal/solvothermal synthesis of the nanomaterials

Material	Precursors	Surfactant	Solvent	Reaction T (°C) / time (s)	Calcination T (°C) / time (s)
FeMn$_2$O$_4$	FeCl$_2$ + MnCl$_2$.4H$_2$O	-	2-propanol + UPW	180 °C / 6 h	-
	FeCl$_2$ + MnCl$_2$.4H$_2$O	-	2-propanol	180 °C / 6 h	-
	FeCl$_3$ + MnCl$_2$.4H$_2$O	-		180 °C / 6 h	-
	Fe(acac)$_3$ + MnCl$_2$.4H$_2$O	-		180 °C / 6 h	-
	FeCl$_2$ + MnSO$_4$	-		180 °C / 6 h	-

Table D.2 Parameters for the hydrothermal/solvothermal synthesis of the nanomaterials

Material	Precursors	Surfactant	Solvent	Reaction T (°C) / time (s)	Calcination T (°C) / time (s)
$FeCr_2O_4$	$Fe(NO_3)_2.6H_2O$ + $Cr(NO_3)_3.9H_2O$	Citric acid	UPW	60 °C / 2h + 90 °C / 2 h	400 °C / 2 h
$MgCr_2O_4$	$Mg(NO_3)_2.6H_2O$ + $Cr(NO_3)_3.9H_2O$	Citric acid	UPW	60 °C / 2h + 90 °C / 2 h	400 °C / 2 h
$CuMn_2O_4$	$Cu(NO_3)_2.3H_2O$ + $Mn(NO_3)_2.4H_2O$	Citric acid	UPW	60 °C / 2h + 90 °C / 2 h	400 °C / 2 h
	$Cu(acac)_2$ + $MnCl_2.4H_2O$	Citric acid	UPW	95 °C / 2h + 160 °C / 2 h	700 °C / 3 h
$FeMn_2O_4$	$Fe(NO_3)_2.6H_2O$ + $Mn(NO_3)_2.4H_2O$	Citric acid	UPW	60 °C / 2h + 90 °C / 2 h	400 °C / 2 h
	$FeCl_2$ + $MnCl_2.4H_2O$	Citric acid	UPW	95 °C / 2h + 160 °C / 2 h	700 °C / 3 h

CURRICULUM VITAE

PERSONAL INFORMATION

Surname, Name: Çetin, Asude
Nationality: Turkish (TC)
Date and Place of Birth: 28 September 1989, Ankara
Marital Status: Single
Phone: +90 5301794744
email: asude.cetin@metu.edu.tr

EDUCATION

Degree	Institution	Year of Graduation
Ph.D	Middle East Technical University Department of Chemistry	2020
BS	Middle East Technical University Department of Chemistry	2012
High School	Dr.Binnaz Ege – Dr. Rıdvan Ege Anadolu High School, Ankara	2007

WORK EXPERIENCE

Year	Place	Enrollment
2012-Present	METU Chemistry	Teaching Assistant

SUCCESSES AND AWARDS

- TUBITAK 2211 A – National Scholarship Programme for PhD, Scholar

- Lando / National Science Foundation (NSF) Summer Undergraduate Research Programme, Scholar (University of Minnesota, Minnesota-USA, 2011)

- Honor Student in Department of Chemistry, Bachelor Degree (Middle East Technical University, Ankara, Turkey, 2012)

PUBLICATIONS

1. <u>Asude Çetin</u>, Okan Esentürk, Emren Nalbant Esentürk "Optical and vibrational properties of $[Pt@Pb_{12}]^{2-}$, $[Ni@Pb_{12}]^{2-}$ and $[Ni@Pb_{10}]^{2-}$ Zintl ion clusters" *Eur. J. Inorg. Chem.* **2017**, *18*, 2413-2421.

2. Elif Ekebaş, <u>Asude Çetin</u>, Ahmet M. Önal, Emren Nalbant Esentürk, "Magnesium substituted cobalt spinel nanostructures for electrocatalytic water oxidation reaction" *J. Appl. Electrochem.* **2019**, *49*, 315-325.

3. <u>Asude Çetin</u>, Ahmet M. Önal, Emren Nalbant Esentürk, Nanowires assembled from iron manganite nanoparticles: Synthesis, characterization and investigation of electrocatalytic properties for water oxidation reaction" *J. Mater. Res.* **2019**, *18*, 3231-3239.

4. Serra Kocabaş, <u>Asude Çetin</u>, Ahmet M. Önal, Emren Nalbant Esentürk, "Chromium substituted iron oxide nanowires as affordable electrocatalysts for oxygen evolution reaction" *J. Nanopart. Res.* **2019**, *21*, 143

5. <u>Asude Çetin</u>, Emren Nalbant Esentürk, "Hierarchical nanowire and nanoplate-assembled $NiCo_2O_4$-NiO biphasic microspheres as effective electrocatalysts for oxygen evolution reaction" *Mater. Today Chem.* **2019**, *14*, 100215.

CONFERENCES ATTENDED

- 257th ACS National Meeting & Exposition / 31 March – 4 April, 2019/ Orlando, Florida – USA
- 13th Nanoscience and Nanotechnology Conference / October, 2017 / Antalya – Turkey
- 29th National Chemistry Congress / September, 2017 / Ankara – Turkey
- 27th National Chemistry Congress / August, 2015 / Çanakkale – Turkey
- 11th Nanoscience and Nanotechnology Conference / June, 2015 / Ankara – Turkey

- 2014 Materials Research Society (MRS) Fall Meeting and Exhibition / November, 2014/ Boston, Massachusetts – USA
- 44th World Chemistry Congress / August, 2013/ Istanbul – Turkey
- Materials Research Science and Engineering Center(MRSEC) Summer Undergraduate Research Expo /August, 2011/ Minnesota - USA